

THE FLORIDA STATE UNIVERSITY  
COLLEGE OF ARTS AND SCIENCES

A CLIMATOLOGY OF THE SURFACE WIND FIELD, ITS DIVERGENCE  
AND THE ITCZ OVER THE EASTERN TROPICAL PACIFIC OCEAN


by

GERARD VOGEL

A Thesis submitted to the  
Department of Meteorology  
in partial fulfillment of the  
requirements for the degree of  
Master of Science


APPROVED:

  
\_\_\_\_\_  
Professor Directing Thesis

  
\_\_\_\_\_

  
\_\_\_\_\_

  
\_\_\_\_\_

  
\_\_\_\_\_

December, 1982

## ABSTRACT

A subjectively analyzed data set of monthly averaged ship wind observations on a  $2^\circ$  square grid for the period 1961-78 is used to describe the annual and seasonal climatology of the surface wind, the divergence of the surface wind, and the Intertropical Convergence Zone (ITCZ) over the eastern tropical Pacific Ocean. The climatology of the ITCZ is derived from independent monthly calculations of a best fit to the axis of maximum convergence within the Northern Hemisphere near-equatorial convergence zone.

The seasonal variability of the ITCZ latitudinal position exhibits considerable longitudinal dependence and is observed to be strongly related with variations in strength and areal extent of the SE trade wind regime. The intensity of convergence of the ITCZ is generally strong throughout the year for longitudes east of  $110^\circ\text{W}$  with strong convergence also observed westward from  $110^\circ\text{W}$  during the period July to November.

Interannual variability of the ITCZ latitudinal position and intensity of convergence is much less than the pronounced seasonal ITCZ variability. Plots of the ITCZ interannual variability do not confirm the generally held view that the ITCZ strengthens and shifts southward during El Niño events.

A search for secondary convergence zones reveals the existence of a significant Southern Hemisphere near-equatorial convergence zone during the December-February season as well as several distinct convergence mechanisms operative within the Northern Hemisphere near-equatorial convergence zone.

## ACKNOWLEDGMENTS

I am most grateful to my major professor and director of thesis, Dr. J. J. O'Brien, for his support, encouragement, and helpful discussions throughout the course of this research. My gratitude is also extended to thesis committee members Drs. J. Stephens, N. LaSeur, and D. Cadet for their comments and suggestions. I would like to thank all the members of the Mesoscale Air-Sea Interaction Group for their support and encouragement, most especially Pat Teaf, for her excellent typing of the various versions of this manuscript, Jim Merritt, for his excellent computer assistance and Roberta Scott, for drafting some of the thesis figures. Mr. Dewey Rudd also provided valuable drafting assistance.

This research was supported by the National Science Foundation, under Grants ATM-7920485 and OCE-8119052, and the Office of Naval Research. Computations were performed on the Cyber 170-760 at the Florida State University. The original wind stress data used in this study for the years 1961-71 have been provided through the courtesy of Drs. K. Wyrтки and G. Meyers; for the years 1972-78, through the courtesy of Dr. S. Pazan. The revised data set was prepared by the Mesoscale Air-Sea Interaction Group at Florida State University under Dr. J. J. O'Brien.

## TABLE OF CONTENTS

	Page
ABSTRACT	ii
ACKNOWLEDGMENTS	iii
TABLE OF CONTENTS	iv
LIST OF TABLES	v
LIST OF FIGURES	vi
INTRODUCTION	1
DATA	3
DERIVED QUANTITIES	7
Divergence	
Intertropical Convergence Zone	
CLIMATOLOGY	25
Annual	
Seasonal	
INTERANNUAL VARIABILITY OF THE ITCZ	63
SECONDARY CONVERGENCE ZONES	77
SUMMARY AND CONCLUSIONS	82
APPENDIX	85
REFERENCES	91

## LIST OF TABLES

Table	Page
1. Total number and percent frequency per selected 12° longitude bands of positive divergence values resulting from the application of the ITCZ analysis procedure.	10
2. Annual and monthly averages, and standard deviations about the annual mean, of the ITCZ latitudinal position for selected longitude bands. All units are degrees and tenths of degree of latitude. Values are derived from the four time series of Fig. 3.	22
3. Annual and monthly averages, and standard deviations about the annual mean, of the ITCZ intensity of convergence for selected longitude bands. All units are $10^{-6} \text{ s}^{-1}$ . Values are derived from the four time series of Fig. 4.	23
4. Total variance as well as the frequencies and percentage of the total variance explained by the two largest harmonics calculated from each of the four 22° band averaged time series of the ITCZ latitudinal position given in Fig. 3. Units of variance are degrees squared; frequencies are $\text{year}^{-1}$ .	56
5. Total variance as well as the frequencies and percentage of the total variance explained by the two largest harmonics calculated from each of the four 22° band averaged time series of the ITCZ intensity of convergence given in Fig. 4. Units of variance are $10^{-12} \text{ s}^{-2}$ ; frequencies are $\text{year}^{-1}$ .	58
A1. List of symbols and glossary of terms used in association with the ITCZ analysis procedure. Units of variance are $10^{-12} \text{ s}^{-2}$ ; frequencies are $\text{year}^{-1}$ .	85
A1. List of symbols and glossary of terms used in association with the ITCZ analysis procedure.	85

## LIST OF FIGURES

Figure	Page
1. Base ten logarithm of the total number of ship observations per $2^\circ \times 10^\circ$ latitude-longitude quadrangles for the period January 1961-December 1978.	4
2. Range and boundaries for the ITCZ analysis procedure. Outer boundaries are data limits; no ITCZ calculations are allowed beyond these limits.	9
3. (a) Time series of the derived ITCZ latitudinal position, band averaged across $22^\circ$ of longitude from $79^\circ\text{W}$ to $101^\circ\text{W}$ and centered at $90^\circ\text{W}$ . (b) Similar to (a) but for band $99^\circ\text{W}$ to $121^\circ\text{W}$ and centered at $110^\circ\text{W}$ . (c) Similar to (a) but for band $119^\circ\text{W}$ to $141^\circ\text{W}$ and centered at $130^\circ\text{W}$ . (d) Similar to (a) but for band $139^\circ\text{W}$ to $161^\circ\text{W}$ and centered at $150^\circ\text{W}$ .	14-17
4. (a) Time series of the derived ITCZ intensity of convergence band averaged across $22^\circ$ of longitude from $79^\circ\text{W}$ to $101^\circ\text{W}$ and centered at $90^\circ\text{W}$ . (b) Similar to (a) but for band $99^\circ\text{W}$ to $121^\circ\text{W}$ and centered at $110^\circ\text{W}$ . (c) Similar to (a) but for band $119^\circ\text{W}$ to $141^\circ\text{W}$ and centered at $130^\circ\text{W}$ . (d) Similar to (a) but for band $139^\circ\text{W}$ to $161^\circ\text{W}$ and centered at $150^\circ\text{W}$ .	18-21
5. Time series of the number of ship wind observations per month between $6^\circ\text{N}$ and $12^\circ\text{N}$ for selected $20^\circ$ longitude bands across the eastern tropical Pacific Ocean.	24
6. Annual mean surface wind vectors over the eastern tropical Pacific Ocean. Vector scale is given in upper right corner.	26
6. Annual mean surface wind vectors over the eastern tropical Pacific Ocean. Vector scale is given in upper right corner.	26

7. Annual mean surface wind divergence over the eastern tropical Pacific Ocean. Units of divergence are  $10^{-6} \text{ s}^{-1}$  (solid lines divergence, dashed lines convergence). 28
8. Annual and seasonal mean latitudinal positions of the ITCZ. Legend: (1) Annual, (2) December, January, February season, (3) March, April, May season, (4) June, July, August season, and (5) September, October, November season. 30
9. (a) Mean surface wind vectors over the eastern tropical Pacific Ocean for December, January, February season. Vector scale is given in upper right corner. (b) Similar to (a) but for March, April, May season. (c) Similar to (a) but for June, July, August season. (d) Similar to (a) but for September, October, November season. 32-35
10. (a) Mean surface wind divergence over the eastern tropical Pacific Ocean for December, January, February season. Units of divergence are  $10^{-6} \text{ s}^{-1}$  (solid lines divergence, dashed lines convergence). (b) Similar to (a) but for March, April, May season. (c) Similar to (a) but for June, July, August season. (d) Similar to (a) but for September, October, November season. 36-39
11. Seasonal variation in the latitudinal position of the ITCZ. Contours are in degrees of latitude north. 47
12. Seasonal variation in the standard deviation of the ITCZ latitudinal position. Contour units are degrees of latitude. Areas of standard deviation  $> 3^\circ$  are hatched. 48

13. Seasonal variation in the intensity of convergence of the ITCZ. Units of convergence are  $10^{-6} \text{ s}^{-1}$ . 49
14. Seasonal variation in the standard deviation of the ITCZ intensity of convergence. Contour units are  $10^{-6} \text{ s}^{-1}$ . Areas of standard deviation  $\geq 4 \times 10^{-6} \text{ s}^{-1}$  are hatched. 50
15. (a) ITCZ latitudinal position, band averaged across  $22^\circ$  of longitude from  $79^\circ\text{W}$  to  $101^\circ\text{W}$  and centered at  $90^\circ\text{W}$ , filtered with a twelve month running mean. (b) Similar to (a) but for band  $99^\circ\text{W}$  to  $121^\circ\text{W}$  and centered at  $110^\circ\text{W}$ . (c) Similar to (a) but for band  $119^\circ\text{W}$  to  $141^\circ\text{W}$  and centered at  $130^\circ\text{W}$ . (d) Similar to (a) but for band  $139^\circ\text{W}$  to  $161^\circ\text{W}$  and centered at  $150^\circ\text{W}$ . 64-67
16. (a) ITCZ intensity of convergence, band averaged across  $22^\circ$  of longitude from  $79^\circ\text{W}$  to  $101^\circ\text{W}$  and centered at  $90^\circ\text{W}$ , filtered with a twelve month running mean. (b) Similar to (a) but for band  $99^\circ\text{W}$  to  $121^\circ\text{W}$  and centered at  $110^\circ\text{W}$ . (c) Similar to (a) but for band  $119^\circ\text{W}$  to  $141^\circ\text{W}$  and centered at  $130^\circ\text{W}$ . (d) Similar to (a) but for band  $139^\circ\text{W}$  to  $161^\circ\text{W}$  and centered at  $150^\circ\text{W}$ . 68-71
17. Annual mean percent of time that a convergence maximum along a given meridian from  $12^\circ\text{S}$  to  $24^\circ\text{N}$  corresponds to at least 50% of the absolute maximum convergence along that same meridian. Approximate axes of high percentage, given as labelled dashed lines, are discussed in text. 80
- labelled dashed lines, are discussed in text.



A1. Detailed flow chart of the procedure used for one  $2^\circ$  space step ITCZ calculation ( $M_{\theta, \phi} \rightarrow M_{\theta_c, \phi+2}$ ) from a filtered divergence field. This scheme is followed for all computations except at the eastern boundary ( $\phi = 79^\circ\text{W}$ ) where  $M_{\theta, \phi}$  is defined to be the true minimum. All intensity averages are arithmetic means; calculated ITCZ latitudinal positions are given to the closest even number grid point. 86-90

## 1. INTRODUCTION

The term "Intertropical Convergence Zone", or ITCZ, is a highly ambiguous one in the tropical literature. It is often defined or considered to coincide with either the axis of maximum confluence between the Northern and Southern Hemisphere trades, the equatorial surface pressure trough, or near-equatorial axes of either maximum convergence, cloudiness, rainfall frequency, or sea surface temperature. A comparison of these six representations made by Hastenrath and Lamb (1978) using 60-year average ship data for the equatorial Atlantic and eastern Pacific Oceans clearly demonstrated that none of these representations is synonymous. For this paper the name ITCZ applies to the most persistent zone of strong convergence in the near-equatorial surface wind field of the eastern tropical Pacific Ocean. In reference to the literature, the definition of the ITCZ is in the sense implied by the referenced author.

The main emphasis of this study is to describe the quasi-Lagrangian climatology of the ITCZ. This climatology results from a synthesis of 216 independent monthly calculations of the ITCZ latitudinal position and intensity of convergence for the period 1961-78. Individual ITCZ values are determined from filtered monthly surface wind divergence maps by means of a specially-developed marching method.

Two topics of considerable interest, the interannual variability of the ITCZ and secondary convergence zones, are in separate sections.

Two topics of considerable interest, the interannual variability of the ITCZ and secondary convergence zones, are in separate sections.

The discussion of the interannual variability of the ITCZ latitudinal position and intensity of convergence gives special attention to the nature of the variability during El Niño events. An analysis using the full 18-year record of filtered monthly divergence maps provides information on the existence of secondary convergence zones and operative convergence mechanisms within the Northern Hemisphere near-equatorial convergence zone.

Another significant part of this study is a description of the climatology of the surface wind and the divergence of the surface wind over the eastern tropical Pacific Ocean. This tropical climatology is well portrayed by annual and seasonal mean maps. In particular, the surface wind vector maps are able to reveal clearly the seasonal variability of the principal asymmetric features of the low-level atmospheric circulation over the eastern tropical Pacific Ocean.

Throughout this paper, direct quantitative comparisons of the results of this study with those of previously published works will generally be avoided. This is in recognition of the considerable differences in data resolution, length, coverage, and representation found in the literature. On the other hand, more general qualitative comparisons or relationships will sometimes be employed in discussions and analyses.

## 2. DATA

The data base for this study consists of monthly wind stress estimates between 30°N and 30°S over the Pacific Ocean for the period January 1961 through December 1978. Wind stresses were computed from approximately three and a half million individual ship wind observations (excluding all observations with speeds  $> 40 \text{ m s}^{-1}$ ) according to

$$\tau = \rho_a C_d W^2 \quad (1a)$$

$$\tau_x = \rho_a C_d W_x W \quad (1b)$$

$$\tau_y = \rho_a C_d W_y W \quad (1c)$$

where  $\tau$  is the magnitude of the wind stress defined by  $\hat{\tau} = \tau_x \hat{i} + \tau_y \hat{j}$ ,  $\rho_a$  is the air density,  $C_d$  is the drag coefficient and  $W$  is the magnitude of the horizontal wind speed defined by  $\hat{W} = W_x \hat{i} + W_y \hat{j}$ . The subscripts  $x$  and  $y$  refer to the zonal and meridional components, positive to the east and north, respectively. The methods used to develop the data set are further described by Wyrтки and Meyers (1975). The overall data distribution for the eastern tropical Pacific Ocean, per  $2^\circ \times 10^\circ$  latitude-longitude quadrangles, is depicted in Fig. 1 and indicates good to excellent coverage for the Pacific waters adjacent to the North American coast and those from the Mexican coast westward through Hawaii, but generally poor coverage along the immediate South American coastal waters and along an axis extending roughly from  $5^\circ\text{N}$ ,  $100^\circ\text{W}$  to  $8^\circ\text{S}$ ,  $160^\circ\text{W}$ .

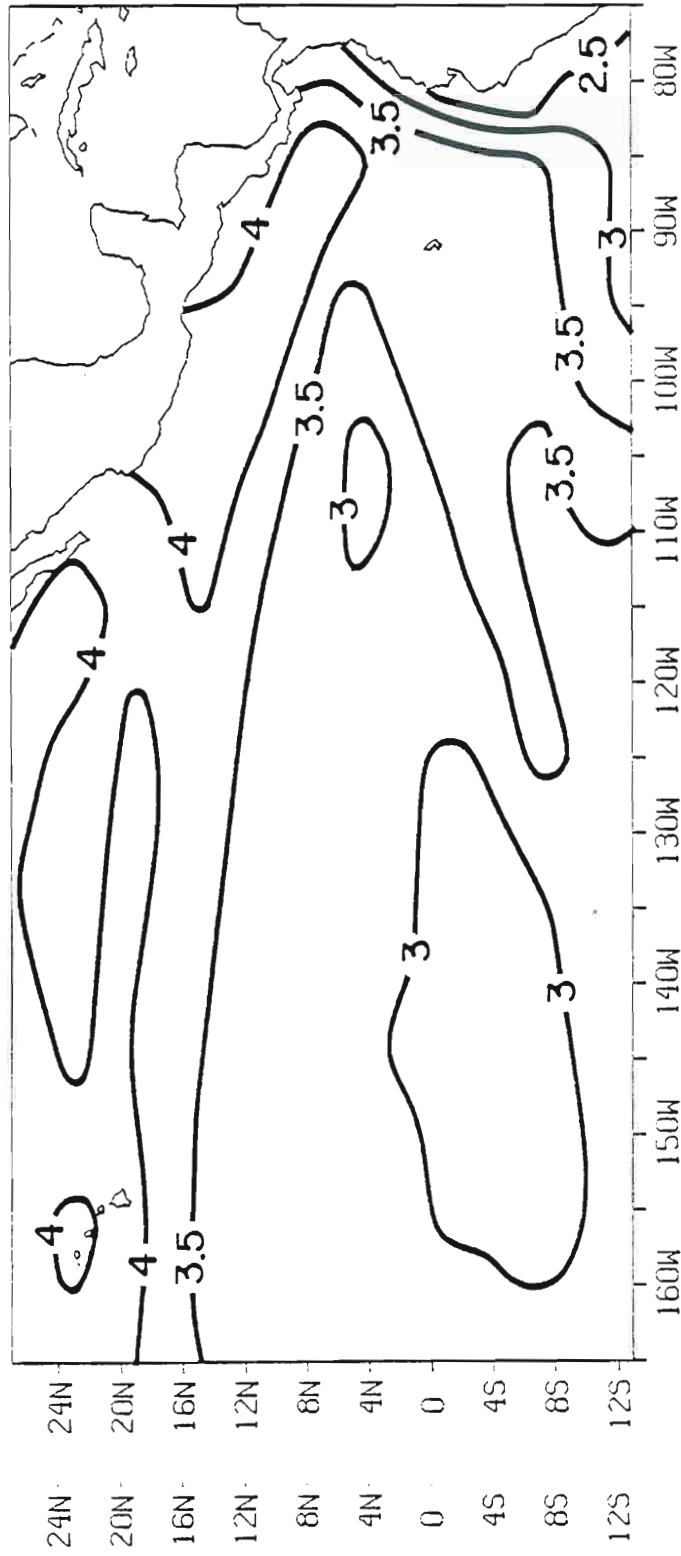


Fig. 1. Base ten logarithm of the total number of ship observations per 2° x 10° latitude-longitude quadrangles for the period January 1961-December 1978.

Monthly wind stress averages were originally computed per  $2^\circ \times 10^\circ$  quadrangles. A revised data set, subjectively analyzed and then digitized on a  $2^\circ$  square grid, was created to remove deficiencies in the data as well as provide a finer grid needed to drive coupled numerical atmosphere-ocean models. As a starting point in the analysis procedure, the quantity  $\rho_a C_D$  was assumed constant and was omitted from the analyses. The term "wind stress" now thus refers to equations 1a-c, without the factor,  $\rho_a C_D$ ; i.e.,  $\tau_x$  and  $\tau_y$ , the zonal and meridional components of the wind stress, respectively, refer to the quantities

$$\tau_x = W_x W \quad (2a)$$

$$\tau_y = W_y W \quad (2b)$$

Separate scalar analyses of these two components involved eliminating obvious sign errors due to bad data transmission, weighing each quadrangle by the number of observations per month to yield more representative data fields, filling data-void regions through use of surrounding data and patterns, time continuity, and climatological maps, and smoothing unrealistically strong gradients. Extension of the analysis to include some land areas was undertaken to accommodate the approximate land boundaries that are used in ocean models. Further details of the revised wind stress data set and analysis methods are given by O'Brien and Goldenberg (1982).

The zonal and meridional wind components,  $W_x$  and  $W_y$ , are derived on the  $2^\circ$  square grid from  $\tau$  by the use of the formulae

$$W_x = \tau_x (\tau_x^2 + \tau_y^2)^{-1/4} \quad (3a)$$

on the  $2^\circ$  square grid from  $\tau$  by the use of the formulae

$$W_x = \tau_x (\tau_x^2 + \tau_y^2)^{-1/4} \quad (3a)$$

$$W_y = \tau_y (\tau_x^2 + \tau_y^2)^{-1/4} \quad (3b)$$

Plots of the annual and seasonal mean surface wind vectors over the eastern tropical Pacific Ocean reflecting the full 18-year revised data set are presented and discussed subsequently in Section 4.

### 3. DERIVED QUANTITIES

#### a. DIVERGENCE

The divergence of the wind is given by

$$\nabla \cdot \hat{W} = \partial W_x / \partial x + \partial W_y / \partial y \quad (4)$$

The derivatives are calculated on a 2° latitude-longitude grid from 24°N to 12°S and from 161°W to the Pacific coast of America by averaging across the 2° box centered on each point. Data extrapolation results in a few divergence calculations over land areas at the eastern boundary. Variations in the meridional separation are quite small for tropical latitudes and are not taken into account. A single pass of a 1-2-1 filter is applied individually to all monthly calculated divergence fields, first in the E-W direction, then in the N-S direction, to reduce small-scale spatial structure at scales < 6° in extent. Plots of the smoothed annual and seasonal mean wind divergence fields are presented and discussed in Section 4.

#### b. ITCZ

The term "Intertropical Convergence Zone", or ITCZ, is applied to the most persistent zone of strong convergence in the near-equatorial surface wind field. It is represented by a best fit to the axis of maximum convergence within the zone and is calculated independently for each of the 216 filtered monthly surface wind divergence fields.

The analysis method used for the ITCZ calculations will now be discussed. A detailed flow chart of the procedure (Fig. A1) and a list

The analysis method used for the ITCZ calculations will now be discussed. A detailed flow chart of the procedure (Fig. A1) and a list



of symbols and a glossary of terms used in conjunction with the method (Table A1) are provided for reader reference. In general, for any particular month, the analysis proceeds from the divergence minimum at the eastern boundary ( $\phi = 79^\circ\text{W}$ ) and marches westward within a certain range of latitude (see Fig. 2) calculating the position and intensity of convergence of the ITCZ at  $2^\circ$  longitude intervals up to and including  $\phi = 161^\circ\text{W}$ . Any relative and absolute minimum(s) for the next longitude fully contained within a latitude domain  $8^\circ$  north and south of the previous solution are found. Depending upon the sign of the minimum(s), the analysis procedure branches. The various cases are discussed below.

#### Case I Minimum(s) $> 0$

The search interval at  $\phi+2$  is expanded to include the entire range or even perhaps boundary values. An unsuccessful search for a minimum  $< 0$  results in a positive divergence value being selected as the  $M_{\theta_c, \phi+2}$  (ITCZ) value; such a value is retained in the ITCZ data series for statistical completeness. Occurrence of positive values (see Table 1) is not frequent and is almost entirely restricted to longitudes east of  $120^\circ\text{W}$ , and there often in association with various hyperbolic points in the summer and fall mean surface wind fields. If a negative value is found, the resulting  $M_{\theta_c, \phi+2}$  may or may not be a negative value depending upon the magnitude of the minimum value and averaging employed.

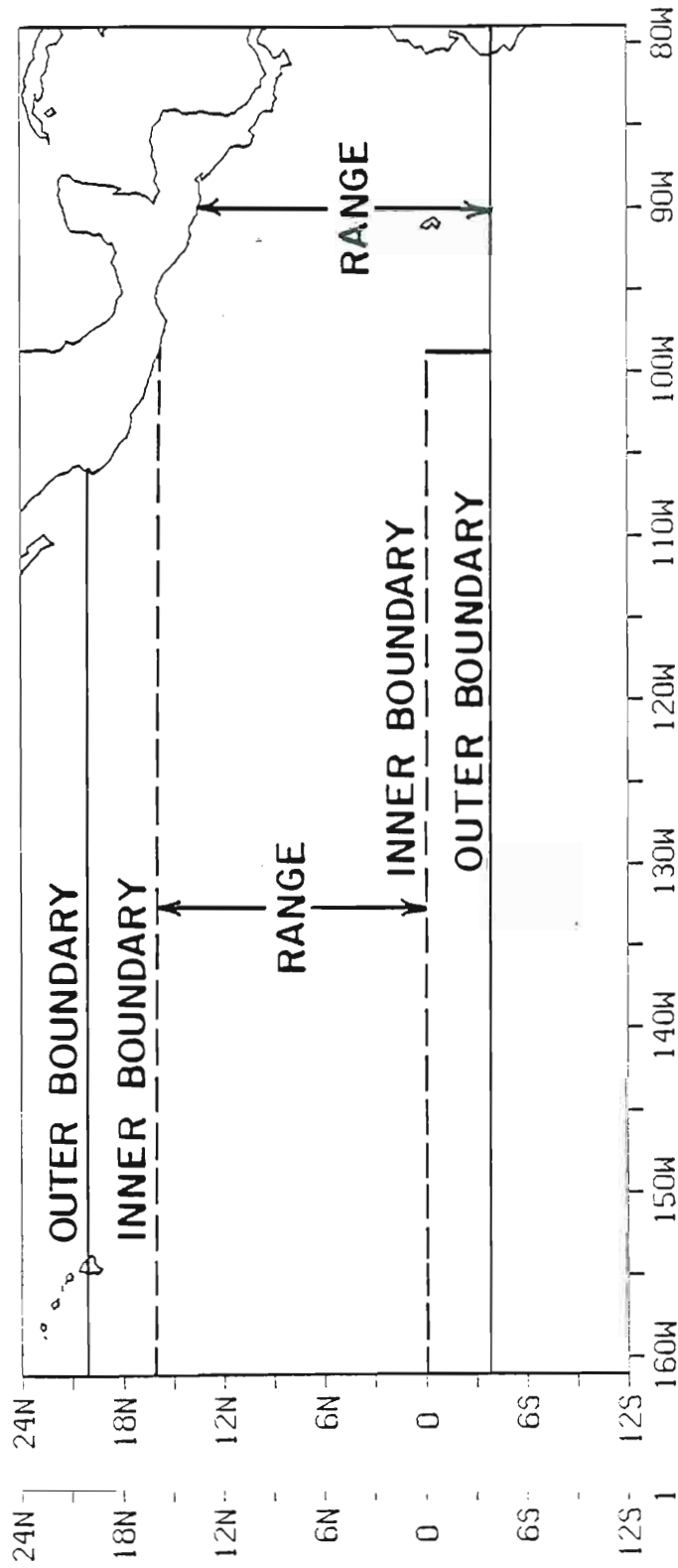


Fig. 2. Range and boundaries for the ITCZ analysis procedure. Outer boundaries are data limits; no ITCZ calculations are allowed beyond these limits.

Table 1. Total number and percent frequency per selected 12° longitude bands of positive divergence values resulting from the application of the ITCZ analysis procedure.

Band	No. Values > 0	Freq. of Values > 0(%)
79°W-91°W	26	1.72
93°W-105°W	10	.66
107°W-119°W	23	1.52
121°W-133°W	2	.13
135°W-147°W	0	0
149°W-161°W	0	0

Case II Minimum(s)  $< 0$ 

A test is first performed to ascertain if all minimums are located within the same band (an interval in  $\theta$  with all values having the same sign). If only one band is relevant for the calculation, the magnitudes of the absolute range minimum and the band minimums are compared. Unless the absolute band minimum is dominant, i.e.,  $> 50\%$  of the absolute range minimum and  $> 200\%$  of any other range minimum, averaging is used to compute  $M_{\theta_c, \phi+2}$ . The analysis procedure for minimums contained within several distinct bands parallels that for a single band case once a determination has been made as to whether or not any one convergence band is dominant.

When averaging is used to define a climatologically representative axis of maximum convergence for the ITCZ, much of the mesoscale structure of the convergence zone is lost if there exists two or more convergence bands in relative proximity and of comparable magnitude. A more detailed small-scale analysis of the full 18-year data record would show a complex ITCZ structure with the occurrence of two or more "broken" convergence bands embedded within the boundaries of the zone. This is a common, yet random, feature, with a tendency to occur more often between  $120^\circ\text{W}$  and  $160^\circ\text{W}$  and near the American coast but without any apparent temporal regularity. Fletcher (1945), by examining information provided by weather reconnaissance planes operating in the southern Caribbean and south of Panama, concluded that the inter-tropical convergence zone frequently breaks down into two or more lines of convergence due to radiative processes. More recently, Ramage et al. (1981), in a detailed six week study of the central Pacific

near-equatorial convergence zone, also found that the structure of the zone was highly variable and usually comprised of alternating bands of convergence and divergence.

All calculated ITCZ latitudinal positions are given to the closest even number grid point. When required, ITCZ intensity of convergence averages are calculated as arithmetic means. Once all (42) ITCZ latitudinal positions have been calculated from  $\phi = 79^{\circ}\text{W}$  to  $\phi = 161^{\circ}\text{W}$  for any given month, a continuous line drawn through all positional values represents the ITCZ.

In general, the ITCZ analysis procedure is nonlinear. The extent of nonlinearity depends upon the structure of the particular smoothed divergence map from which the ITCZ is derived. For example, the ITCZ analysis procedure will introduce more nonlinearity into an ITCZ calculation from a filtered monthly divergence map with a weak and complex structure within the near-equatorial convergence zone than into a calculation from a divergence map with a strong and simple structure within that same zone. The effect of this nonlinearity in the ITCZ analysis procedure will be apparent later when mean annual and seasonal ITCZ positions are compared with axes of maximum convergence as seen on mean annual and seasonal divergence maps.

Several problems were encountered in the application of the ITCZ analysis procedure and should be mentioned. First, due to the finite difference grid limitations imposed by the presence of the Central American coastline, caution should be exercised in interpreting the derived divergence and ITCZ values east of  $90^{\circ}\text{W}$  and in very close proximity to this coastline. Second, the analysis method, sometimes,

especially west of  $120^{\circ}\text{W}$ , had difficulty differentiating between the speed convergence of the northern hemisphere trade winds and the actual intertropical convergence and this resulted in a derived ITCZ axis being displaced slightly north of its probable location.

Time series of the derived ITCZ position and intensity of convergence, band averaged across  $22^{\circ}$  of longitude and centered at  $90^{\circ}\text{W}$ ,  $110^{\circ}\text{W}$ ,  $130^{\circ}\text{W}$  and  $150^{\circ}\text{W}$ , are plotted in Figs. 3a-d and 4a-d, respectively. Statistics derived from these time series are given in Tables 2 and 3.

In order to examine the homogeneity and density of the original ship wind data upon which Figs. 3 and 4 are based, time series of the number of observations within  $\sim 3^{\circ}$  of latitude of the annual mean ITCZ position (i.e. between  $6^{\circ}\text{N}$  and  $12^{\circ}\text{N}$ ) for longitude bands comparable to those of Figs. 3 and 4 are presented (Fig. 5). The data is observed to be very dense for the longitude band centered at  $90^{\circ}\text{W}$  but much less so for the bands centered at  $110^{\circ}\text{W}$ ,  $130^{\circ}\text{W}$  and  $150^{\circ}\text{W}$ . In general, areas of high data density exhibit less homogeneity in time; areas of low data density, more homogeneity. During the late 1960's and early 1970's, the bands  $80\text{-}100^{\circ}\text{W}$  and  $100\text{-}120^{\circ}\text{W}$  both show a broad peak in the number of observations. Pronounced changes in data density and homogeneity, such as those observed in 1971 and 1972 for the longitude band  $80\text{-}100^{\circ}\text{W}$  and in 1962 for the band  $140\text{-}160^{\circ}\text{W}$ , do not appear to have any significant effect on either ITCZ position or intensity of convergence calculations. On the other hand, the longitudinal structure in data density suggests that ITCZ calculations west of  $100^{\circ}\text{W}$  are most likely calculations. On the other hand, the longitudinal structure in data density suggests that ITCZ calculations west of  $100^{\circ}\text{W}$  are most likely of less reliability than those eastward from that longitude.

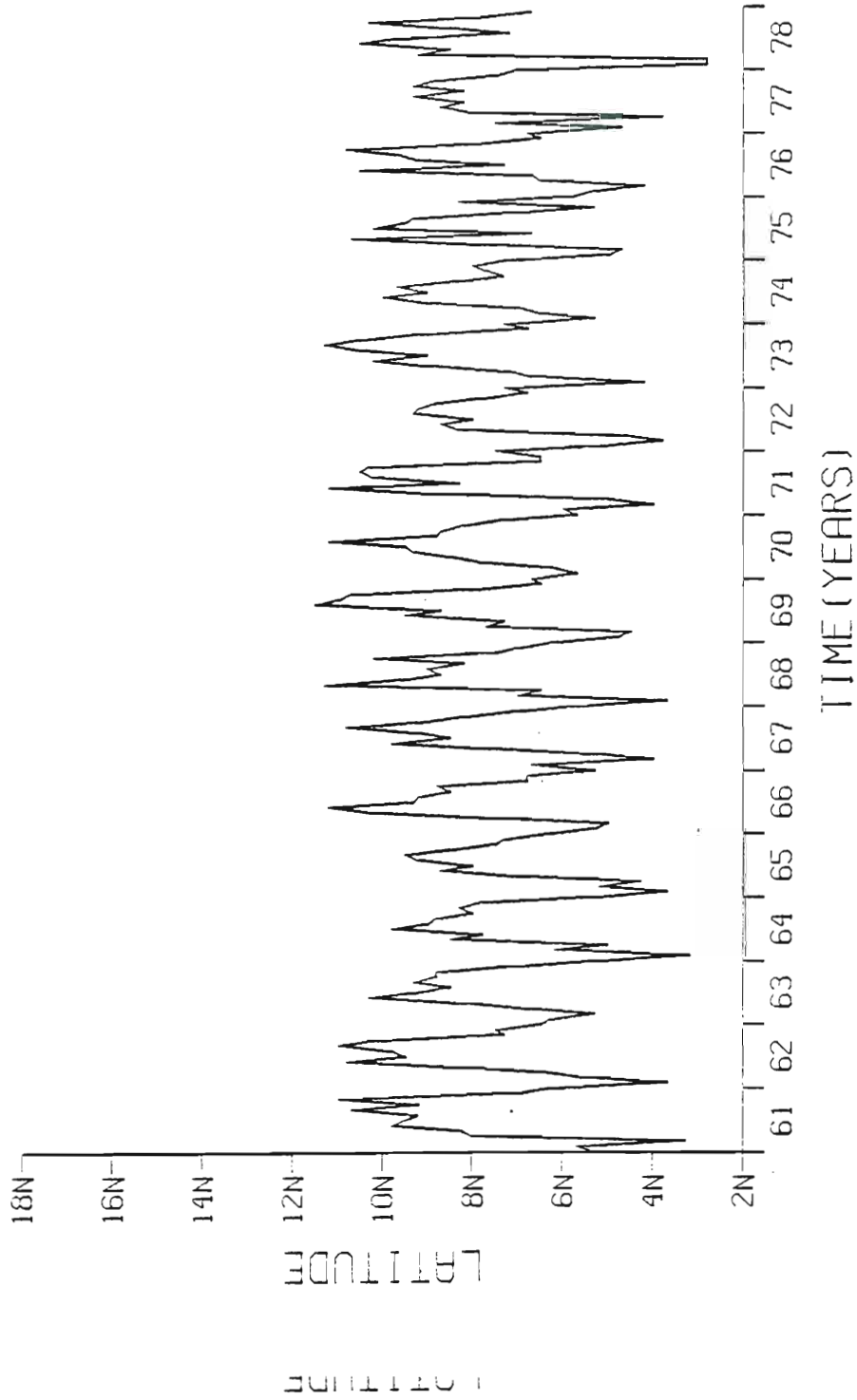


Fig. 3. (a) Time series of the derived ITCZ latitudinal position, band averaged across  $22^\circ$  of longitude from  $79^\circ\text{W}$  to  $101^\circ\text{W}$  and centered at  $90^\circ\text{W}$ .

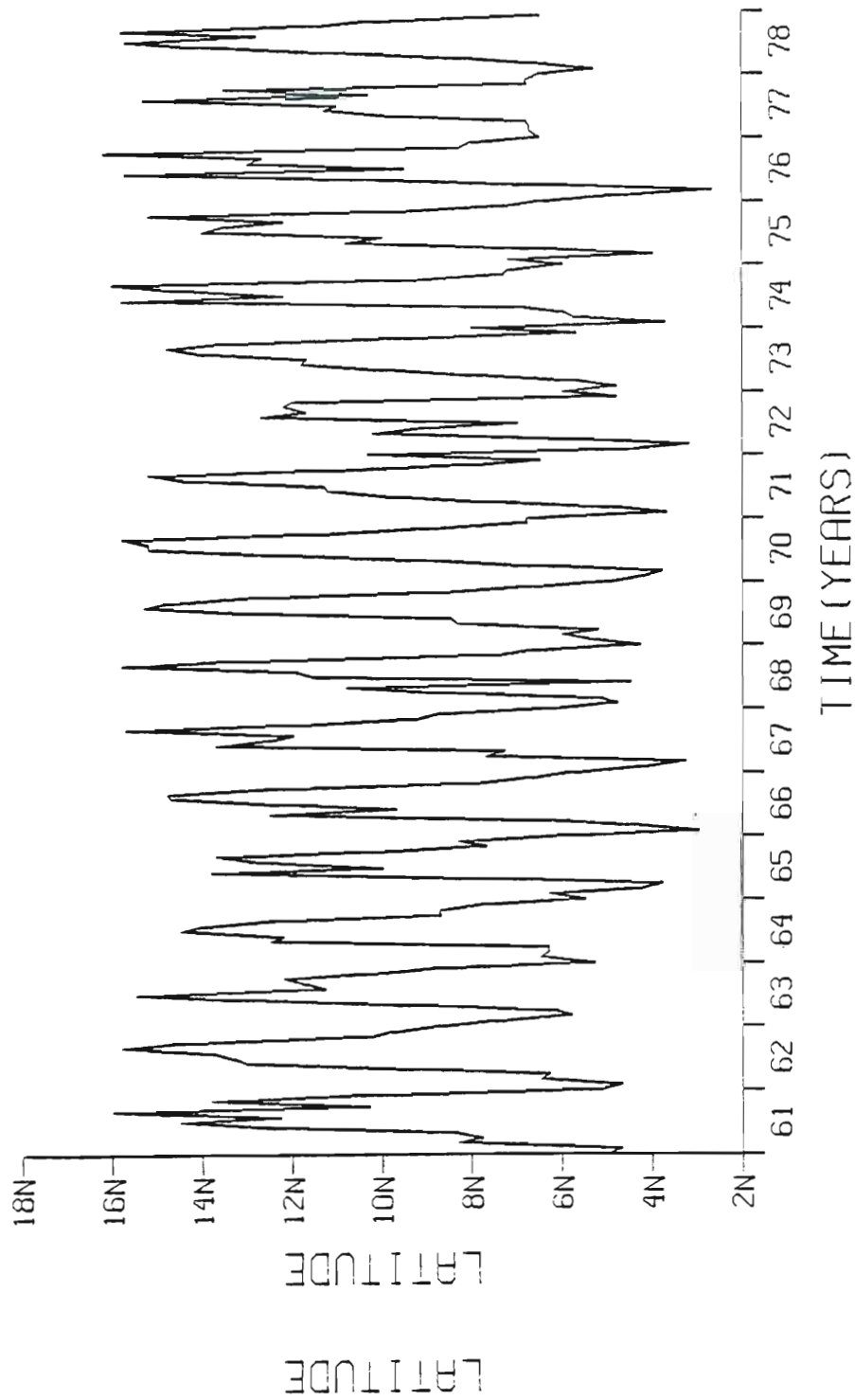


Fig. 3. (b) Similar to (a) but for band 99°W to 121°W and centered at 110°W.



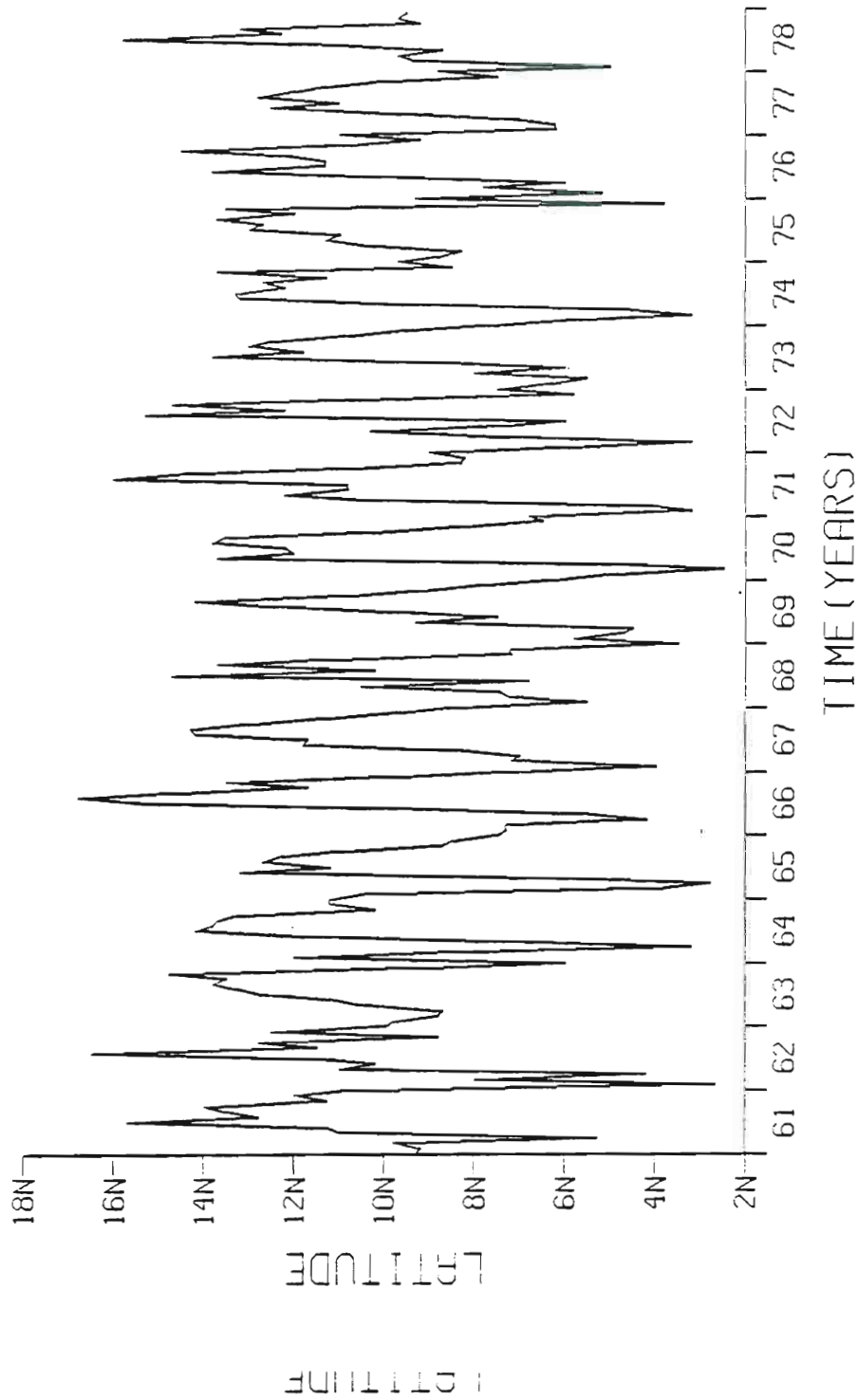


Fig. 3. (c) Similar to (a) but for band 119°W to 141°W and centered at 130°W.

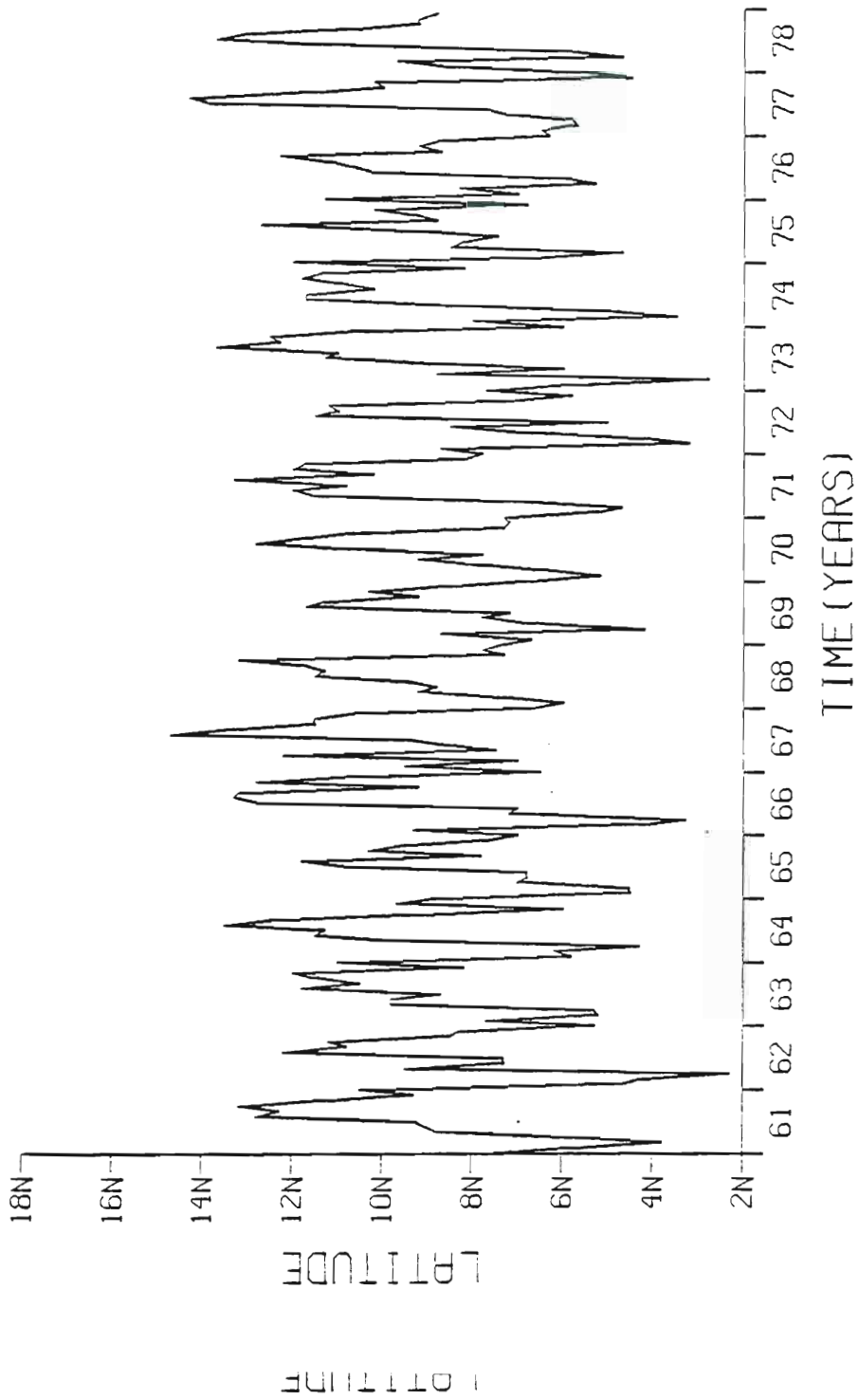


Fig. 3. (d) Similar to (a) but for band 139°W to 161°W and centered at 150°W.

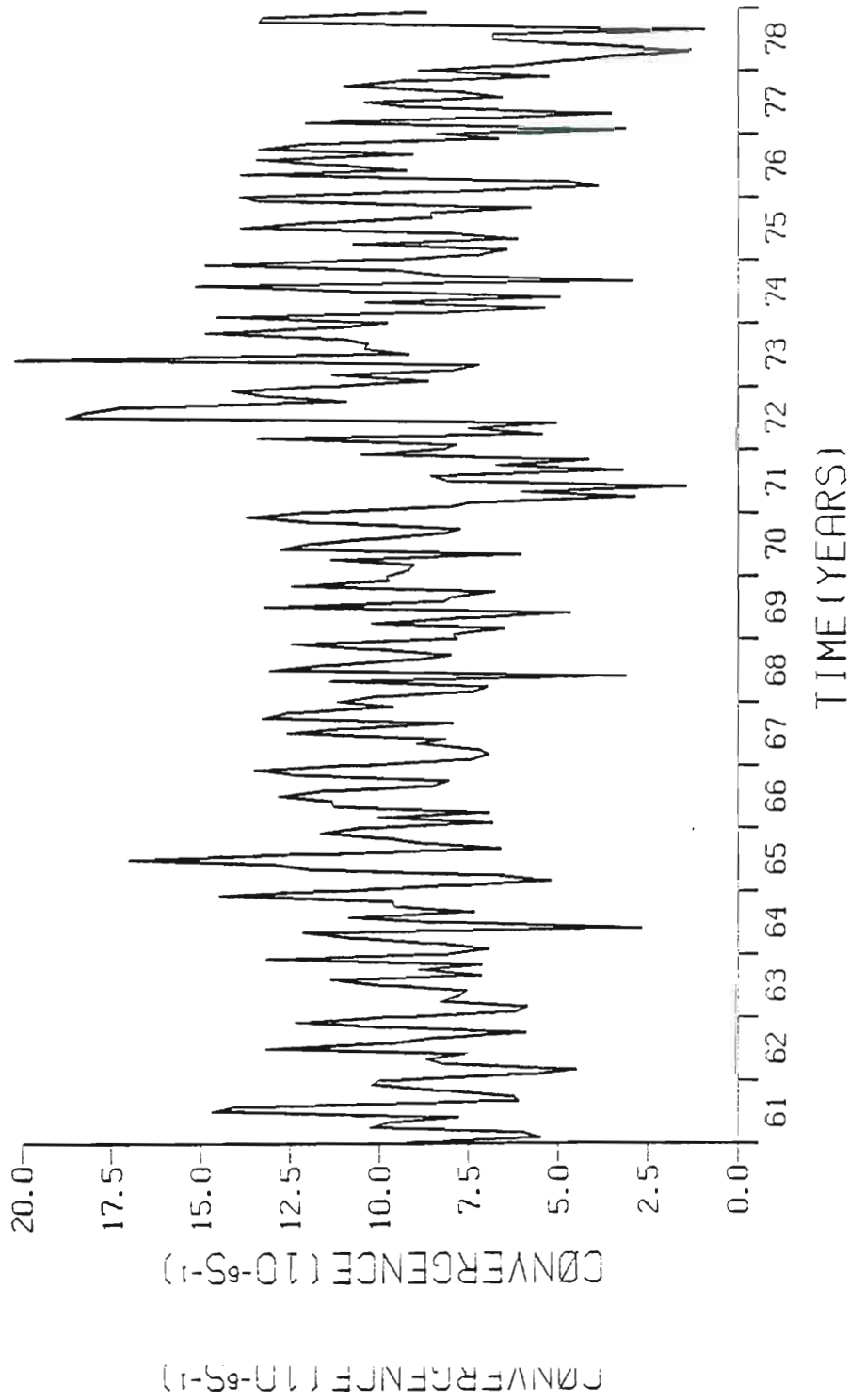


Fig. 4. (a) Time series of the derived ITCZ intensity of convergence band averaged across 22° of longitude from 79°W to 101°W and centered at 90°W.

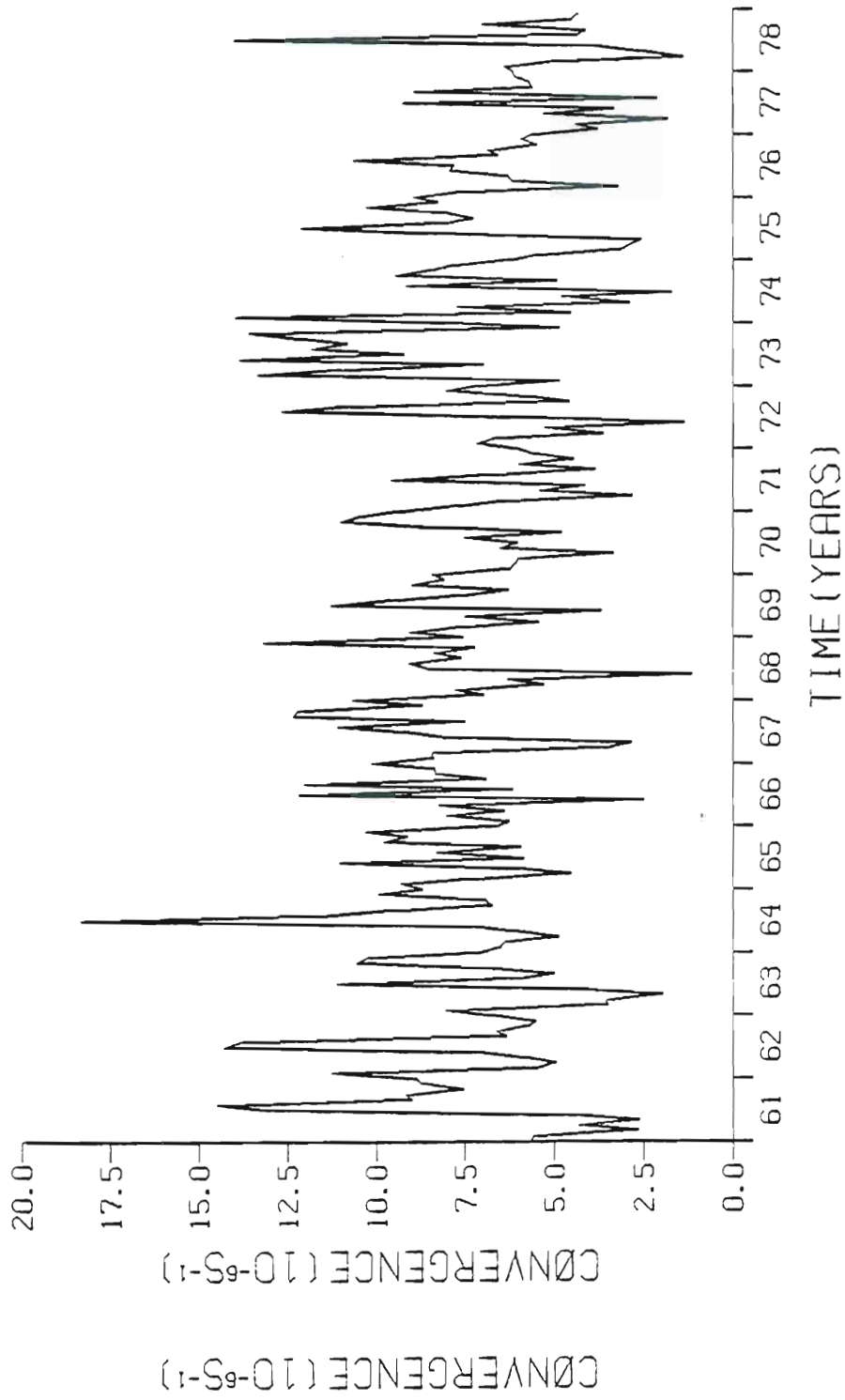


Fig. 4. (b) Similar to (a) but for band 99°W to 121°W and centered at 110°W.

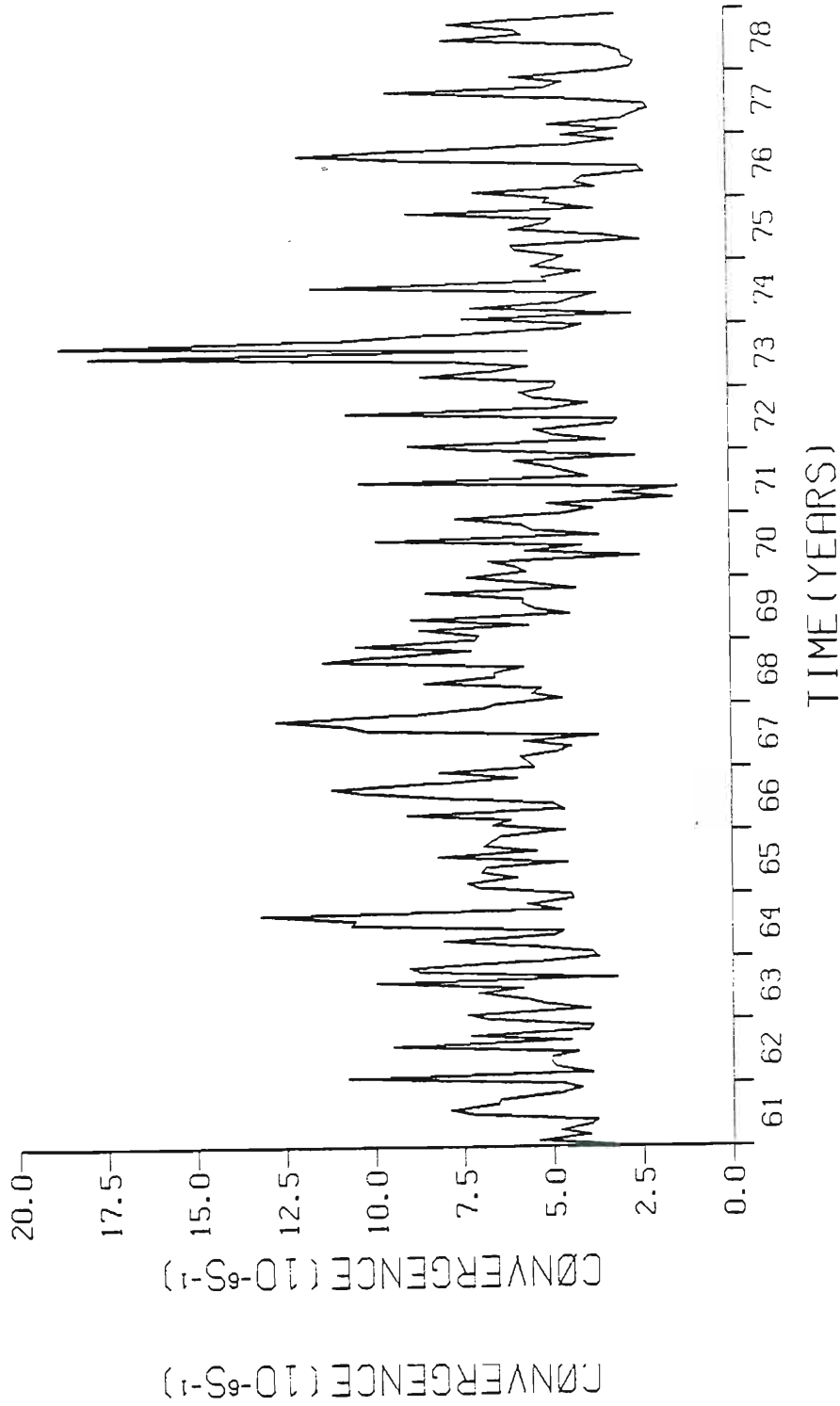


Fig. 4. (c) Similar to (a) but for band 119°W to 141°W and centered at 130°W.

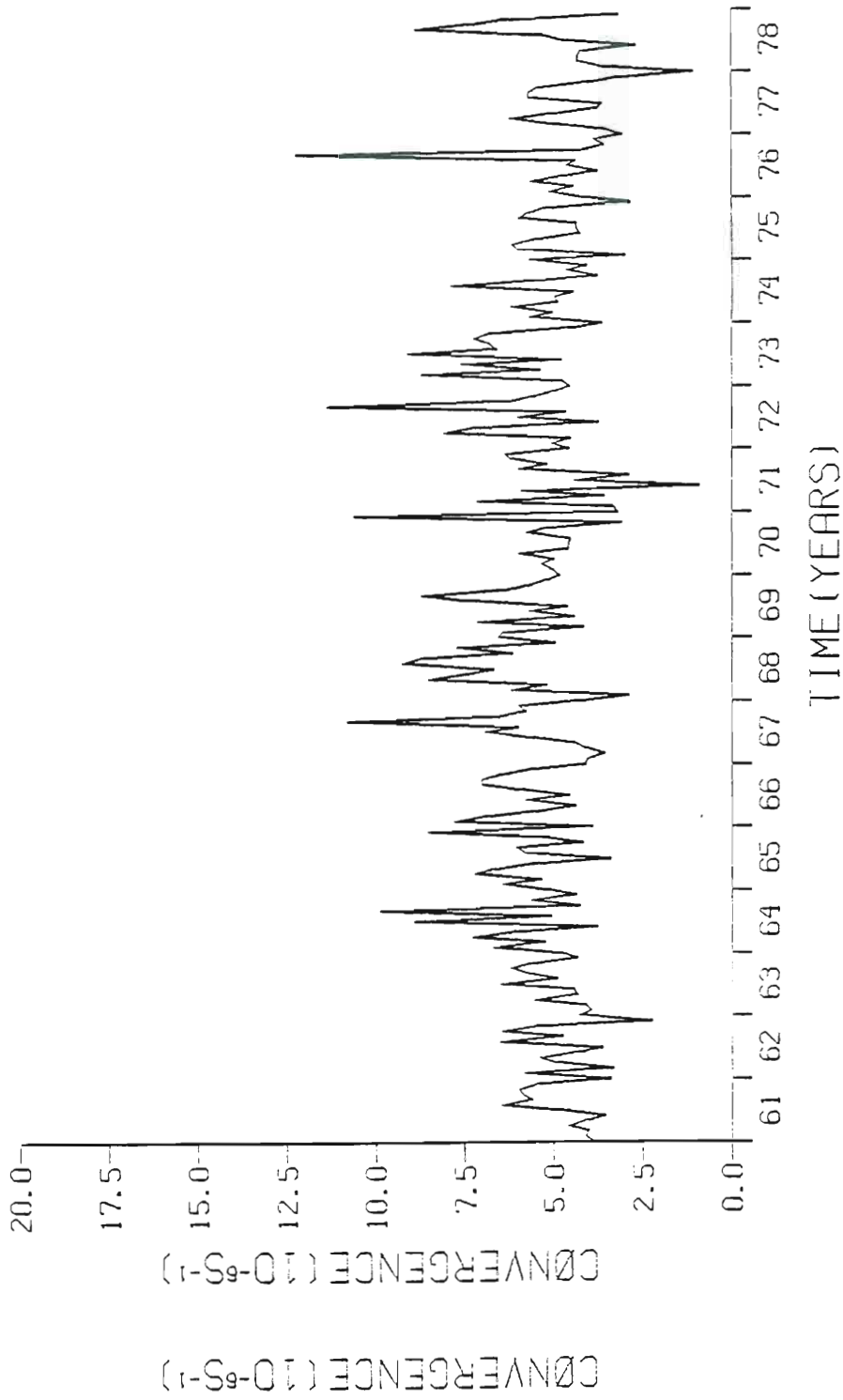


Fig. 4. (d) Similar to (a) but for band 139°W to 161°W and centered at 150°W.

Table 2. Annual and monthly averages, and standard deviation about the annual mean, of the ITCZ latitudinal position for selected longitude bands. All units are degrees and tenths of degree of latitude. Values are derived from the four time series of Fig. 3.

Longi Ban	Longitude Band	Monthly Average												Annual Average	Std. Deviation
		Jan	Feb	Mar	Apr	May	Jun	Jul	Aug	Sep	Oct	Nov	Dec		
139-16	139-161°W	7.9	6.8	5.6	6.2	8.0	9.1	10.3	12.4	11.3	10.8	9.9	8.3	8.9	2.7
119-14	119-141°W	8.3	6.6	6.4	6.5	9.6	10.8	12.4	13.4	13.3	12.1	10.6	8.7	9.9	3.2
99-12	99-121°W	6.3	5.1	5.2	6.7	9.7	11.8	12.5	13.5	14.2	12.3	9.2	7.4	9.5	3.6
79-10	79-101°W	6.3	4.9	5.1	6.5	8.6	9.6	8.9	9.5	9.5	9.3	7.9	7.1	7.8	2.0

Table 3. Annual and monthly averages, and standard deviations about the annual mean, of the ITCZ intensity of convergence for selected longitude bands. All units are  $10^{-6} \text{ s}^{-1}$ . Values are derived from the four time series of Fig. 4.

Longitude Band	Longitude Band	Monthly Average												Annual Average	Std. Deviation	
		Jan	Feb	Mar	Apr	May	Jun	Jul	Aug	Sep	Oct	Nov	Dec			
139-161°	89-161°W	4.2	4.9	5.2	5.7	5.5	4.4	5.3	5.8	7.5	5.8	5.5	5.0	5.4	5.4	1.7
119-141°	119-141°W	5.2	5.9	5.2	5.4	4.8	4.7	6.3	8.0	7.9	7.5	5.8	5.5	6.0	6.0	2.6
99-121°	99-121°W	7.7	7.5	6.1	4.8	4.9	4.8	10.0	9.1	7.4	7.9	8.1	8.0	7.3	7.3	3.0
79-101°	79-101°W	10.0	7.7	7.7	7.5	8.4	4.9	12.0	11.2	7.7	9.3	10.3	11.4	9.3	9.3	3.2



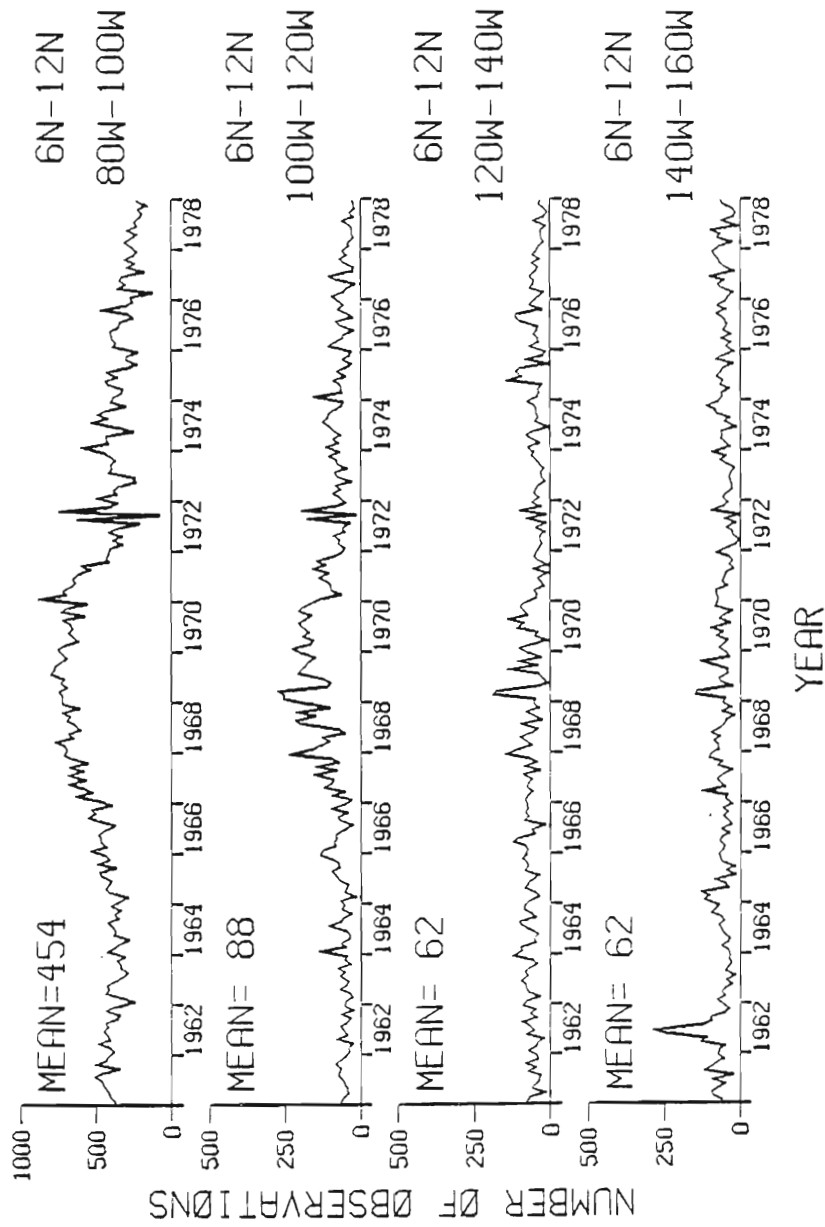


Fig. 5. Time series of the number of ship wind observations per month between 6°N and 12°N for selected 20° longitude bands across the eastern tropical Pacific Ocean.

#### 4. CLIMATOLOGY

##### a. ANNUAL

The mean annual large-scale atmospheric surface circulation pattern over the eastern tropical Pacific Ocean (Fig. 6) is dominated by the northeast and southeast trade winds which spin off the eastern side of the North and South Pacific subtropical anticyclones, respectively, into a near-equatorial zone of asymptotic confluence located approximately between  $5^{\circ}$  and  $10^{\circ}$ N. West of  $95^{\circ}$ W, winds from both hemispheres within this confluence zone have an easterly component, and a net easterly flow results; in such circumstances, the zone is sometimes also referred to as a "trade wind equatorial trough" (Gray, 1968). East of  $95^{\circ}$ W, winds on the poleward side of the confluence zone have an easterly component and those on the equatorial side an opposing westerly component, but are generally light and variable in the vicinity of the zone axis. In such circumstances, the zone is characterized by directional shear and is sometimes called a "doldrum equatorial trough" (Gray, 1968) or "monsoon trough" (Atkinson, 1971).

The presence of the ITCZ in the Northern Hemisphere results in the areal coverage of the northeast trade winds being considerably less than that for the southeast trade winds. Although the maximum wind speeds within the two trade wind systems are approximately the same ( $\sim 7.5 \text{ m s}^{-1}$ ), the core of maximum NE winds, located near  $15^{\circ}$ N, is closer to the ITCZ than the core of maximum SE trade winds, being ( $\sim 7.5 \text{ m s}^{-1}$ ), the core of maximum NE winds, located near  $15^{\circ}$ N, is closer to the ITCZ than the core of maximum SE trade winds, being centered near  $9^{\circ}$ S,  $105^{\circ}$ W.

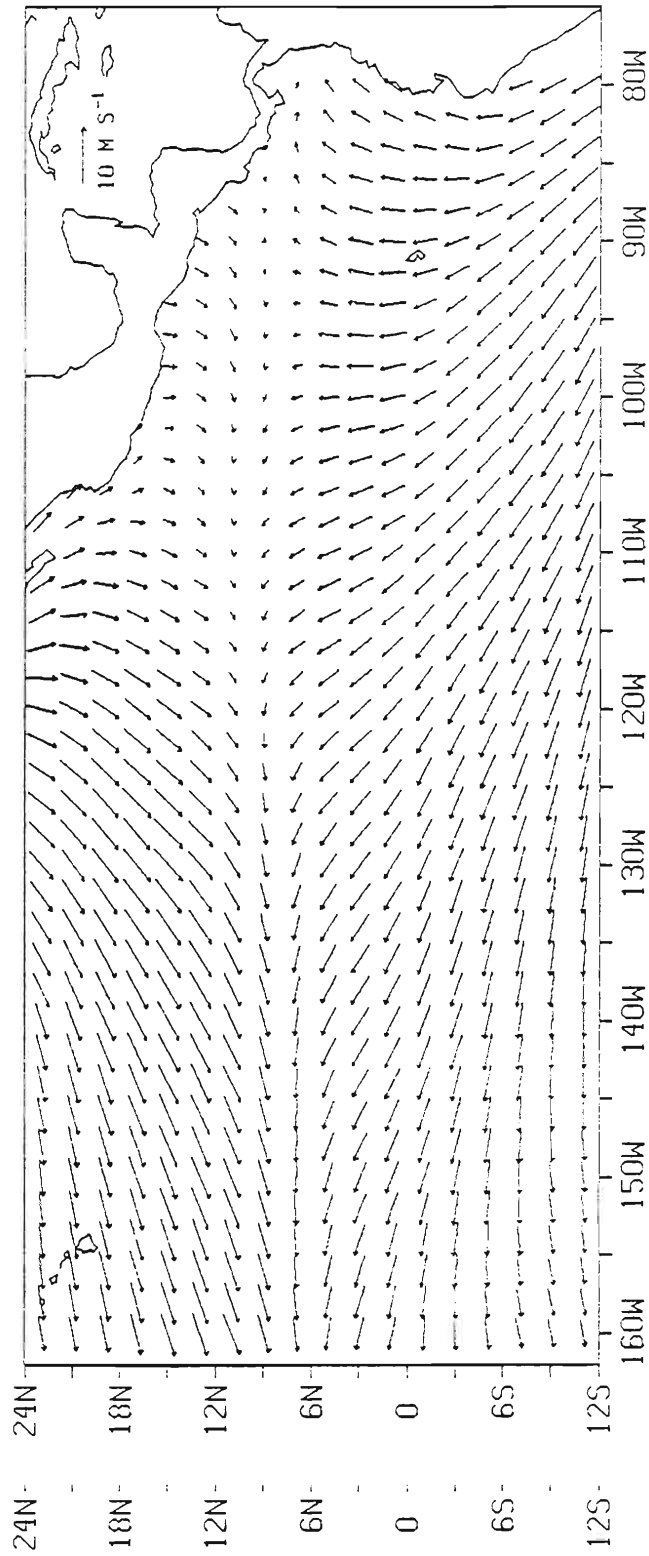


Fig. 6. Annual mean surface wind vectors over the eastern tropical Pacific Ocean. Vector scale is given in upper right corner.

In general, the effect of the Coriolis acceleration causes the southeast trade winds to curve gradually anticyclonically as they cross the equator and progress northward to the trade and monsoon troughs. This effect is quite evident eastward of  $120^{\circ}\text{W}$  (see Fig. 6) and most especially east of  $95^{\circ}\text{W}$  where the southeast winds become southwesterlies. Here the Coriolis effect is accentuated by land-sea monsoonal effects. The anticyclonic turning of the southeast trades west of  $120^{\circ}\text{W}$  is not very apparent as these winds have a pronounced easterly component which results in their trajectories across the equator into the Northern Hemisphere being at quite small angles.

The divergence of the annual mean surface wind field, depicted in Fig. 7, shows a split near-equatorial convergence zone, with a sharp convergence tongue extending from a maximum along the Panamanian coast westward to  $107^{\circ}\text{W}$  and a broader weaker convergence zone centered at  $11^{\circ}\text{N}$ ,  $140^{\circ}\text{W}$ . The more western zone represents the contributions of both the ITCZ and speed convergence within the NE trade winds. The convergence discontinuity between zones, which even appears in the unfiltered mean annual wind divergence field, results from the large seasonal variability of the convergence patterns in this area, which tend to cancel one another in the mean annual signal. The fringes of the South Pacific Convergence Zone (SPCZ) are apparent in the lower left corner of Fig. 7. The strong area of divergence centered off the southern tip of Baja California is due to the veering of the northwest winds off the eastern side of the North Pacific subtropical high into the NE trades. The broad divergence zone from the coast of Peru winds off the eastern side of the North Pacific subtropical high into the NE trades. The broad divergence zone from the coast of Peru westward and equatorward reflects the SE trade wind regime.

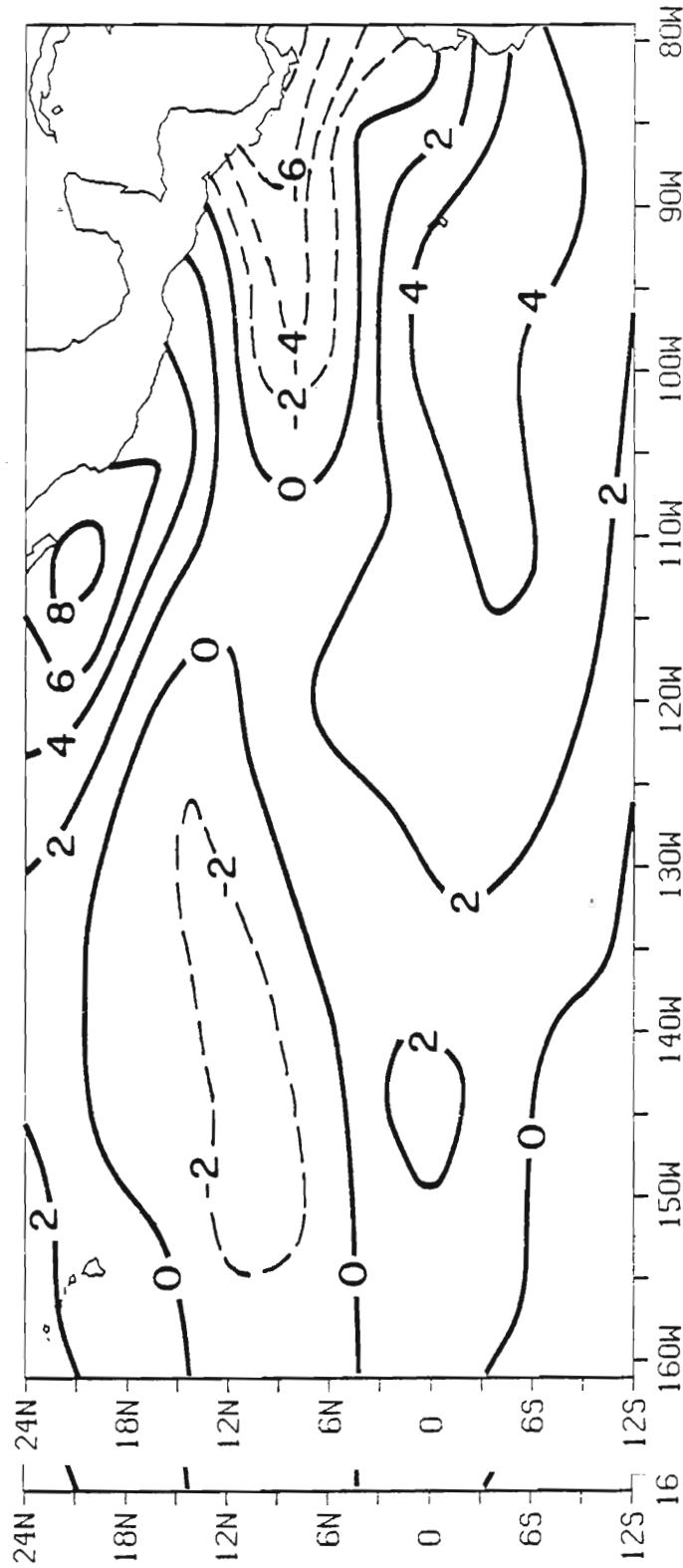


Fig. 7. Annual mean surface wind divergence over the eastern tropical Pacific Ocean. Units of divergence are  $10^{-6} \text{ s}^{-1}$  (solid lines divergence, dashed lines convergence).

The annual mean latitudinal position of the ITCZ in the eastern tropical Pacific Ocean is approximately  $9^{\circ}\text{N}$ , ranging from slightly greater than  $10^{\circ}\text{N}$  for the longitude band  $120\text{-}130^{\circ}\text{W}$  and less than  $8^{\circ}\text{N}$  east of  $90^{\circ}\text{W}$  (Fig. 8). The standard deviation about the annual mean position (see Table 2) decreases westward from  $100^{\circ}\text{W}$ , being slightly less than  $4^{\circ}$  of latitude for the band  $99\text{-}121^{\circ}\text{W}$  and approximately  $2.7^{\circ}$  for the band  $139\text{-}161^{\circ}\text{W}$ . The small standard deviation of  $2^{\circ}$  for the easternmost longitude band  $79\text{-}101^{\circ}\text{W}$  in part reflects latitudinal constraints imposed by the presence of nearby land areas.

Intensity of convergence of the ITCZ corresponding to the annual mean position of the ITCZ, gradually increases eastward from a minimum value slightly less than  $5 \times 10^{-6} \text{ s}^{-1}$  at  $160^{\circ}\text{W}$  to a maximum value of  $1 \times 10^{-5} \text{ s}^{-1}$  at  $97^{\circ}\text{W}$ . A large variation in intensity of convergence for the ITCZ occurs east of  $90^{\circ}\text{W}$ , with a minimum of  $7 \times 10^{-6} \text{ s}^{-1}$  at  $87^{\circ}\text{W}$  and a maximum slightly greater than  $1 \times 10^{-5} \text{ s}^{-1}$  at  $79^{\circ}\text{W}$ . Although care should be used in interpreting derived positions and intensities east of  $90^{\circ}\text{W}$  due to their close proximity to the coast, it is interesting to note that the minimum at  $87^{\circ}\text{W}$  occurs where the ITCZ latitudinal position starts to move rapidly northward. The standard deviation about the annual mean ITCZ intensity of convergence, given in Table 3, shows a gradual eastward increase from  $1.7 \times 10^{-6} \text{ s}^{-1}$  for the band centered at  $150^{\circ}\text{W}$  to  $3.2 \times 10^{-6} \text{ s}^{-1}$  for the band  $79\text{-}101^{\circ}\text{W}$ .

In general, the confluence zone (CZ) exhibiting maximum directional convergence between the two trade wind systems is not synonymous with either the annual mean position of the ITCZ or with the directional convergence between the two trade wind systems is not synonymous with either the annual mean position of the ITCZ or with the axis of maximum convergence as seen on the annual wind divergence map.

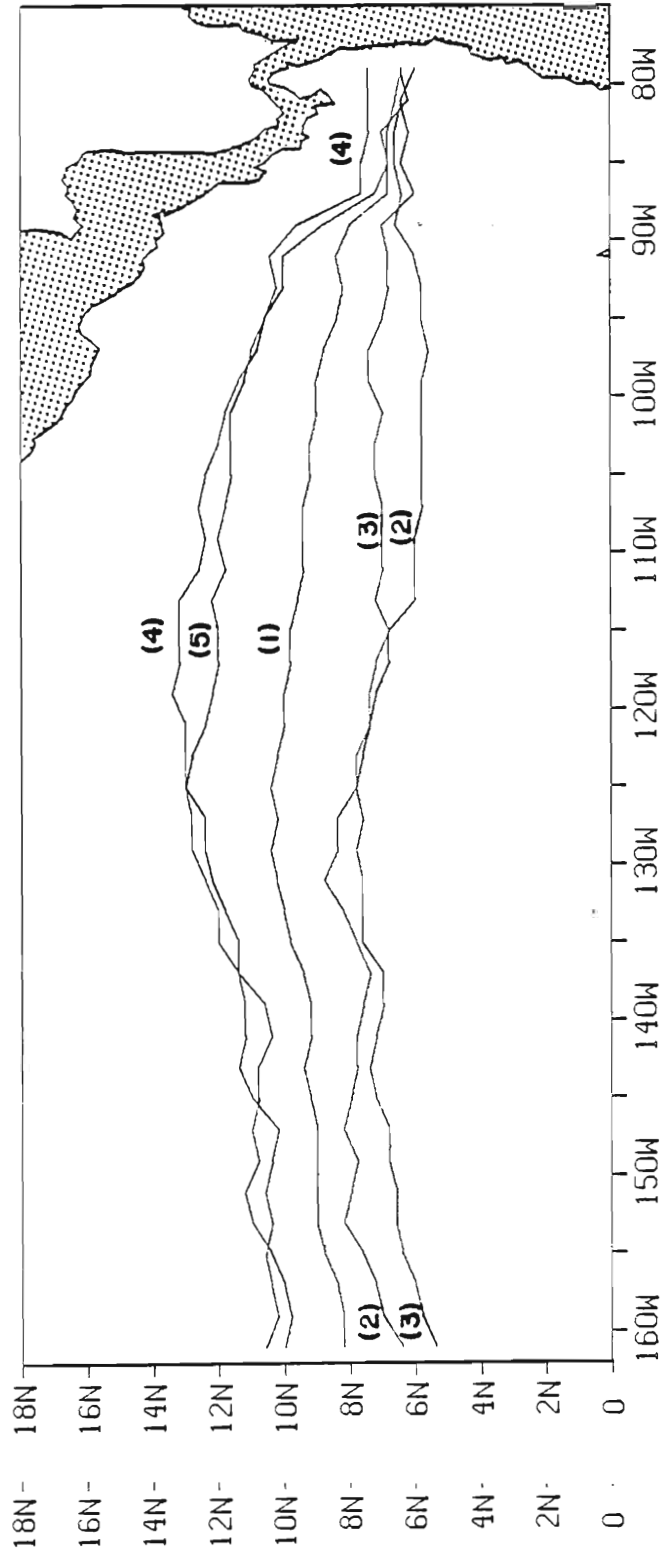


Fig. 8. Annual and seasonal mean latitudinal positions of the ITCZ.  
 Legend: (1) Annual, (2) December, January, February season,  
 (3) March, April, May season, (4) June, July, August season,  
 and (5) September, October, November season.

In theory, the position of the ITCZ, which represents a best fit to the axis of maximum convergence within the near-equatorial convergence zone, should be synonymous with the axis of maximum convergence of the corresponding divergence map. Differences between the two are the result of the application of the ITCZ analysis method which essentially is a nonlinear process. Thus, the derived ITCZ annual position (Fig. 8) superimposed on the axis of maximum convergence of the annual divergence map (Fig. 7) reveals incongruities, with the ITCZ position being in general slightly south of the convergence axis west of  $110^{\circ}\text{W}$  and near or slightly south of it east of that longitude. Superposition of the annual ITCZ position upon the annual mean surface wind vector field (Fig. 6) indicates that only near  $115^{\circ}\text{W}$  do the CZ and ITCZ latitudinal positions agree, with the ITCZ position being several degrees north of the CZ axis west of this longitude and in general slightly south of the CZ axis eastward from  $115^{\circ}\text{W}$ .

#### b. SEASONAL

In this section, the general features of the seasonal cycle of the ITCZ latitudinal position, the surface wind, and the divergence of the surface wind, based on Figs. 8, 9, and 10, respectively, are described. This is followed by an in-depth study of the seasonal variability of the ITCZ.

The December, January, February season (DJF) is characterized by a well-developed NE trade wind system (see Fig. 9a) extending from the American coast westward across the NE tropical Pacific Ocean with maximum wind speeds exceeding  $8 \text{ m s}^{-1}$ . Trade winds off the coasts of southern Mexico and Central America are accentuated by frequent



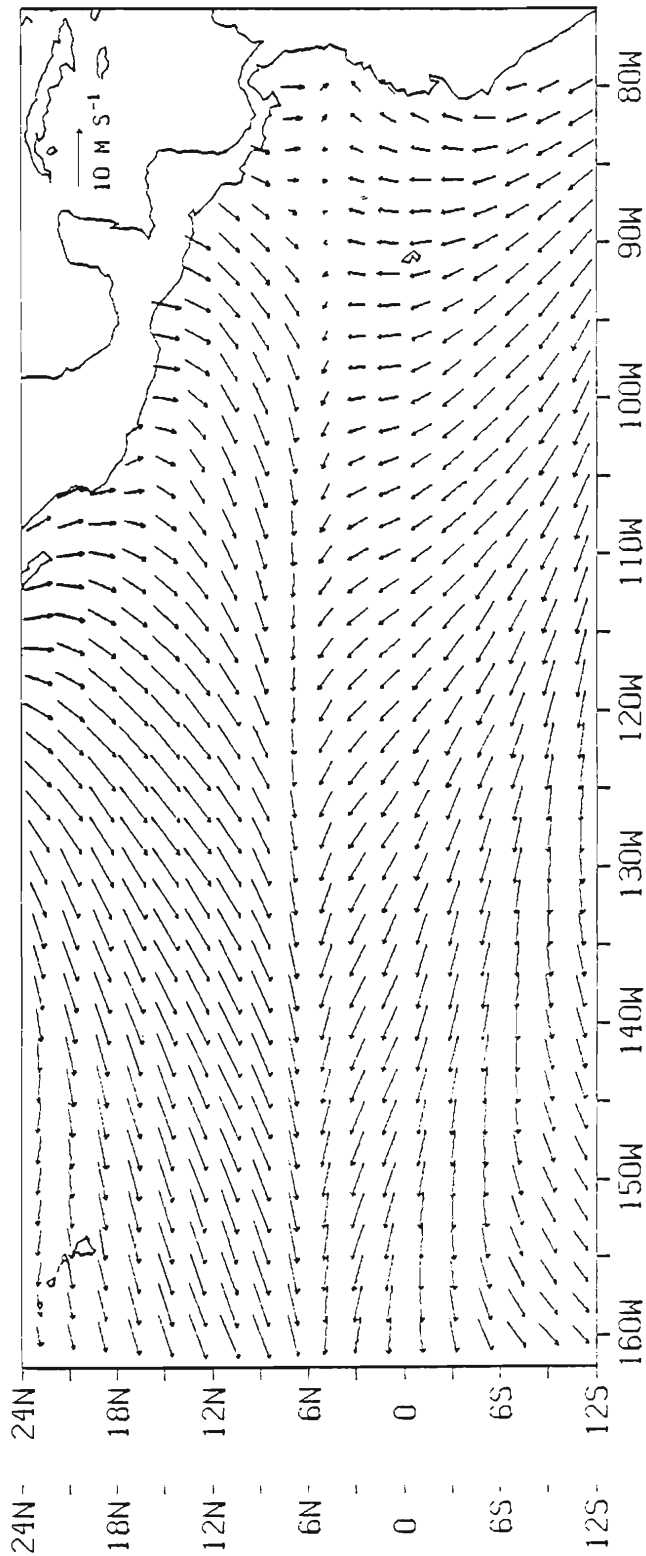


Fig. 9. (a) Mean surface wind vectors over the eastern tropical Pacific Ocean for December, January, February season. Vector scale is given in upper right corner.

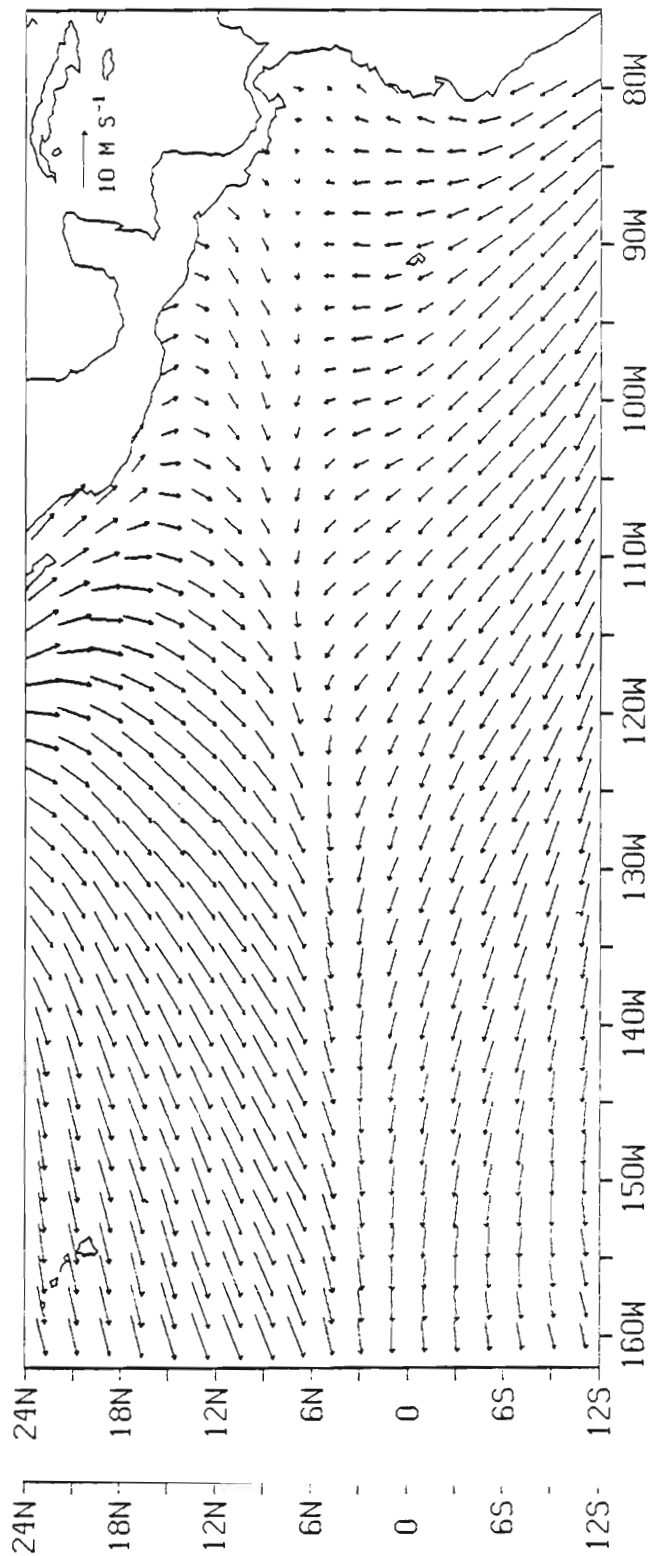


Fig. 9. (b) Similar to (a) but for March, April, May season.

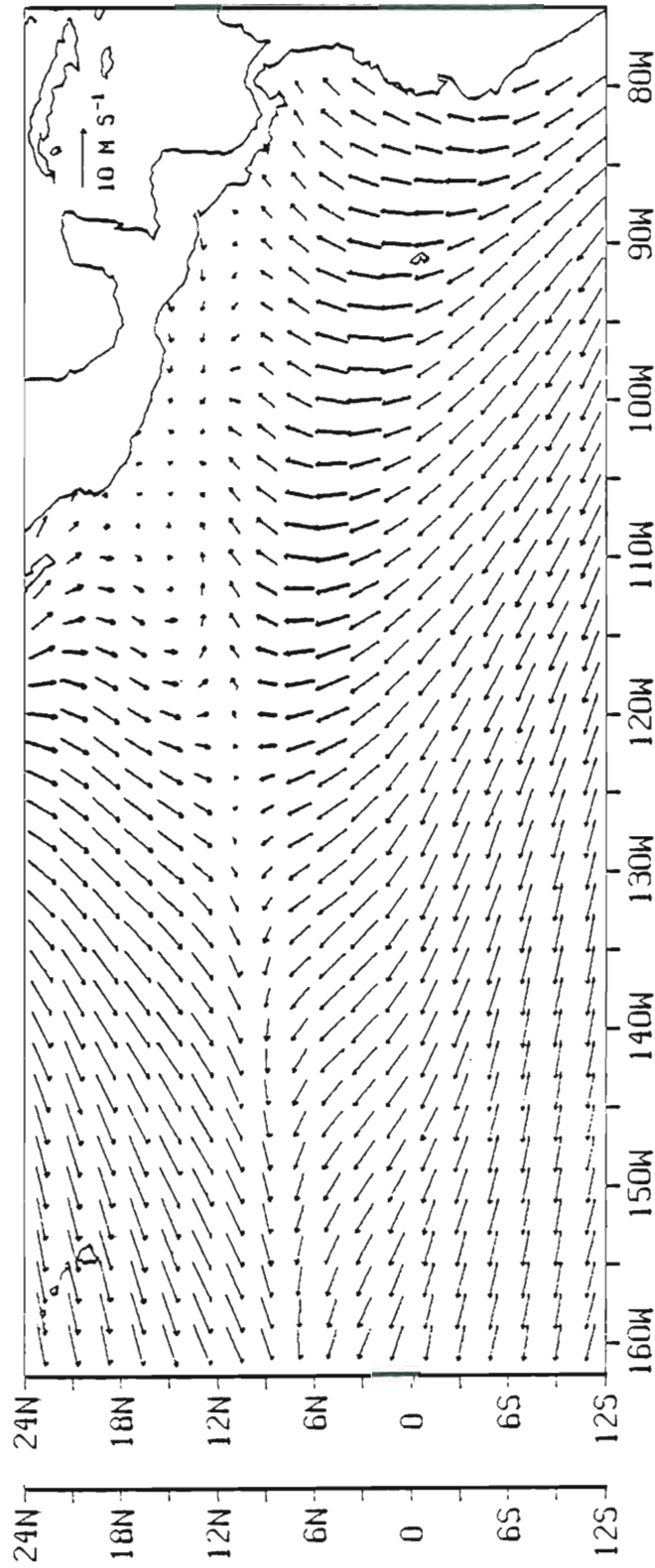


Fig. 9. (c) Similar to (a) but for June, July, August season.

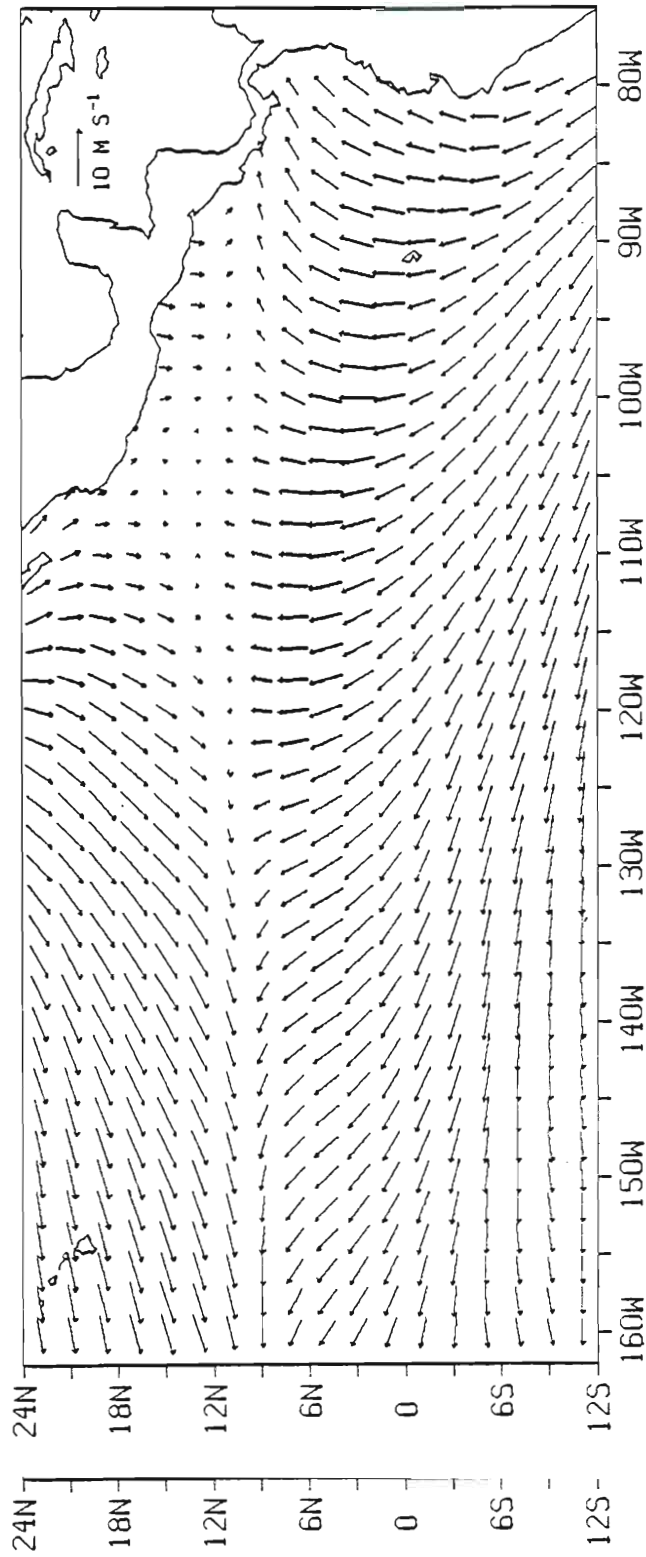


Fig. 9. (d) Similar to (a) but for September, October, November season.

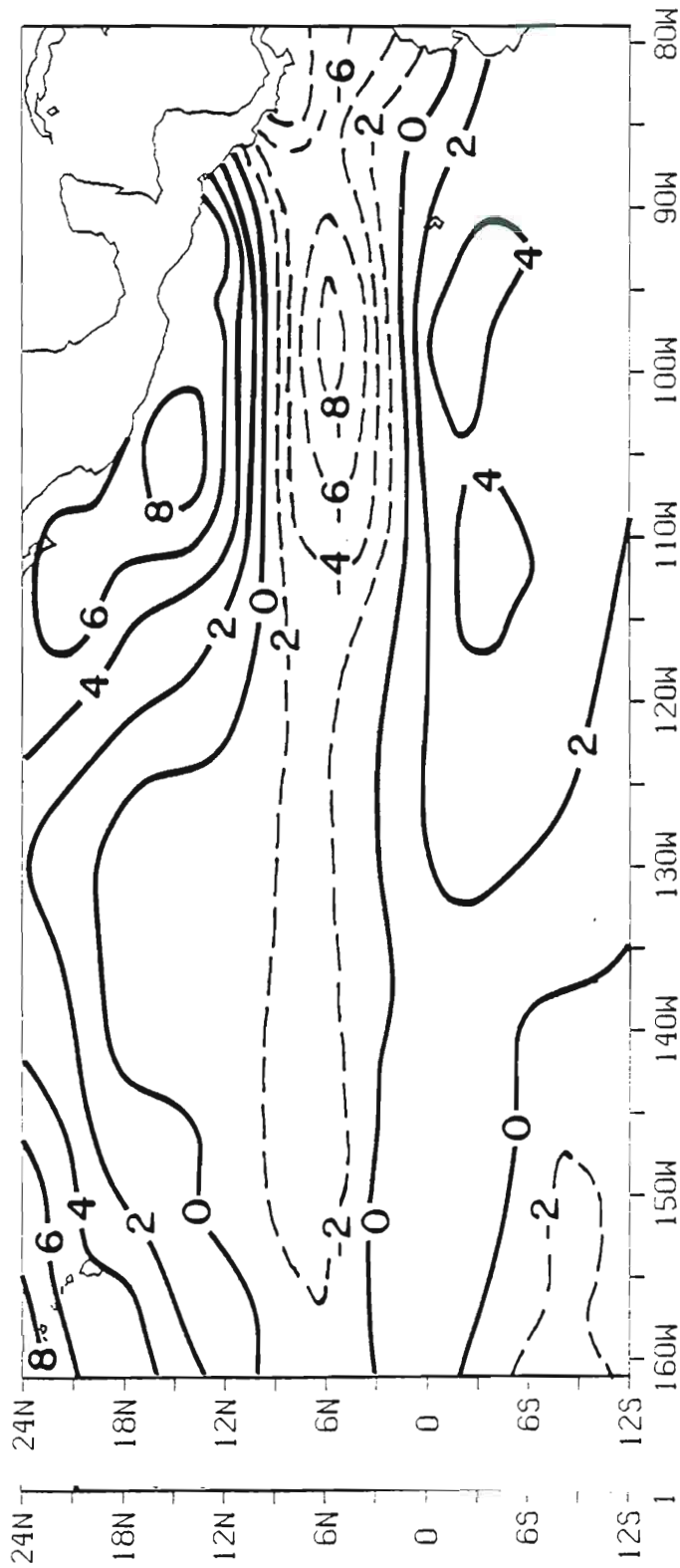


Fig. 10. (a) Mean surface wind divergence over the eastern tropical Pacific Ocean for December, January, February season. Units of divergence are  $10^{-6} \text{ s}^{-1}$  (solid lines divergence, dashed lines convergence).

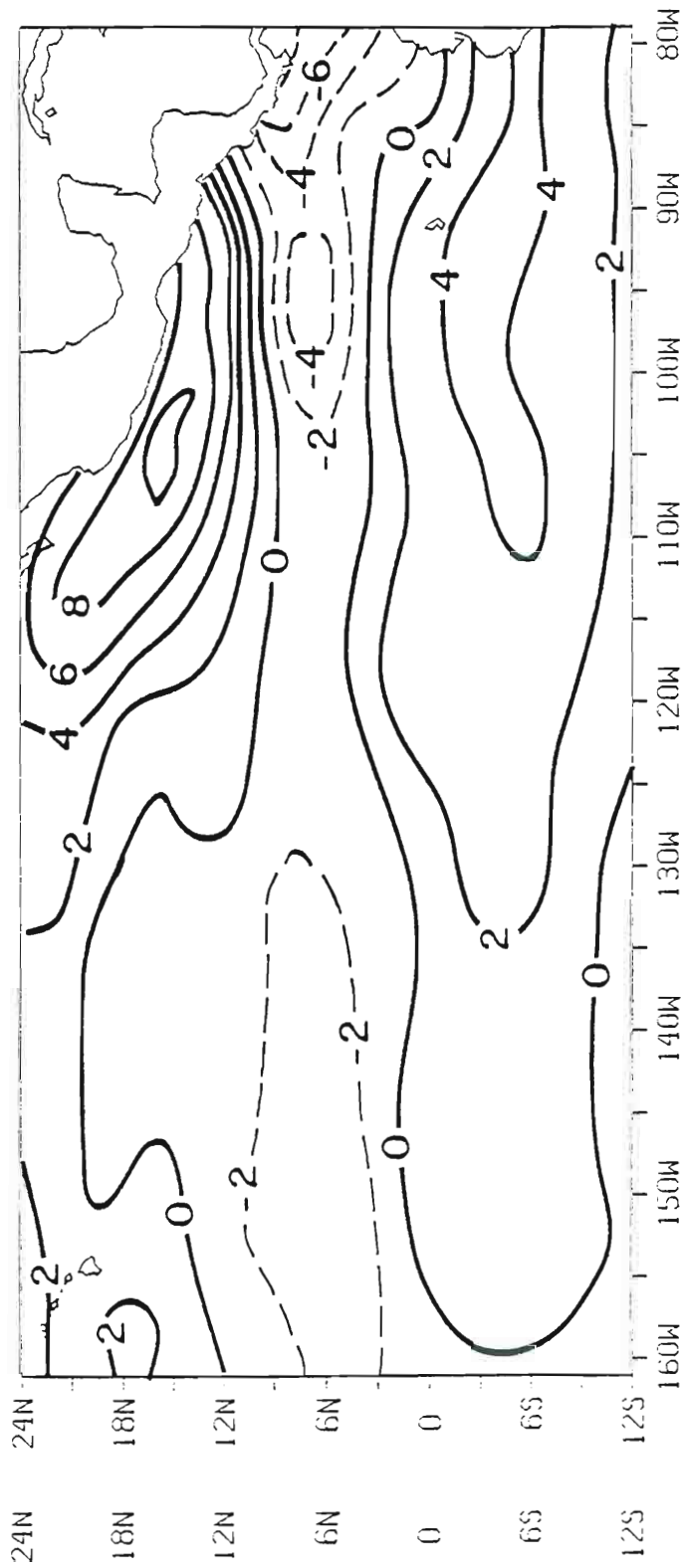


Fig. 10. (b) Similar to (a) but for March, April, May season.

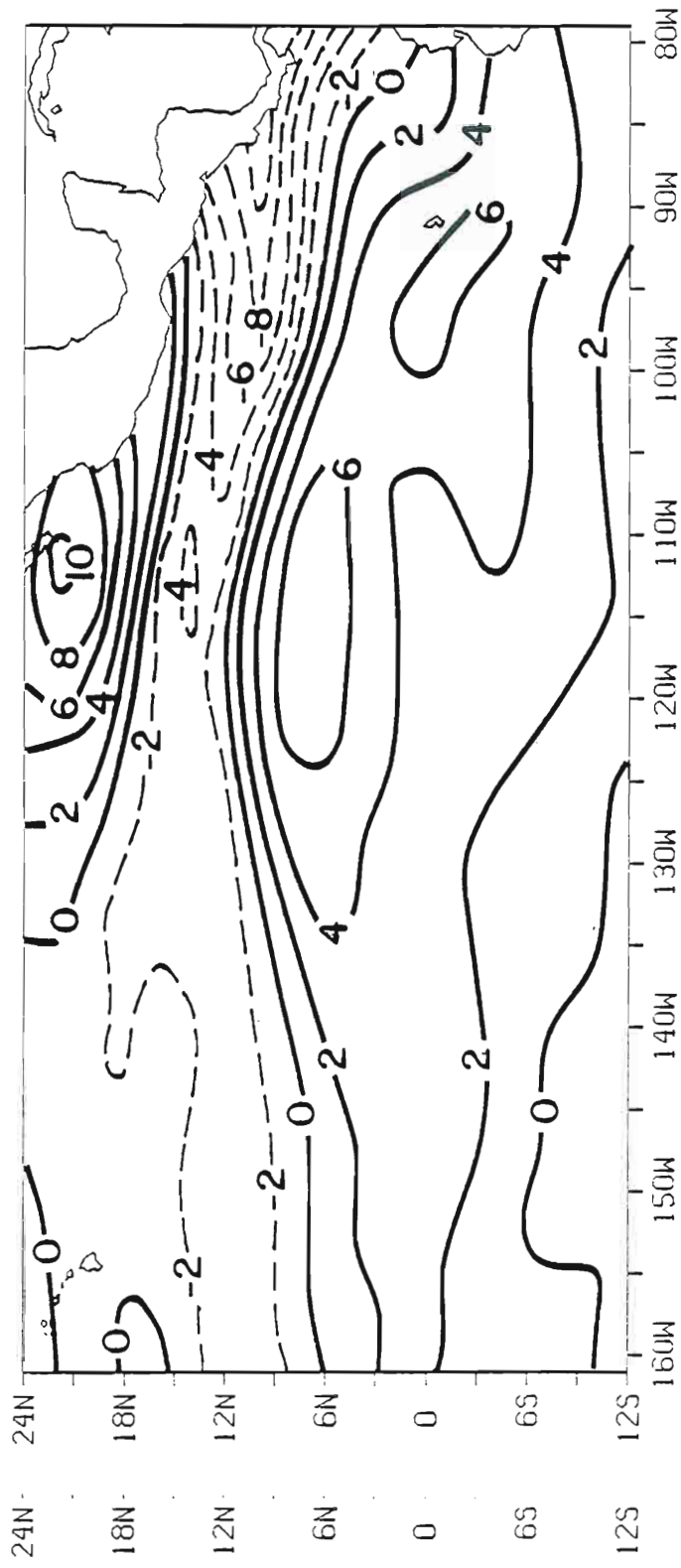


Fig. 10. (c) Similar to (a) but for June, July, August season.

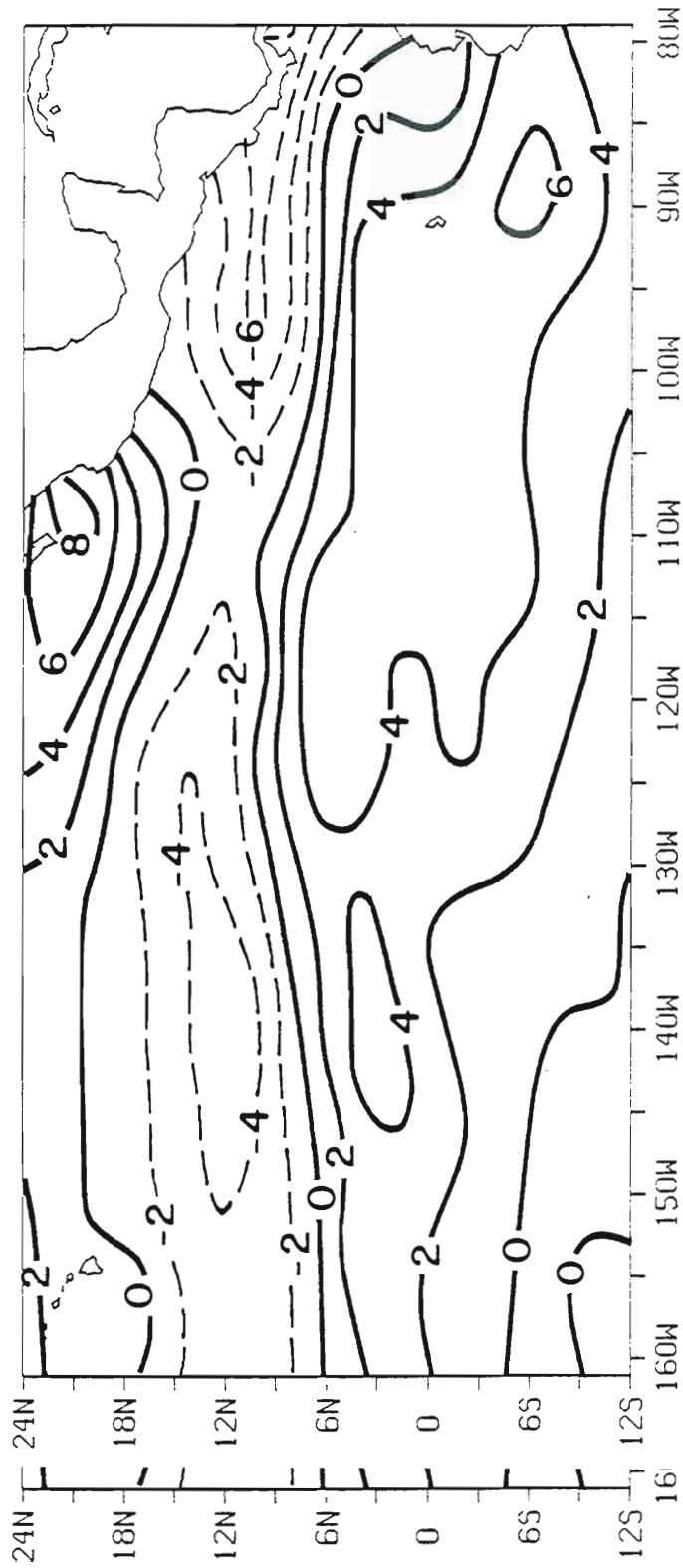


Fig. 10. (d) Similar to (a) but for September, October, November season.



intrusions of polar air masses funnelled through mountain passes, known locally as "Tehuantepecos" in Mexico and "Papagayos" in regions of Central America. The southeast trades are extensive but of only moderate average intensity. A sharp E to NE turning and slowing down of these winds is noted west of  $145^{\circ}\text{W}$  and south of  $5^{\circ}\text{S}$ . Southwest winds are confined to a narrow zone along the South American coast. For this season, the axis of the near-equatorial confluence zone across the eastern tropical Pacific Ocean can accurately be described as a trade wind trough.

Strong areas of divergence (Fig. 10a) are found in the Northern Hemisphere northwestward from Hawaii and southwest of Mexico. The latter area, centered near  $15^{\circ}\text{N}$ ,  $105^{\circ}\text{W}$ , results from the combined effects of speed divergence and diffluence of the trade winds in the area. A near-equatorial axis of maximum convergence is positioned approximately along  $6^{\circ}\text{N}$  with centers of maximum intensity at  $100^{\circ}\text{W}$  and near Panama. The northward bulge from this convergence axis to almost  $20^{\circ}\text{N}$  at  $130^{\circ}\text{W}$  reflects speed convergence within the northeast trades. Westward and equatorward from the Peruvian coast is a large area of divergence associated with the SE trade wind field. Maximum divergence within this region is located just south of the equator from approximately  $90^{\circ}\text{W}$  to  $120^{\circ}\text{W}$ . A significant near-equatorial convergence axis is located along  $8^{\circ}\text{S}$  west of  $145^{\circ}\text{W}$ . The intensity of convergence within this zone is equal to or slightly larger than the intensity within the northern near-equatorial convergence zone for the same longitude domain.

within the northern near-equatorial convergence zone for the same longitude domain.

The derived ITCZ mean latitudinal position for DJF, given in Fig. 8, is approximately  $7^{\circ}\text{N}$ , varying from less than  $6^{\circ}$  from  $90^{\circ}\text{W}$  to  $115^{\circ}\text{W}$  to near  $8^{\circ}\text{N}$  for the longitude band  $125\text{-}155^{\circ}\text{W}$ . This ITCZ position corresponds well with the axis of the northern convergence zone depicted in Fig. 10a. On the other hand, the ITCZ position is generally a few degrees of latitude north of the axis of maximum wind confluence of Fig. 9a for longitudes west of  $125^{\circ}\text{W}$  as well as near the Central American coast.

The surface wind field for the March, April, May (MAM) season, depicted in Fig. 9b, is generally quite similar to the DJF wind field. Nonetheless, some rather significant differences are observable. The sharp E to NE turning of the winds associated with the DJF southern near-equatorial zone disappears during MAM and is replaced by a zonal easterly flow. The NE trade winds during MAM expand slightly southward west of  $120^{\circ}\text{W}$ . In response to this movement, the Southern Hemisphere trade winds north of the equator become more easterly. The NE trade wind vectors of the MAM season east of  $120^{\circ}\text{W}$  are rotated approximately  $30^{\circ}$  counterclockwise from the DJF vectors over the same area. An increase in trade wind speeds in the vicinity of Hawaii is noted during MAM. On the contrary, the intensity of the NE winds located south of Mexico and west of Central America during DJF decreases markedly in MAM.

Inspection of the wind divergence map for MAM (Fig. 10b) reveals that the strong DJF divergence zone northwestward from Hawaii has disappeared. However, the strong areas of divergence located southwest of Mexico and westward from the South American coast remain firmly

established during the MAM season. A slight northward shift of the southernmost of these divergence regions is observed between  $90^{\circ}\text{W}$  and  $125^{\circ}\text{W}$ . The intensities of divergence within these regions during MAM are comparable to those of the previous season. The DJF southern near-equatorial convergence zone is replaced east of  $155^{\circ}\text{W}$  by positive divergence values during MAM. The northern near-equatorial zone east of  $120^{\circ}\text{W}$  narrows, shifts slightly northward, and weakens in MAM, with its maximum intensity of convergence at  $95^{\circ}\text{W}$  being approximately half of the DJF maximum convergence value located near  $98^{\circ}\text{W}$ .

The mean MAM latitudinal position of the ITCZ across the eastern tropical Pacific Ocean (Fig. 8), at slightly less than  $7^{\circ}\text{N}$ , is essentially unchanged from the DJF mean seasonal position. Nonetheless, a comparison between the DJF and MAM positions reveals interesting longitudinal variations. During the MAM season, for the longitude range  $90^{\circ}\text{W}$  to  $115^{\circ}\text{W}$ , the ITCZ position is about  $1^{\circ}$  of latitude north of its DJF position. West of  $125^{\circ}\text{W}$ , the opposite situation occurs; the latitudinal position during the MAM season is south of the DJF position by about  $1^{\circ}$  of latitude. Further comparisons show that the MAM latitudinal position of the ITCZ agrees quite well with the axis of maximum convergence of the near-equatorial convergence zone of Fig. 10b but for longitudes west of  $120^{\circ}\text{W}$  it is found to be displaced a few degrees north of the axis of maximum directional convergence of Fig. 9b.

The arrival of the June, July, August season (JJA) brings about marked and rapid changes in the ITCZ latitudinal position and the surface wind and divergence fields. It is during this season that the marked and rapid changes in the ITCZ latitudinal position and the surface wind and divergence fields. It is during this season that the Northern Hemisphere has its maximum exposure to the sun. Concurrently,

tropical storm activity is at its maximum in the NE tropical Pacific Ocean.

The JJA surface wind field (Fig. 9c) is dominated by an extensive and strong SE trade wind regime. Maximum wind speeds are near  $8 \text{ m s}^{-1}$  in the core of the southeast trades with speeds  $> 5 \text{ m s}^{-1}$  common north of the equator. East of  $120^\circ\text{W}$  the SE trade winds become monsoon southwesterlies as they progress northward toward the monsoon trough. The latitudinal position of the monsoon trough is near or slightly north of  $12^\circ\text{N}$  between  $100^\circ\text{W}$  and  $120^\circ\text{W}$ . The area of light and variable winds southwest of Mexico in the vicinity of this monsoon trough is one of high tropical storm activity and resulting low wind constancy. The thrust of the SE trade winds across the equator results in a northward displacement of the northeast trades. Nonetheless, strong wind speeds ( $\sim 7.5 \text{ m s}^{-1}$ ) within these trades are found in the vicinity of Hawaii. The axis of maximum directional convergence west of  $120^\circ\text{W}$ , best described as a trade wind trough, is situated at approximately  $12^\circ\text{N}$  at  $120^\circ\text{W}$  and near  $7^\circ\text{N}$  at  $160^\circ\text{W}$ .

The JJA enhancement and northward movement of the SE trade winds has a reciprocal effect on the wind divergence field (Fig. 10c). Positive divergence associated with these southeast trades reaches its northern apex,  $11^\circ\text{N}$ , near  $118^\circ\text{W}$ . Southward from this point a strong divergence center is found at  $6^\circ\text{N}$ . Another core of strong divergence is located just west of the Galapagos Islands. The strong divergence center that was located off the southwest Mexican coast during MAM has shifted rapidly northwestward to just south of Baja California during JJA. Strong gradients in the divergence are found inward from these

three centers of divergence to the axis of the near-equatorial convergence zone. The intensity of convergence within this near-equatorial convergence zone during JJA is quite strong, most especially from  $100^{\circ}\text{W}$  eastward to the Central American coast and immediately south of Panama, where values exceed  $8 \times 10^{-6} \text{ s}^{-1}$ . The axis of maximum convergence within this zone splits near  $130^{\circ}\text{W}$ . The southern axis continues westward, along the same general path as the derived JJA latitudinal position of the ITCZ. The northern axis goes WNW toward Hawaii with rapidly diminishing intensity beyond  $145^{\circ}\text{W}$ . This northern axis is thought to result from the combined effects of speed convergence within the NE trade wind regime and a mean northern summer tropical cyclone path across the NE tropical Pacific Ocean.

The ITCZ latitudinal position, which follows the sun throughout the year, achieves on the average its most northerly position during the JJA season (Fig. 8). It is furthest north at  $120^{\circ}\text{W}$ , reaching approximately  $13^{\circ}\text{N}$ . East of  $87^{\circ}\text{W}$ , its position is between  $7^{\circ}\text{N}$  and  $8^{\circ}\text{N}$ . The ITCZ mean JJA position moves very rapidly northward between  $87^{\circ}\text{W}$  and  $91^{\circ}\text{W}$ . Comparison of the derived ITCZ latitudinal position with the axis of maximum convergence on the divergence map (Fig. 10c) indicates good latitudinal agreement west of  $90^{\circ}\text{W}$  and poor agreement east of that longitude, the ITCZ position there being a few degrees south of the maximum convergence axis. Finally, the ITCZ position for JJA is slightly north of the JJA near-equatorial axis of maximum directional convergence (see Fig. 9c) for longitudes west of  $110^{\circ}\text{W}$  and south of the axis for longitudes eastward from that meridian, with a difference of convergence (see Fig. 9c) for longitudes west of  $110^{\circ}\text{W}$  and south of the axis for longitudes eastward from that meridian, with a difference of several degrees noted near the Central American coast.

The main features of the surface wind field for the September, October, November season (SON), depicted in Fig. 9d, are essentially unchanged from those of the previous season. The SE trade winds continue extensive, pushing well into the Northern Hemisphere. A strong clockwise turning cross-equatorial monsoon flow persists and is especially prominent east of  $100^{\circ}\text{W}$ . The area of light and variable winds off the southwest Mexican coast during JJA still is present during SON. Immediately east of this area, the observed JJA easterly winds are seen to be almost northerly during SON. The trade wind trough west of  $125^{\circ}\text{W}$  is well developed in SON, its axis of maximum directional convergence being near or slightly north of the JJA latitudinal position for the longitude band  $125\text{-}160^{\circ}\text{W}$ .

The surface wind divergence field over the eastern tropical Pacific Ocean (Fig. 10d) during SON is generally quite similar to that of the previous season. Nonetheless, a few significant changes do occur; perhaps the most striking of these is the appearance of a convergence maximum, centered at  $12^{\circ}\text{N}$  and  $140^{\circ}\text{W}$ , within the near-equatorial convergence zone. A convergence minimum within the zone at  $110^{\circ}\text{W}$  separates this "western" maximum from the more eastern convergence maximum located along  $9^{\circ}\text{N}$  from  $100^{\circ}\text{W}$  to the American coast. The intensity of convergence within the "eastern" maximum is considerably smaller than the JJA intensity of convergence within the same region. The SON divergence area associated with the southeast trades is slightly altered from that of the previous season. During SON, a divergence maximum appears at  $3^{\circ}\text{N}$ ,  $140^{\circ}\text{W}$ . The center that was located slightly altered from that of the previous season. During SON, a divergence maximum appears at  $3^{\circ}\text{N}$ ,  $140^{\circ}\text{W}$ . The center that was located near  $6^{\circ}\text{N}$  and  $115^{\circ}\text{W}$  during JJA has diminished. The maximum near the

Galapagos Islands has shifted southeastward during SON. The divergence maximum located off the tip of Baja California in JJA persists into SON, albeit slightly weaker.

The latitudinal position of the ITCZ during SON (see Fig. 8) is near or slightly south of its JJA position eastward from about  $140^{\circ}\text{W}$  and is actually further north of the JJA position at some longitudes between  $140^{\circ}\text{W}$  and  $160^{\circ}\text{W}$ . This result indicates that the solar radiation received by the earth within the tropics north of the equator during SON is sufficient enough to maintain the ITCZ far north of the equator over the eastern tropical Pacific Ocean at a mean position of about  $11^{\circ}\text{N}$ . The ITCZ latitudinal position for SON is slightly north of the SON axis of maximum directional convergence (Fig. 9d) west of  $120^{\circ}\text{W}$  and south of the axis eastward from  $90^{\circ}\text{W}$ . The axis of maximum convergence within the near-equatorial convergence zone, estimated from Fig. 10d, agrees well with the ITCZ position west of  $100^{\circ}\text{W}$  but is farther north eastward from that meridian, most especially near the American coast.

In order to examine further the structure of the ITCZ, maps of the seasonal variation in the ITCZ latitudinal position (Fig. 11) and the seasonal variability in the standard deviation of the ITCZ latitudinal position (Fig. 12) are provided. Similar maps describing the seasonal variation in the intensity of convergence of the ITCZ and the seasonal variability in the standard deviation of the ITCZ intensity of convergence are presented as Figs. 13 and 14, respectively. All four of these maps are constructed from monthly values given for each  $2^{\circ}$  of longitude from  $79^{\circ}\text{W}$  to  $161^{\circ}\text{W}$ . This implies that the base data input for any

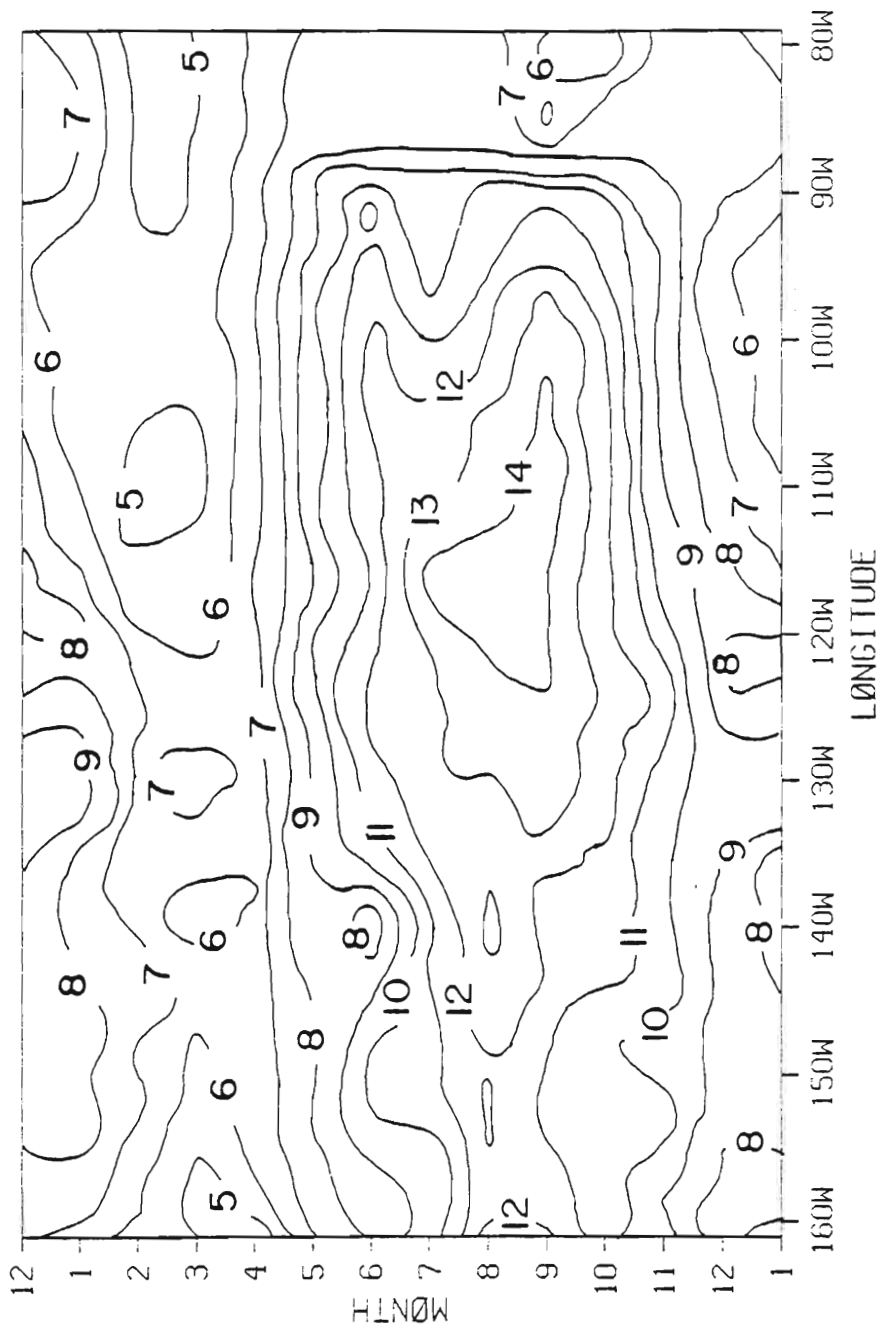


Fig. 11. Seasonal variation in the latitudinal position of the ITCZ. Contours are in degrees of latitude north.



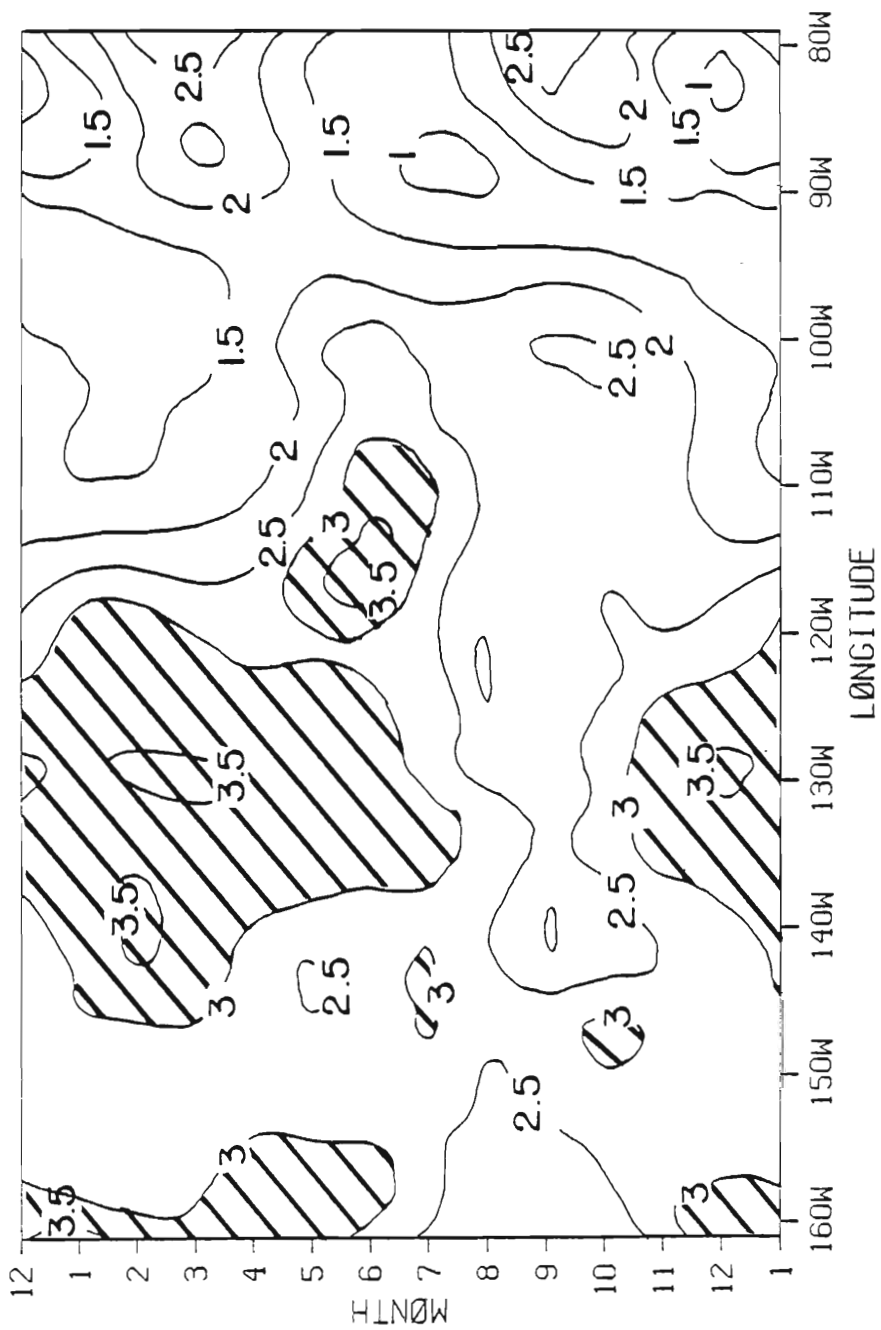


Fig. 12. Seasonal variation in the standard deviation of the IICZ latitudinal position. Contour units are degrees of latitude. Areas of standard deviation  $> 3^\circ$  are hatched.

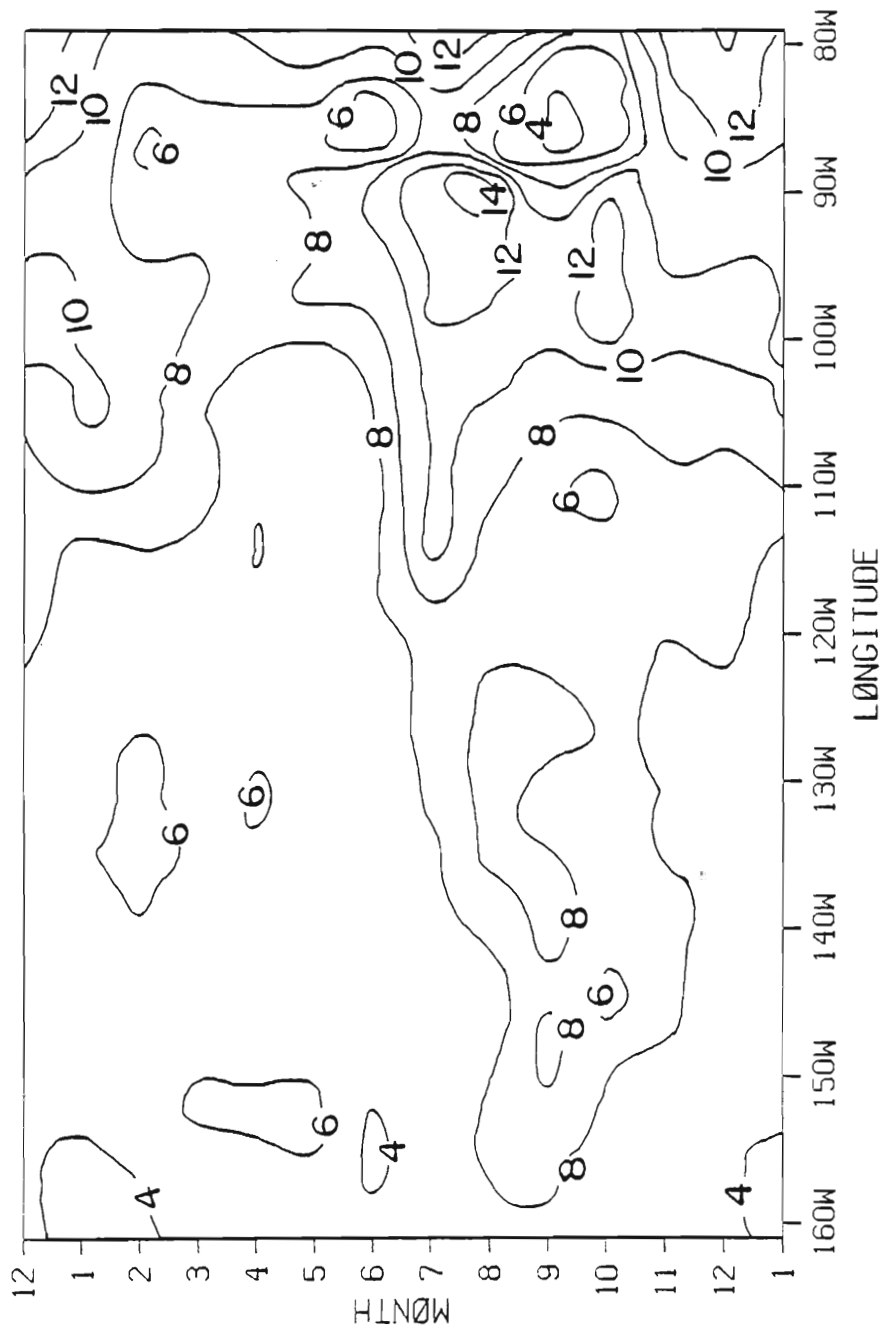


Fig. 13. Seasonal variation in the intensity of convergence of the ITCZ. Units of convergence are  $10^{-6} \text{ s}^{-1}$ .

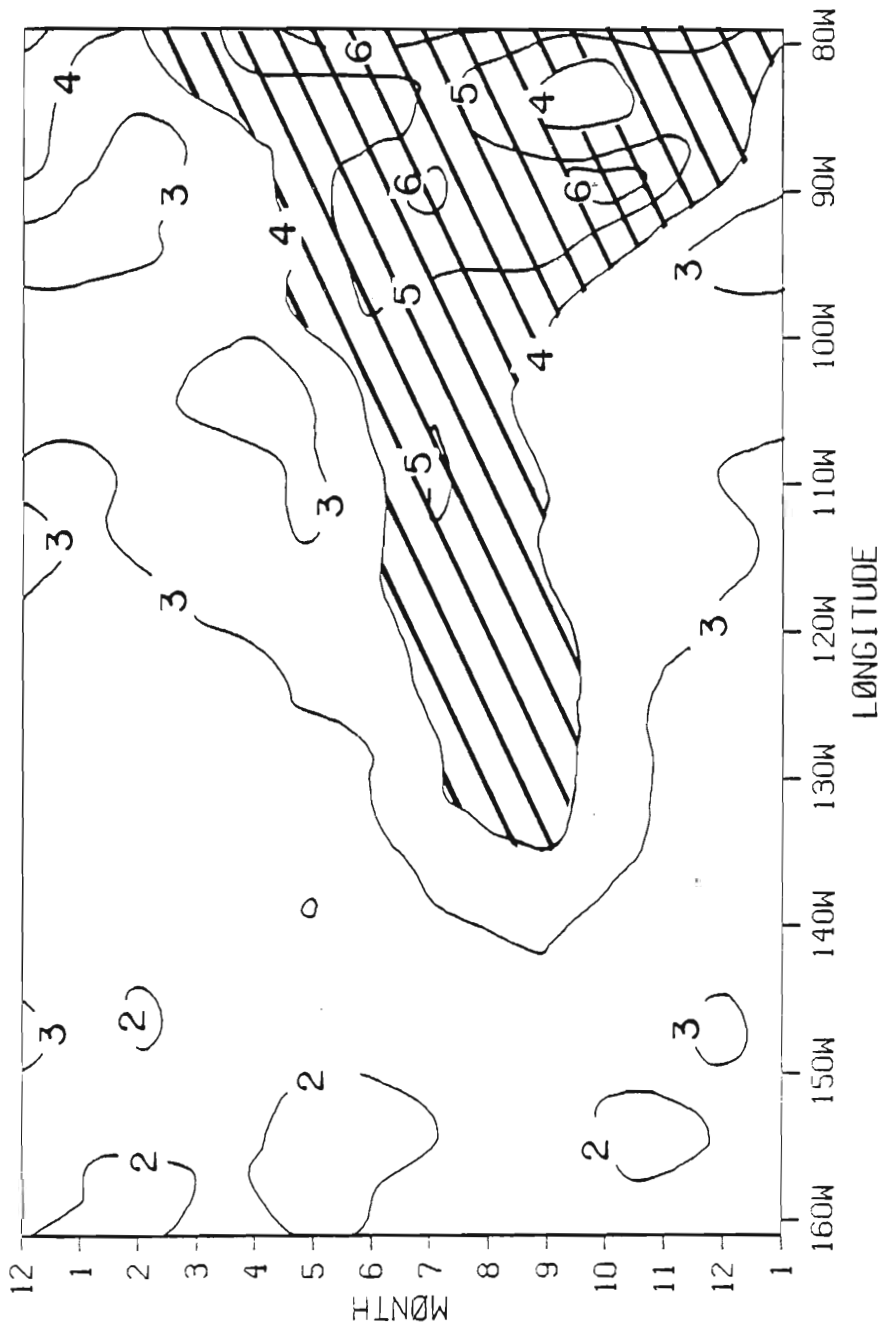


Fig. 14. Seasonal variation in the standard deviation of the ITCZ intensity of convergence. Contour units are  $10^{-6} \text{ s}^{-1}$ . Areas of standard deviation  $> 4 \times 10^{-6} \text{ s}^{-1}$  are hatched.

particular element consists of an  $(x,t)$  lattice of  $42 \times 12$  points. Numbered tick marks along the ordinate of Figs. 11-14 correspond to the middle of the months. Excessive noisiness in the standard deviation data fields (Figs. 12 and 14) was reduced somewhat by application of a 1-2-1 filter in both the N-S and E-W directions. The effect of this filtering is a loss of information in the signal below  $6^\circ$ .

The pronounced large annual variability in the latitudinal position of the ITCZ across the eastern tropical Pacific Ocean is the most outstanding feature portrayed by Fig. 11. Variations greater than  $5^\circ$  of latitude occur west of  $90^\circ\text{W}$  with the maximum variability, of the order of  $9^\circ$  of latitude, occurring within the longitude band  $110\text{--}120^\circ\text{W}$ . Continental influences keep the observed seasonal variation moderate eastward from  $90^\circ\text{W}$ .

Longitudinal dependence of the seasonal variability of the ITCZ position is another important feature. Nonetheless, the very nature of this seasonal variability across the eastern Pacific makes it difficult to define precisely its longitudinal dependence. An examination of Fig. 11 suggests that the seasonal variability is significantly different within at least three distinct longitude bands. A discussion of each of these arbitrarily chosen longitude bands follows.

The easternmost band, chosen from  $79^\circ\text{W}$  to  $90^\circ\text{W}$ , exhibits the smallest seasonal variability in the ITCZ position of any longitude band. This low seasonal variability, as well as probable too far south derived ITCZ positions during northern summer, are due in great part to restrictions imposed by adjacent land masses over which no input data derived ITCZ positions during northern summer, are due in great part to restrictions imposed by adjacent land masses over which no input data is available for ITCZ calculations. Such restrictions are most notable

east of  $87^{\circ}\text{W}$  where the most northerly possible grid location for an ITCZ calculation is  $8^{\circ}\text{N}$ .

The most interesting feature of the  $79\text{-}90^{\circ}\text{W}$  band is its bimodal structure with two distinct south positions observed during the year. The more southern of these ITCZ positions, slightly less than  $5^{\circ}\text{N}$ , occurs in late February. During September and October, the ITCZ position achieves a secondary south position, ranging from near  $5^{\circ}\text{N}$  at the coast to  $7^{\circ}\text{N}$  at  $87^{\circ}\text{W}$ . The cause of the southward shift in September and October is unclear. Inspection of the full 18-year data record indicates that during approximately half of all the years a September-October southward shift of the ITCZ occurs near the coast. In addition, its occurrence does not appear to be related to any known interannual ocean-atmosphere variability, such as El Niño.

The next band to be discussed is that from  $90\text{-}110^{\circ}\text{W}$ . The most southerly position of the ITCZ within this band, about  $5^{\circ}\text{N}$ , occurs in late February. A rapid northward movement starts by late April and continues into June when the ITCZ reaches the first of its two north positions. A slight southward movement of  $1\text{-}2^{\circ}$  of latitude occurs in July. In August, the ITCZ reverses direction and again heads northward, reaching its most northerly position during September. A rapid southward movement is observed during October and November, but gradually slows as northern winter is approached.

The slight southward movement of the ITCZ observed during July is interesting and deserves further study. Visual inspection of Fig. 3a reveals that a southward shift of the ITCZ latitudinal position occurs interesting and deserves further study. Visual inspection of Fig. 3a reveals that a southward shift of the ITCZ latitudinal position occurs during northern summer, most especially in July or August, for many

years of the data record. Alpert (1945), in a detailed study of the ITCZ in the eastern Pacific Ocean, found a southward movement of the ITCZ between 90°W and 95°W during July-August. Hastenrath and Lamb (1978) showed a southward shift of about 2° of latitude from July to September in the axis of maximum convergence within the longitude band 80-100°W. Alpert stated that this southward movement results from the westward extension of a ridge from the Bermuda High into the western Caribbean. This explanation seems plausible in light of the behavior of the wind field immediately west of Central America from June through September. Derived monthly wind field maps for these months (not given in this report) indicate variable or light southwesterly winds north of 10°N and east of 100°W during June and September but easterly winds within the same region during July and August, with those of July of greater intensity. Similar results have been obtained by Wyrcki and Meyers (1975), Hastenrath and Lamb (1977), and Weare et al. (1980). These wind patterns agree well with the notion that the existence of a ridge from the Bermuda High into the western Caribbean would result in an enhanced easterly trade wind flow across the Caribbean through Central America and into the eastern tropical Pacific and the absence of such a ridge would permit southwesterly monsoon flow to penetrate northward in the Pacific Ocean along the Central American coast.

East of 90°W, no significant changes are noted in the ITCZ latitudinal position during July. It is believed that aforementioned analysis restrictions cause the derived July ITCZ position of 7-8°N to be a few degrees too far south so as not to be affected appreciably by analysis restrictions cause the derived July ITCZ position of 7-8°N to be a few degrees too far south so as not to be affected appreciably by the westward ridge extension into the Caribbean. Indeed, further

north, at the latitude of Costa Rica ( $\sim 10^\circ\text{N}$ ), dynamic processes associated with the ridge extension across the zone bring about annually a welcomed dry period during July, known locally as the "veranillo," or little summer.

The seasonal variability within the extensive band from  $110^\circ\text{W}$ - $161^\circ\text{W}$  is quite complex. The ITCZ is further south, at slightly less than  $5^\circ\text{N}$ , near the end of February at  $110^\circ\text{W}$  and in late March near  $160^\circ\text{W}$ . The southernmost position between  $120^\circ\text{W}$  and  $150^\circ\text{W}$  occurs generally in mid-March when the ITCZ position ranges from less than  $6^\circ\text{N}$  near  $120^\circ\text{W}$ ,  $140^\circ\text{W}$ , and  $150^\circ\text{W}$  to slightly greater than  $7.5^\circ\text{N}$  near  $130^\circ\text{W}$ . A rapid northward movement of the ITCZ between  $110^\circ\text{W}$  and  $140^\circ\text{W}$  commences in late April, then slows down during July, finally culminating in August or early September. The most northerly ITCZ position across the eastern tropical Pacific Ocean, slightly less than  $15^\circ\text{N}$ , is reached within this zone near  $117^\circ\text{W}$  in late August. West of  $140^\circ\text{W}$ , the northward ITCZ movement is delayed somewhat, starting in May or June, and generally is not as pronounced as that for the longitude band  $110^\circ\text{W}$ - $140^\circ\text{W}$ . An August maximum north ITCZ position of about  $12^\circ\text{N}$  is observed between  $140^\circ\text{W}$  and  $161^\circ\text{W}$ . The southward movement of the ITCZ in October and November is quite rapid from  $110^\circ\text{W}$  to  $125^\circ\text{W}$ , but significantly slower westward from  $125^\circ\text{W}$ . As a consequence of this slow southward movement, the ITCZ between  $120^\circ\text{W}$  and  $160^\circ\text{W}$  remains further north into northern winter when compared with its position eastward from  $120^\circ\text{W}$ .

Although the seasonal variation in the standard deviation of the eastward from  $120^\circ\text{W}$ .

Although the seasonal variation in the standard deviation of the ITCZ latitudinal position (Fig. 12) is quite noisy, significant

qualitative conclusions can nonetheless be drawn. First, the standard deviation well away from the influence of the American coast is large. Second, the variability within this open ocean region appears in general to have a large annual signal, with the smallest standard deviations of the ITCZ position occurring during northern summer and the largest standard deviations during northern winter. Third, a bimodal structure is observed near the coast and reflects significant variability in the two south positions of the ITCZ depicted in Fig. 11. Fourth, a broad area of relatively low standard deviation is observed over the eastern Pacific coastal waters and in part reflects limitations in latitudinal movement imposed by land boundaries. Last, the maximum standard deviation located near  $117^{\circ}\text{W}$  in June is very large ( $> 3.5^{\circ}$  of latitude) and indicates significant year to year temporal differences in the ITCZ northward movement.

The conclusion that the ITCZ latitudinal position exhibits a significant annual signal is confirmed by harmonic analysis. Standard methods, as given by Jenkins and Watts (1968), are applied to each  $22^{\circ}$  band averaged ITCZ position time series given in Fig. 3. Results in Table 4 show that the annual harmonic accounts for a very large percentage of the total variance, being an overwhelming 76% for the  $99\text{-}121^{\circ}\text{W}$  longitude band. Compared to the annual harmonic, all other harmonics are seen to be quite insignificant.

Unlike the strong annual harmonic found for the ITCZ latitudinal position, harmonic analysis performed on the band averaged ITCZ intensity of convergence series of Fig. 4 indicates no dominant annual position, harmonic analysis performed on the band averaged ITCZ intensity of convergence series of Fig. 4 indicates no dominant annual signal, with the annual harmonic overall accounting for less than 10%



Table 4. Total variance as well as the frequencies and percentage of the total variance explained by the two largest harmonics calculated from each of the four 22° band averaged time series of the ITCZ latitudinal position given in Fig. 3. Units of variance are degrees squared; frequencies are year<sup>-1</sup>.

Longitude Band	Variance	Freq.	Harmonics		
			%	Freq.	%
139-161°W	7.2	1.00	54.6	0.28	3.0
119-141°W	10.3	1.00	60.6	1.94	1.5
99-121°W	12.9	1.00	76.2	3.00	1.4
79-101°W	3.9	1.00	63.5	2.00	5.0

of the total variance (see Table 5). Although the semiannual signal is found to be larger than the annual signal for the easternmost band (79-101°W) and the westernmost band (139-161°W), the percentage of the total variance explained by the semiannual signal is approximately 10% for either band. The sum of the two largest harmonics, the annual and the semiannual, accounts for only about 15-20% of the total variance. The distribution of the remaining 80-85% of the total variance at all other frequencies clearly indicates that the spectra of the ITCZ intensity of convergence is essentially white.

For discussion purposes, the map of the seasonal variability in the intensity of convergence of the ITCZ (Fig. 13) is divided into two bands, 79-110°W and 110-161°W. The easternmost of the two bands exhibits, upon first glance, a very confused pattern. Various centers of low and high intensity of convergence, ranging from  $< 4 \times 10^{-6} \text{ s}^{-1}$  at 86°W during September to  $> 1.4 \times 10^{-5} \text{ s}^{-1}$  at 90°W during August, are seen to be distributed in a quite random fashion. A closer inspection, however, reveals that a more organized pattern exists within the band throughout the year. This pattern consists of alternating longitudinal bands of high and low intensity of convergence. At the eastern boundary, corresponding to the American coast, a generally large ITCZ intensity of convergence is observed throughout the year. This high intensity of convergence is thought to be enhanced by topographical effects at and immediately inland from the coast. Westward from the coast, an axis of relatively low intensity of convergence is found. Its longitudinal position varies from about 87°W for March through coast, an axis of relatively low intensity of convergence is found. Its longitudinal position varies from about 87°W for March through October to about 91°W for the remainder of the year. Still further

Table 5. Total variance as well as the frequencies and percentage of the total variance explained by the two largest harmonics calculated from each of the four 22° band averaged time series of the ITCZ intensity of convergence given in Fig. 4. Units of variance are  $10^{-12} \text{ s}^{-2}$ ; frequencies are  $\text{year}^{-1}$ .

Longitude Band	Variance	Freq.	Harmonics		
			%	Freq.	%
139-161°W	2.8	2.00	10.1	1.00	7.4
119-141°W	6.7	1.00	11.1	2.00	6.2
99-121°W	8.8	1.00	12.3	2.00	8.8
79-101°W	10.6	2.00	8.6	1.00	6.3

west, a broader zone of high ITCZ intensity of convergence is observed. The approximate axis of this zone shows considerable longitudinal extent, being at  $90^{\circ}\text{W}$  in August and around  $100^{\circ}\text{W}$  in January.

A relation between ITCZ intensity of convergence and observed low level cloudiness offers a possible explanation for the observed longitudinal variability of ITCZ intensity of convergence eastward from  $110^{\circ}\text{W}$ . Satellite cloud photos show that convective cloudiness associated with the ITCZ is usually made up of a number of distinct cloud clusters, separated by regions of relatively clear skies. Chang (1970) presented evidence that ITCZ cloud clusters, with usual low level convergence of the order of  $10^{-5} \text{ s}^{-1}$ , are actually precipitation areas associated with westward-propagating weak wave disturbances along the ITCZ. The clearer areas between cloud clusters are marked by weak divergence and subsidence. Obviously, longitudinal differences in ITCZ intensity of convergence within a certain region would tend to disappear in the long-term mean if the westward-propagating ITCZ cloud clusters are steady-state. Thus, any relationship drawn between the observed alternating bands of high and low intensity of convergence east of  $110^{\circ}\text{W}$  and cloud clusters presupposes that the cloud clusters are not steady state, but, rather in the long-term mean have preferred longitudes in regards to formation, strength, and frequency of occurrence.

Satellite cloud analysis studies by Sadler et al. (1976) and Chang (1970) indicate persistent heavy convective cloudiness throughout the year over Colombia and immediate coastal waters at the latitude of the ITCZ. Chang (1970) indicate persistent heavy convective cloudiness throughout the year over Colombia and immediate coastal waters at the latitude of the ITCZ. This relates well with the observed high ITCZ intensity of

convergence found at the Colombian coast. Total cloudiness westward from the coast, as given by Sadler et al., does not, however, generally relate well with the band of minimum ITCZ intensity of convergence from 87-91°W nor with the band of maximum convergence from 90-100°W. This lack of a definite relation between cloudiness and ITCZ intensity of convergence is not surprising in light of the significant differences in data length, coverage, and resolution which exist between the two parameters. Nonetheless, in spite of such inconsistencies, some monthly mean total cloudiness maps of Sadler et al. do show a coastal maximum, a near coast minimum, and a more western maximum over the longitude zone from the coasts of Colombia and Panama westward to 100°W, a pattern similar to that of the ITCZ intensity of convergence.

In addition to total cloudiness, two other features of the ocean-atmosphere system were examined in connection with the longitudinal variability of the ITCZ intensity of convergence. The relationship between the mean atmospheric circulation over the eastern tropical Pacific Ocean and the ITCZ intensity of convergence proved to be inconclusive. The idea that cold sea surface temperatures, which would inhibit convection and reduce convergence, are responsible for the minimum ITCZ intensity of convergence band from 87-91°W, was found to counter existing evidence. Warm sea surface temperatures are observed throughout the year within the ITCZ across the extreme eastern tropical Pacific Ocean. Furthermore, the northward movement of colder Peruvian Current water, which occurs most noticeably during austral winter, does not reach the latitude of the ITCZ. Current water, which occurs most noticeably during austral winter, does not reach the latitude of the ITCZ.

The seasonal variability of the ITCZ intensity of convergence west of  $110^{\circ}\text{W}$  is highlighted by a prominent tongue of high convergence extending westward during northern summer and fall from maxima located between  $90^{\circ}\text{W}$  and  $100^{\circ}\text{W}$ . ITCZ intensity of convergence values  $> 8 \times 10^{-6} \text{ s}^{-1}$  are observed in a broad elongated zone from  $120^{\circ}\text{W}$  to  $150^{\circ}\text{W}$  during August and September. Elsewhere west of  $110^{\circ}\text{W}$ , ITCZ convergence values are generally in the range  $4$  to  $6 \times 10^{-6} \text{ s}^{-1}$  throughout the remainder of the year. This pattern of variability suggests that a strong seasonal cycle occurs west of  $110^{\circ}\text{W}$ . This cycle is not a simple annual cosine wave since large convergences occur only in a few months and during the remainder of the year the values are fairly constant.

The seasonal variability in the standard deviation of the ITCZ intensity of convergence (Fig. 14) reflects the same general features as those depicted in the map of the seasonal variation of the ITCZ intensity of convergence. In general, areas with large ITCZ convergence values exhibit large standard deviations; areas of low ITCZ intensity of convergence, low standard deviations. The hatched area of Fig. 14, representing standard deviations greater than  $4 \times 10^{-6} \text{ s}^{-1}$ , is observed to be widest at the eastern boundary and narrower further west. Between  $100^{\circ}\text{W}$  and  $135^{\circ}\text{W}$ , standard deviations of the ITCZ intensity of convergence greater than  $4 \times 10^{-6} \text{ s}^{-1}$  only encompass the months from June to September. A majority of the area west of  $120^{\circ}\text{W}$  has relatively low standard deviations of less than  $3 \times 10^{-6} \text{ s}^{-1}$ . The isolated minimum at  $85^{\circ}\text{W}$  at the end of September reflects the similarly located minimum in the ITCZ intensity of convergence field. Finally, isolated minimum at  $85^{\circ}\text{W}$  at the end of September reflects the similarly located minimum in the ITCZ intensity of convergence field. Finally, the very fact that substantial parts of the standard deviation field

depicted in Fig. 14 have values greater than half of the corresponding ITCZ intensity of convergence values of Fig. 13 attest to the very high variability and noisiness of the convergence data.

## 5. INTERANNUAL VARIABILITY OF THE ITCZ

The interannual variability of the ITCZ latitudinal position and intensity of convergence is depicted in Figs. 15 and 16, respectively. These plots are obtained by applying a 12-month running mean to the ITCZ latitudinal position and intensity of convergence time series given in Figs. 3 and 4. Since the application of the asymmetric 12-month running mean filter to these time series introduces a slight phase shift, a certain degree of caution should be exercised in interpreting the interannual records.

The interannual variability of the ITCZ latitudinal position is complex and aperiodic. Variability is observed to be small for the easternmost band 79-101°W and greater westward, with the westernmost bands centered at 130°W and 150°W exhibiting a few peak-to-trough variations of 2-2.5° of latitude. No significant phase relationship is noted among the four ITCZ position time series depicted in Fig. 15.

A visual comparison of the plots of Fig. 3 and Fig. 15 reveals that the seasonal variability of the ITCZ latitudinal position across the eastern tropical Pacific is much larger than the interannual variability. The largest peak-to-trough interannual variability, of the order of 2.5° of latitude within the two western bands 119-141°W and 139-161°W, is seen to be far outshadowed even by the smallest seasonal variability across the region, that being a usual 6-7° of latitude for the band 79-101°W. The dominance of the annual signal seasonal variability across the region, that being a usual 6-7° of latitude for the band 79-101°W. The dominance of the annual signal



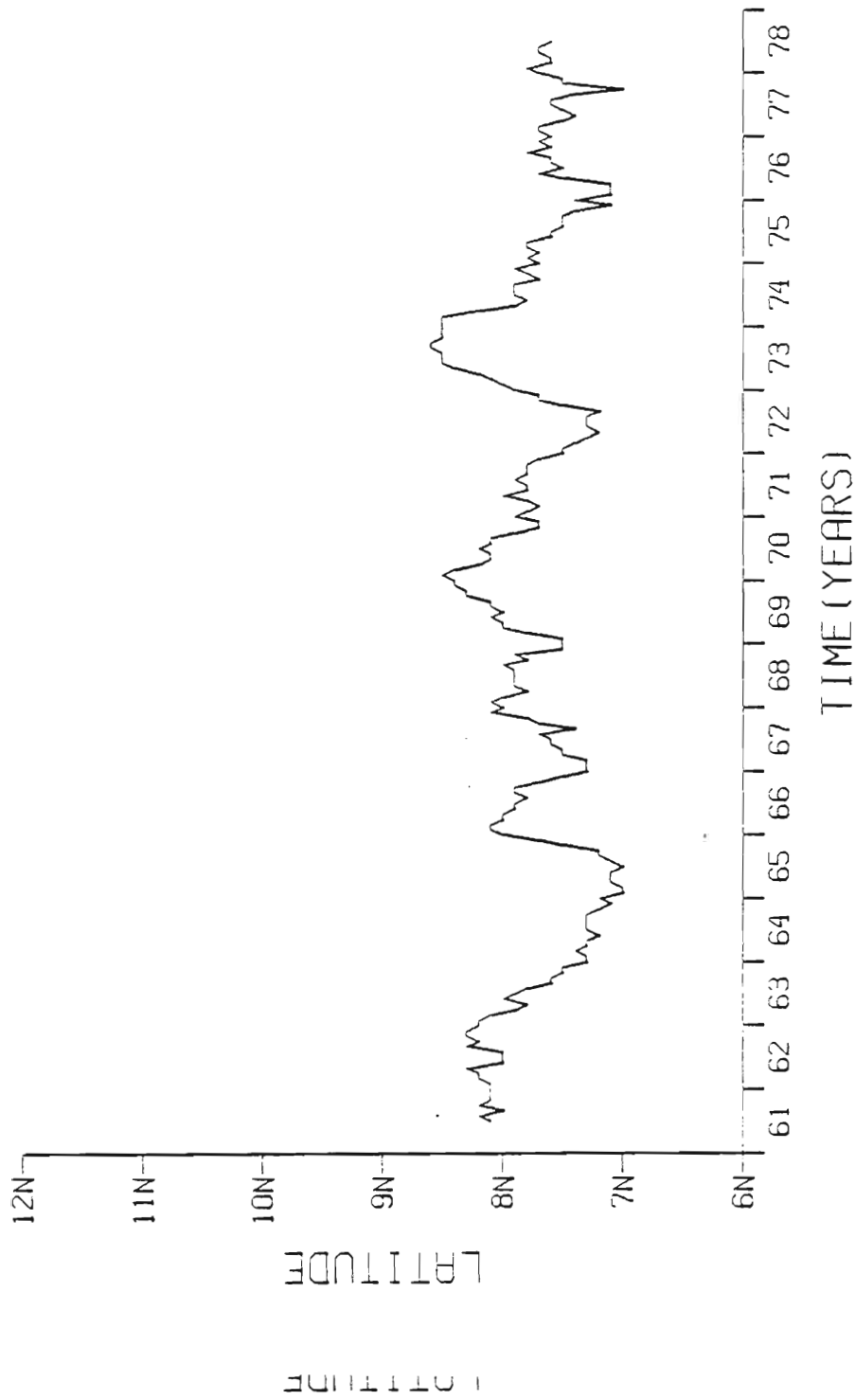


Fig. 15. (a) ITCZ latitudinal position, band averaged across 22° of longitude from 79°W to 101°W and centered at 90°W, filtered with a twelve month running mean.

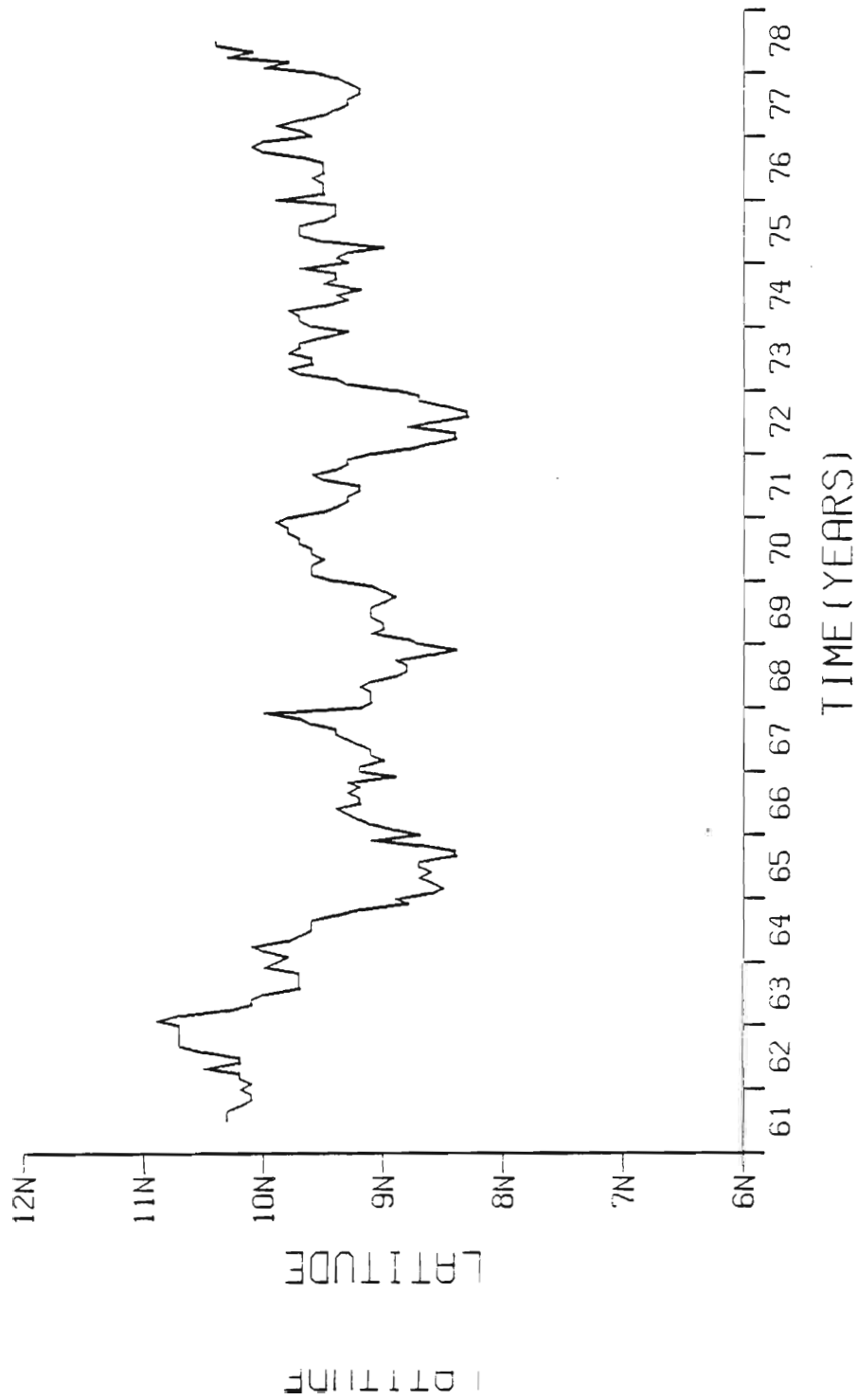


Fig. 15. (b) Similar to (a) but for band 99°W to 121°W and centered at 110°W.

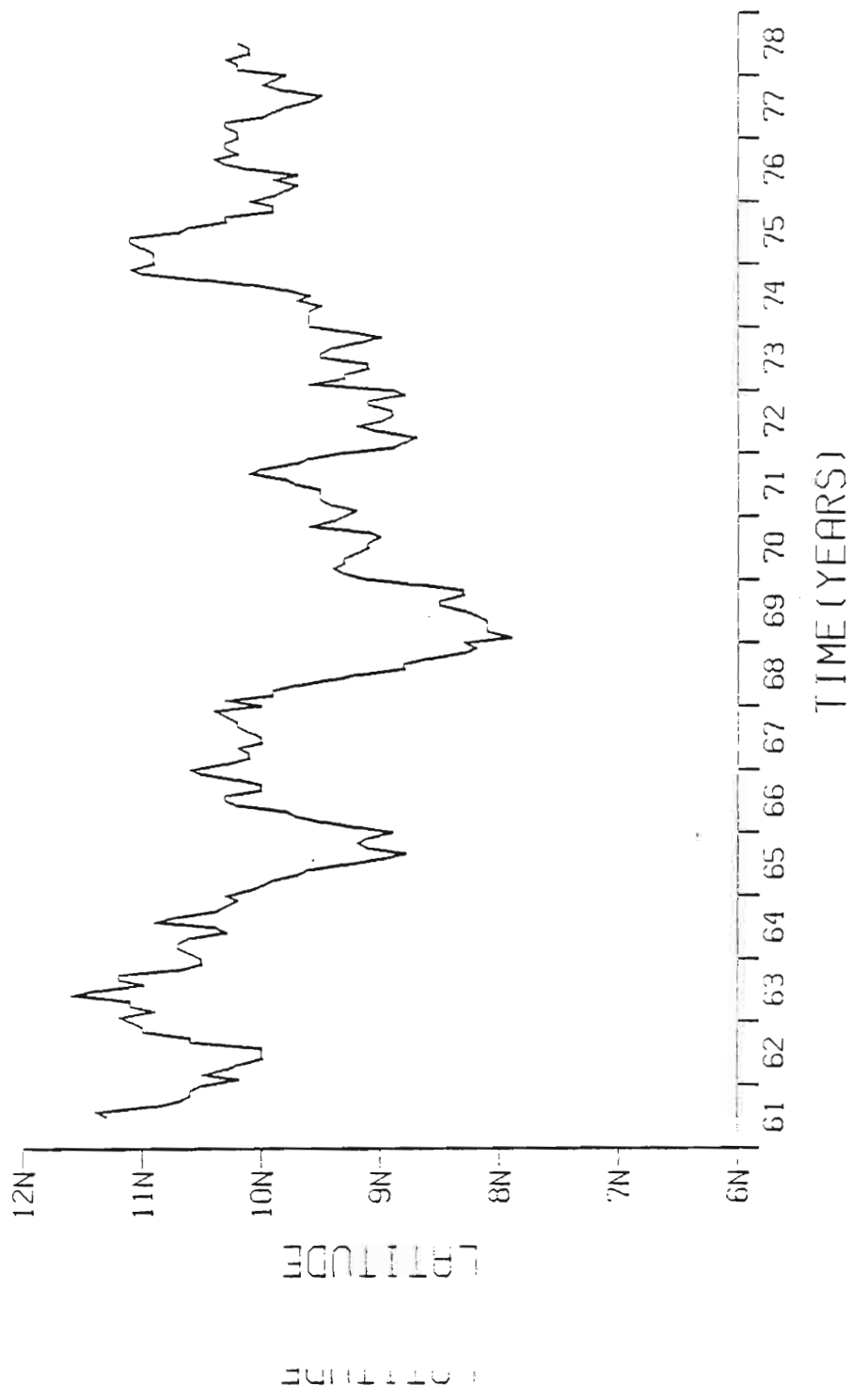


Fig. 15. (c) Similar to (a) but for band 119°W to 141°W and centered at 130°W.

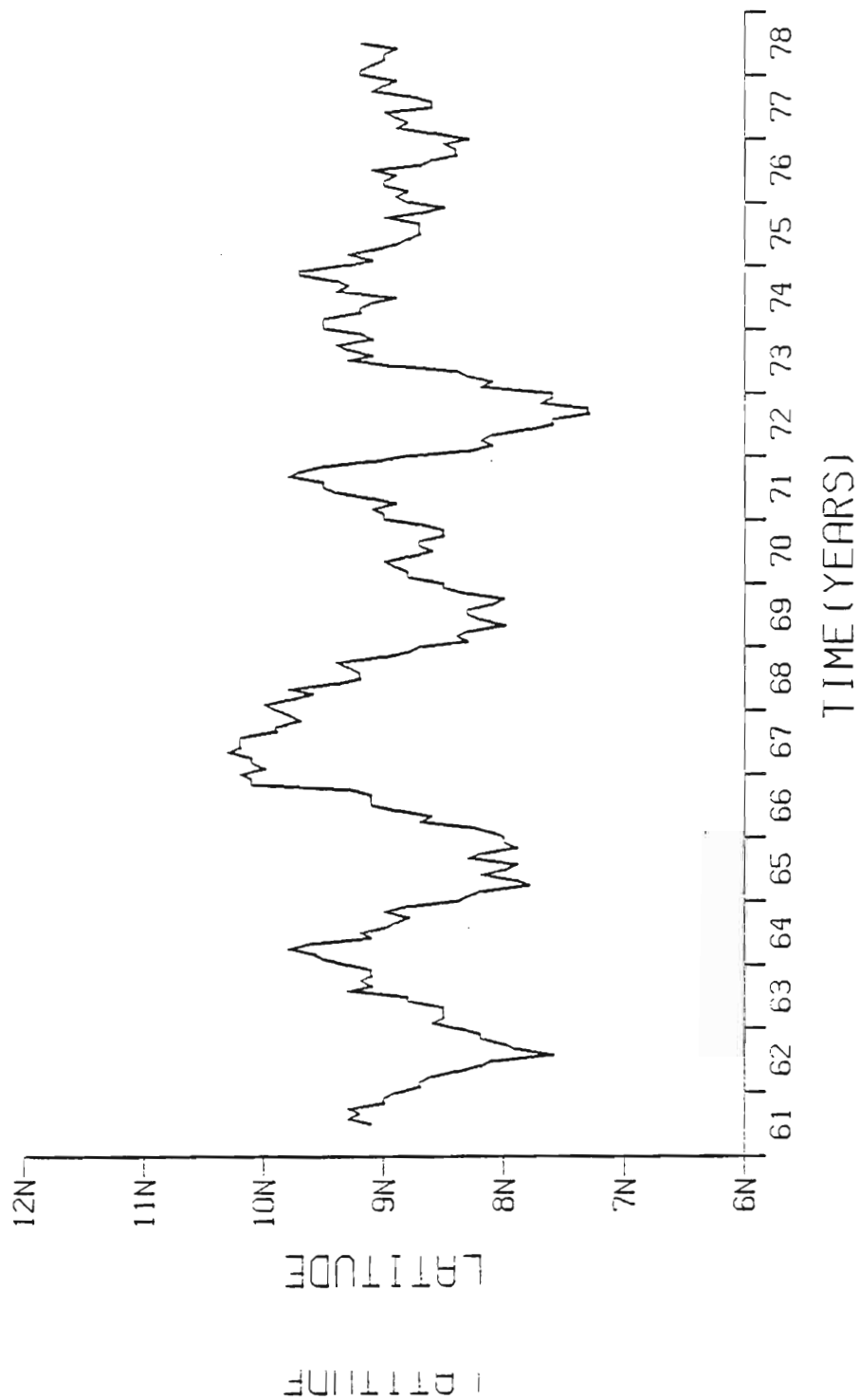


Fig. 15. (d) Similar to (a) but for band 139°W to 161°W and centered at 150°W.

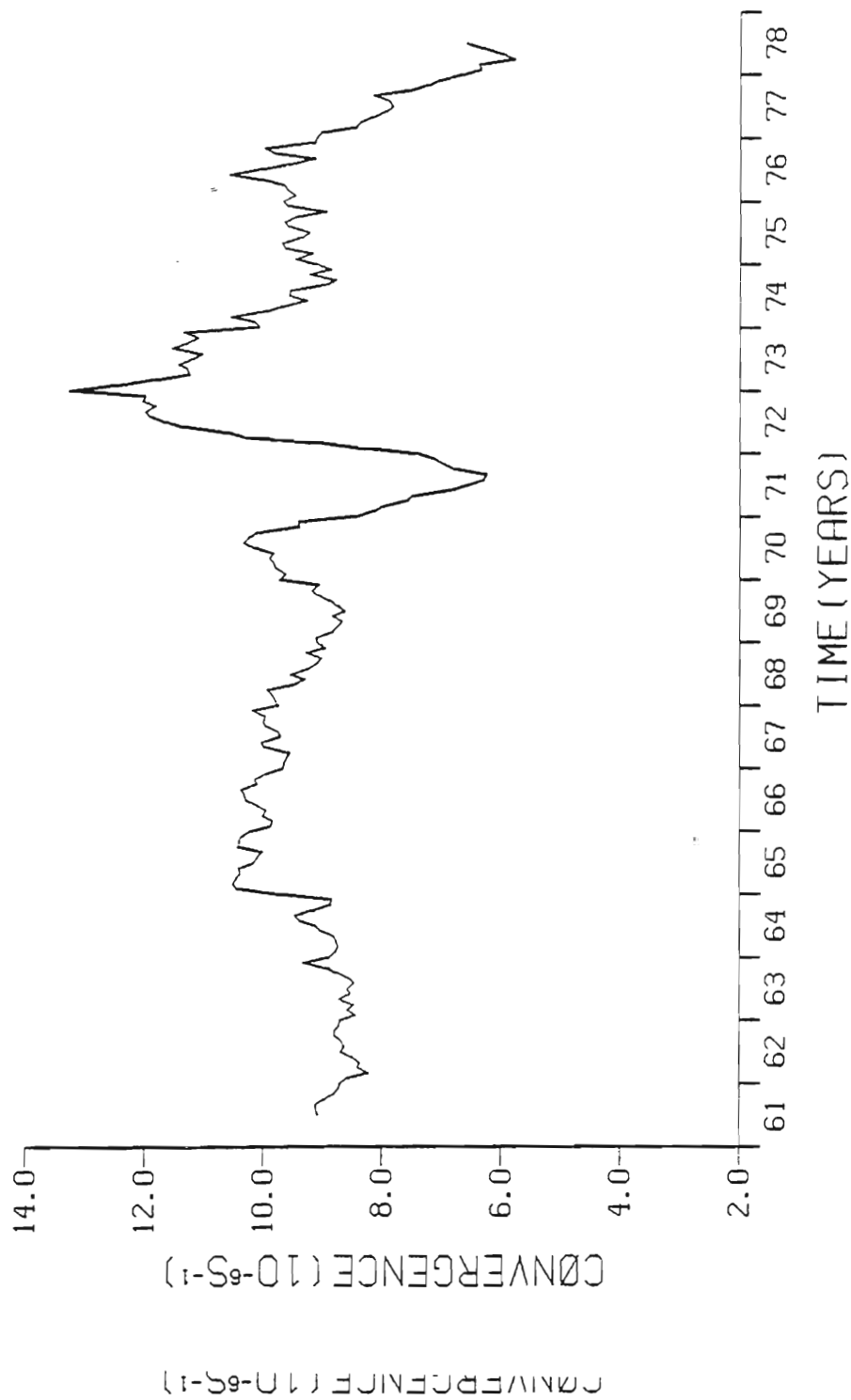


Fig. 16. (a) ITCZ intensity of convergence, band averaged across 22° of longitude from 79°W to 101°W and centered at 90°W, filtered with a twelve month running mean.

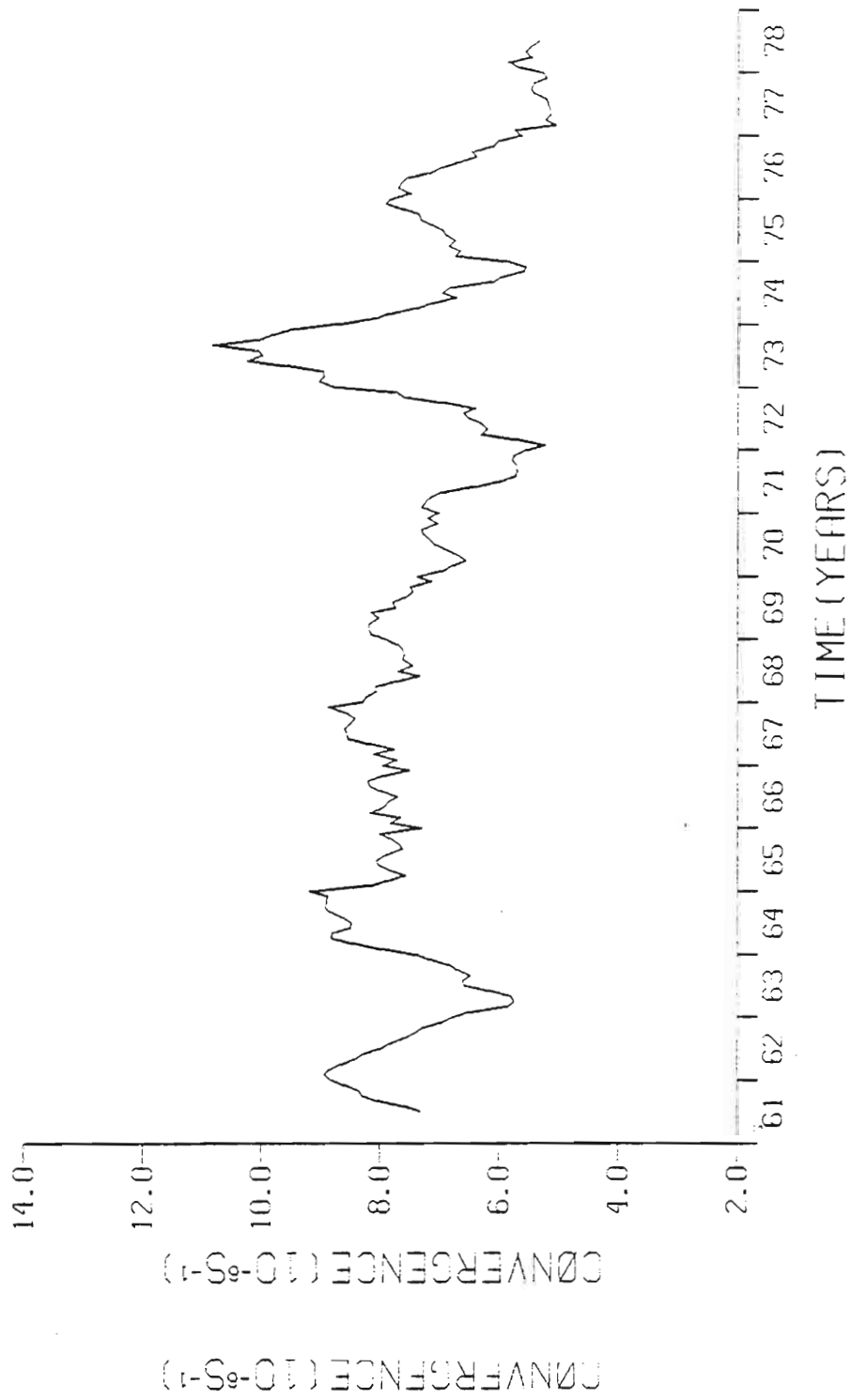


Fig. 16. (b) Similar to (a) but for band 99°W to 121°W and centered at 110°W.

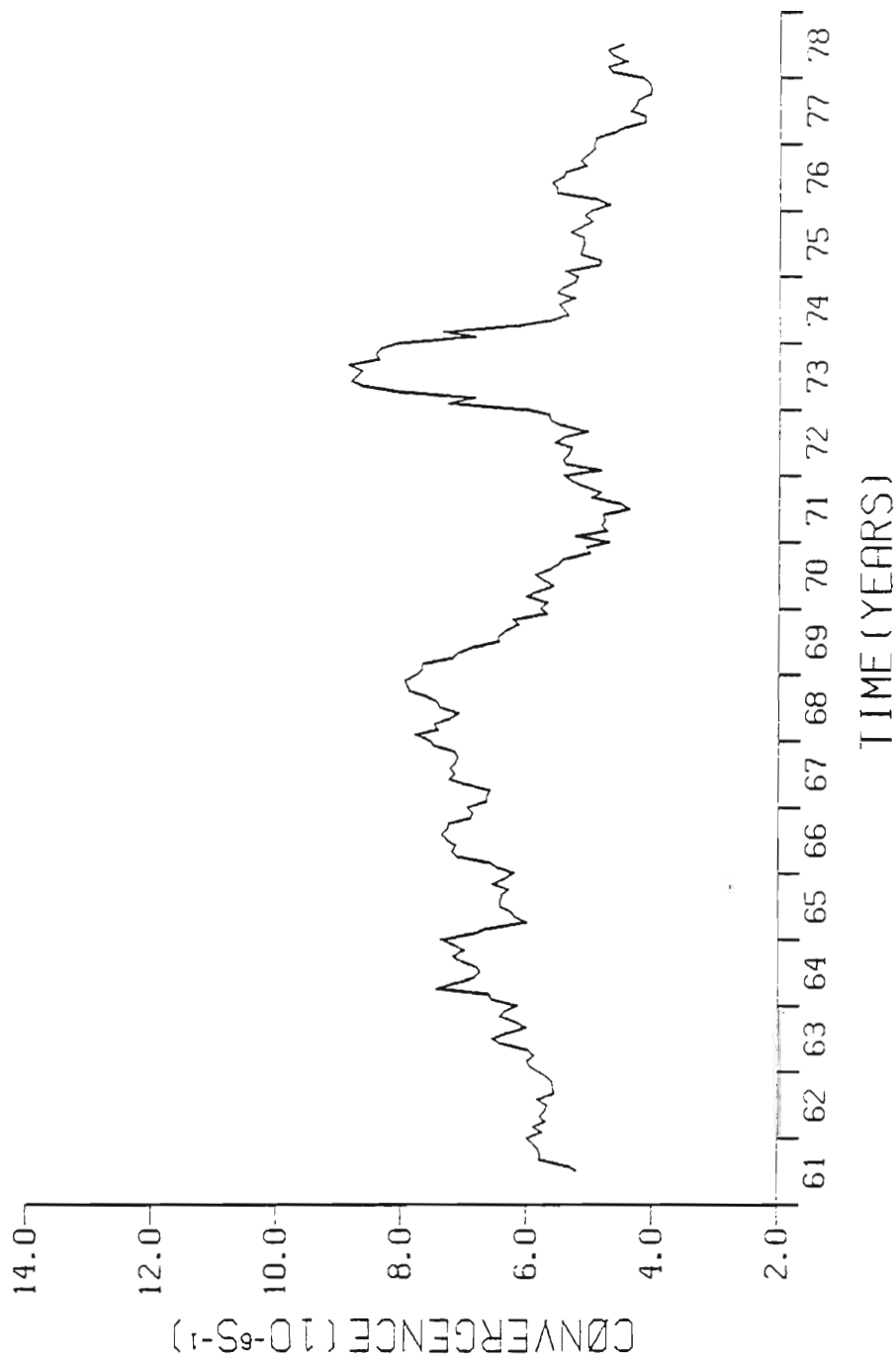


Fig. 16. (c) Similar to (a) but for band 119°W to 141°W and centered at 130°W.

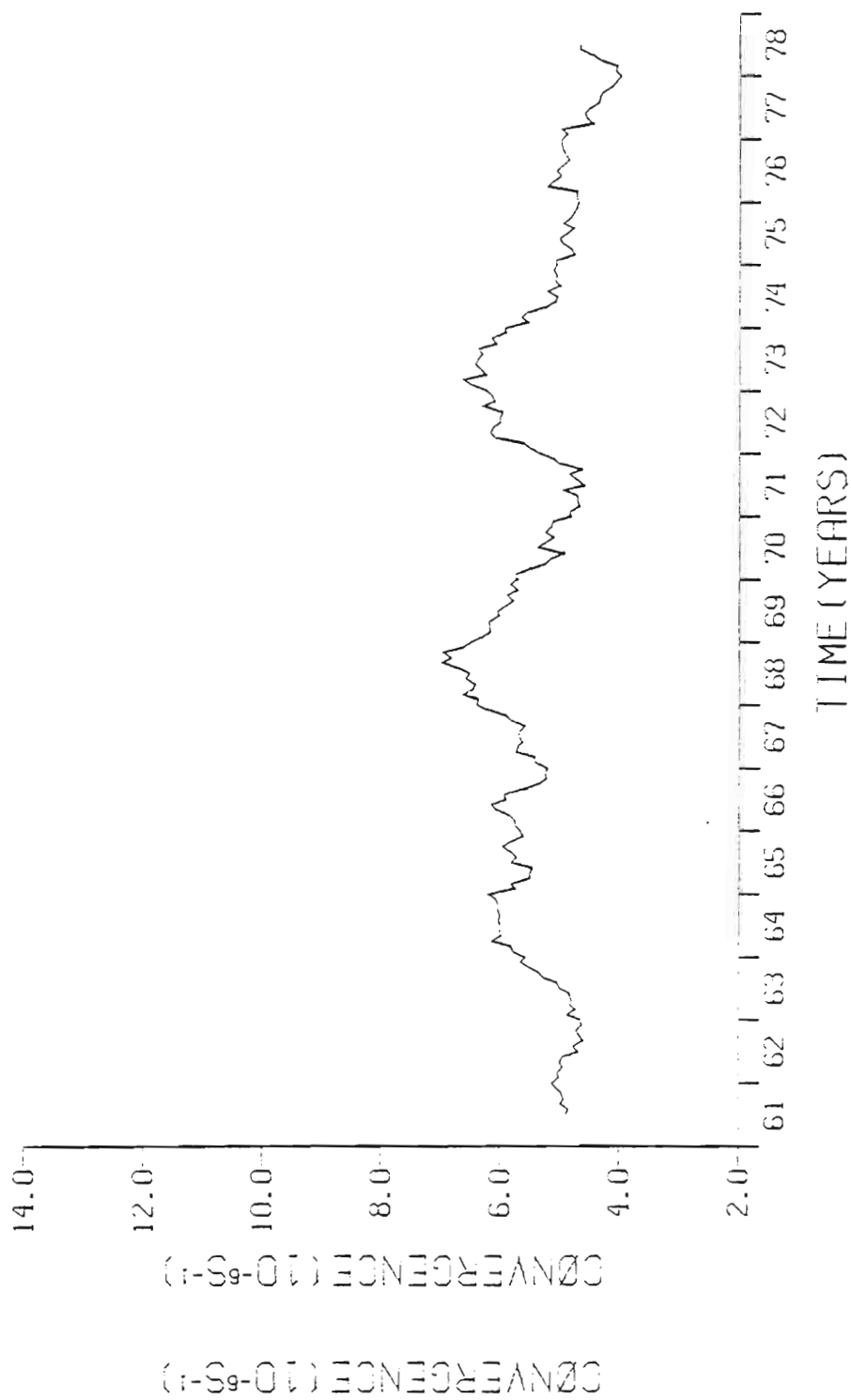


Fig. 16. (d) Similar to (a) but for band 139°W to 161°W and centered at 150°W.



over the interannual is confirmed in Table 4 which indicates that only in the band 139-161°W is an interannual harmonic second in importance to the annual harmonic, and there of only minor significance, explaining but 3% of the total variance.

A significant feature of the interannual variability of the ITCZ intensity of convergence is its overall small variation. Indeed, for the westernmost band 139-161°W, the interannual signal during the 1961-78 period remains between  $4 \times 10^{-6} \text{ s}^{-1}$  and  $7 \times 10^{-6} \text{ s}^{-1}$ . The three longitude bands east of 140°W are dominated by a pronounced peak in the intensity of convergence during the 1972-73 period. A distinct phase relationship is not found among the four intensity of convergence time series of Fig. 15.

Significant interannual changes in the ITCZ position and intensity of convergence have been reported in association with El Niño events in the equatorial Pacific Ocean. Nowadays, in a general sense, El Niño refers to an aperiodic episode of anomalously warm sea surface temperatures in the eastern and central equatorial Pacific Ocean, which typically persists for one to two years. Ramage (1975) determined that during the intense 1972-73 El Niño the Northern Hemisphere near-equatorial convergence zone shifted about 3° closer to the equator over the central equatorial Pacific. Reiter (1978) showed that the trades flow stronger-than-normal toward the equator during El Niño events and result in an intensification of the ITCZ which reflects itself in enhanced precipitation over the equatorial Pacific Ocean. Donguy and Henin (1980), based on wind derived positions of the ITCZ itself in enhanced precipitation over the equatorial Pacific Ocean. Donguy and Henin (1980), based on wind derived positions of the ITCZ along 90°W during the El Niño years 1972 and 1976, stated that during

El Niño years the ITCZ is south of its usual location over the eastern tropical Pacific. A statistical study by Egger et al. (1981) indicated a southward shift of the ITCZ over the eastern and central Pacific Ocean during periods of low Southern Oscillation Index (viz., during El Niño events). Rasmusson and Carpenter (1982) composited surface wind and sea surface temperature fields of six El Niño events into a "typical" sequence. Their results showed enhanced low-level convergence and anomalously strong equatorward flow across the normal position of the ITCZ in the eastern and central equatorial Pacific. They further identified the southward shift of the ITCZ during an El Niño event as a critical kinematic feature associated with central Pacific precipitation anomalies. Pazan and Meyers (1982) computed surface wind and divergence maps for cold and warm ocean equator conditions (the warm corresponding to El Niño events) which showed that the ITCZ is 2-4° closer to the equator during warm equator conditions. Finally, Liebmann and Hartmann (1982), in a study encompassing the 1976 El Niño event, reported an enhanced ITCZ from March 1976 to March 1977 over the eastern and central tropical Pacific Ocean and deduced that it was not merely a southward shift of the ITCZ which caused this enhancement.

The 18-year data record of this study provides a good basis to verify the relationship between El Niño events and ITCZ behavior, in particular the reported southward shift and intensification of the ITCZ during El Niño events. During the 1961-78 period, five El Niño events and one aborted El Niño event occurred. The great 1972 El Niño was the most intense; the 1963 El Niño and the 1975 aborted El Niño were the and one aborted El Niño event occurred. The great 1972 El Niño was the most intense; the 1963 El Niño and the 1975 aborted El Niño were the weakest. The 1965 and 1976 El Niño events can be classified as moderate; the 1969 El Niño as minor.

Careful inspection of the interannual plots of the ITCZ latitudinal position depicted in Fig. 15 indicates that in only two El Niño years, 1965 and 1972, a distinct south position of the ITCZ occurs in all four longitude bands. During 1969, pronounced south positions are noted for the bands centered at  $130^{\circ}\text{W}$  and  $150^{\circ}\text{W}$  while the eastern bands centered at  $90^{\circ}\text{W}$  and  $110^{\circ}\text{W}$  exhibit only brief and slight southward ITCZ shifts from late 1968 to very early 1969.

A distinct relation between a southward shift of the ITCZ and El Niño is not found for the moderate 1976 El Niño event nor for the very minor events of 1963 and 1975. Such a conclusion is exemplified by a study of the period from late 1975 to early 1977 which encompasses the 1976 El Niño event. Although this El Niño was of moderate intensity, in only one longitude band is the ITCZ position during 1976 more than  $1^{\circ}$  of latitude south of the most northerly position during 1975. In addition to a rather insignificant southward shift, considerable time variation in south positions is noted among the four longitude bands with the two westernmost bands, centered at  $130^{\circ}\text{W}$  and  $150^{\circ}\text{W}$ , exhibiting an almost complete out-of-phase ITCZ positional relationship from late 1975 to early 1977.

A further inspection of the interannual ITCZ latitudinal position plots shows that during several El Niño events, most especially the stronger ones, a double or even triple south ITCZ position occurs. This is thought to result from a modulation of the interannual signal by the much stronger seasonal ITCZ cycle. A similar idea was expressed by Ramage and Hori (1981) who, in a study of the 1972-73 El Niño event, emphasized the role of the annual cycle in the atmospheric circulation over the eastern Pacific in modulating the strength of the

El Niño signal, concluding that the annual cycle reinforced El Niño between September and April and weakened El Niño between April and September.

In general, the relationship between an enhanced ITCZ intensity of convergence and El Niño is not confirmed by the interannual variability plots of the ITCZ intensity of convergence depicted in Fig. 16. In these plots, a very pronounced convergence peak is observed to occur during mid-1973 for the longitude bands centered at  $90^{\circ}\text{W}$  and  $110^{\circ}\text{W}$ . This relates poorly with the Ramage and Hori (1981) result that the great 1972-73 El Niño had disappeared by April 1973. The peak in convergence near the end of 1972 for the easternmost band  $79-101^{\circ}\text{W}$  does, however, agree well with the December '72-January '73 maximum El Niño intensity of Ramage and Hori. The enhanced ITCZ reported by Liebmann and Hartmann (1982) during the 1976 El Niño event is essentially absent from the interannual ITCZ intensity of convergence plots of Fig. 16. In addition, these plots indicate no distinct relationship between ITCZ intensity of convergence and El Niño for the remaining four El Niño events within the 1961-78 period.

More than anything else, the interannual variability of the ITCZ latitudinal position and intensity of convergence demonstrates its own spatial and temporal complexity. The idea that an El Niño event in the eastern equatorial Pacific is associated with a southerly displaced and strengthened ITCZ is not substantiated by the results of this study which instead suggest that these features can be related only to some El Niño events. Finally, the appearance of marked southward displacements of the ITCZ for some longitude bands during 1962 and 1977

suggest that in addition to the El Niño other phenomena, most likely of a global scale, play an important role in the interannual variability of the ITCZ over the eastern tropical Pacific Ocean.

## 6. SECONDARY CONVERGENCE ZONES

The existence of secondary convergence zones or even a double ITCZ over the eastern tropical Pacific Ocean has been a topic of interest for many years. Fletcher (1945), based on surface, upper air, and aircraft observations, proposed that there are two intertropical convergence zones, the principal one being located in the summer hemisphere and a secondary one being located near the equator or in the winter hemisphere. Simpson (1947) found nominal evidence that two convergence zones are sometimes present during northern summer and fall. Alpert (1945) stated that secondary convergence zones are often present which may have heavier clouds and weather than that of the intertropical convergence zone.

It is widely believed that cloud bands are to be expected in zones of convergence; indeed, the term "ITCZ" has oftentimes been defined in terms of cloudiness. Kornfield et al. (1967) presented cloud mosaics showing the distribution of clouds for typical half month periods. A mosaic for March 1967 dramatically showed a pair of cloud bands on either side of the equator over the eastern tropical Pacific Ocean. The cloud band south of the equator varied greatly in intensity and was practically non-existent in the January and June 1967 mosaics. The northern band, that associated with the ITCZ, was observed to be relatively stationary and more persistent. This double cloud-maximum structure is also evident eastward from about 140°W in the mean March relatively stationary and more persistent. This double cloud-maximum structure is also evident eastward from about 140°W in the mean March and April charts of the 1965-73 cloud climatology atlas by Sadler et al. (1976).

An exact cause for the seasonally observed cloud band south of the equator is not known. Hubert et al. (1969) indicated that the "southern ITCZ" in late northern winter or spring occurs when the trade winds weaken and sea surface temperatures in the region reach a maximum. This is substantiated by Donguy and Henin (1980) who, based on ship observations, hypothesize the existence of a southern convergence zone associated with extensive cloudiness between 1°S and 5°S.

Wyrтки and Meyers (1975) calculated annual and bimonthly surface wind divergence maps from ship observations for the Pacific Ocean and found a near-equatorial convergence to exist just south of the equator in the eastern tropical Pacific Ocean. Its location is observed to be nearly the same throughout the year except in November-December, when it does not appear. The intensity of this convergence is greatest in March-April with a maximum convergence greater than  $4 \times 10^{-6} \text{ s}^{-1}$  centered at 5°S, 100°W. Moreover, during this bimonthly period, Wyrтки and Meyers show the southern and northern near-equatorial convergence zones to be connected across the equator between 135°W and 145°W.

The convergence zone in the eastern tropical Pacific just south of the equator found by Wyrтки and Meyers is nonexistent in the annual and seasonal divergence maps of this study (Figs. 7 and 10). On the contrary, a zone of large divergence is seen to occupy its location. Such a significant difference is surprising in light of the fact that the data base, the N-S grid spacing, and the finite difference method used for both studies are quite similar. the data base, the N-S grid spacing, and the finite difference method used for both studies are quite similar.

As previously mentioned, the only distinct secondary convergence zone which appears in the surface wind divergence maps (Figs. 7 and 10) is the DJF southern near-equatorial zone with axis along  $8^{\circ}\text{S}$  west of  $145^{\circ}\text{W}$ . This convergence axis results from both speed and directional convergence as trade winds off the western side of the SE Pacific subtropical high turn sharply E to NE and slow down as they proceed toward the SPCZ. Available cloud cover and rainfall climatology, as given by Sadler et al. (1976) and Dorman and Bourke (1979), respectively, indicate that this derived austral summer convergence axis is located in a region of strong cloud cover and rainfall gradients between the equatorial dry zone and the SPCZ.

Convergence within the northern near-equatorial convergence zone (see Figs. 7 and 10) is primarily associated with the ITCZ although in some seasons other mechanisms, such as speed convergence within the NE trade winds, contribute appreciably to the convergence within certain parts of the zone. Ideally, it would be desirable to separate clearly the convergence associated with the ITCZ from that due to other mechanisms. In reality, however, this is not possible. The space and time scales of this study, in conjunction with the ITCZ analysis scheme, are all geared to produce a climatological mean state and not a detailed small-scale analysis. Any discussion, then, of the northern near-equatorial convergence zone will have to consider the zone as a single convergence entity containing several operative mechanisms.

The near-equatorial convergence zones can be further studied by use of Fig. 17. This map gives the percent of time that a convergence

The near-equatorial convergence zones can be further studied by use of Fig. 17. This map gives the percent of time that a convergence maximum along a given meridian from  $12^{\circ}\text{S}$  to  $24^{\circ}\text{N}$  corresponds to at



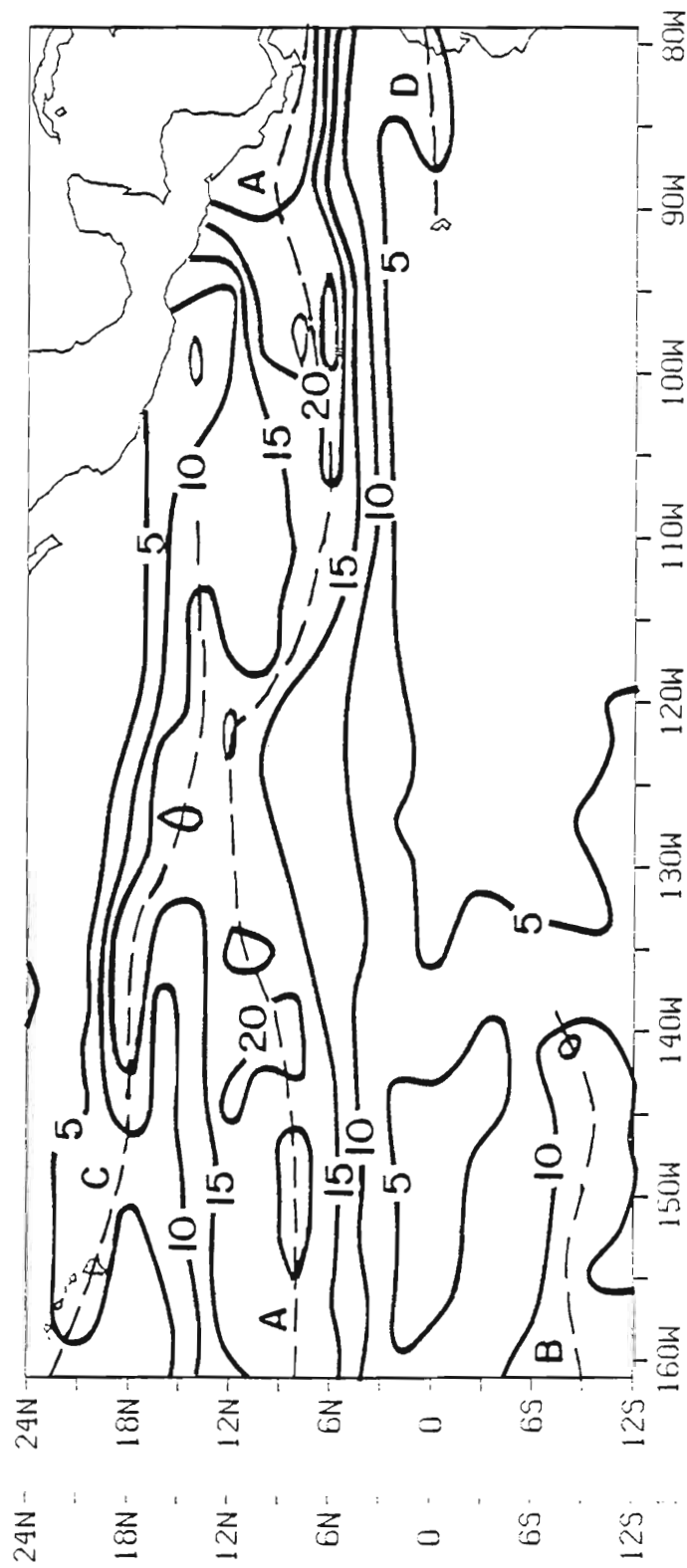


Fig. 17. Annual mean percent of time that a convergence maximum along a given meridian from 12°S to 24°N corresponds to at least 50% of the absolute maximum convergence along that same meridian. Approximate axes of high percentage, given as labelled dashed lines, are discussed in text.

least 50% of the absolute maximum convergence along that same meridian. It is constructed in such a way as to allow a concurrent examination of maximum and significant secondary convergences, the latter assumed to be those relative convergence maximums with intensities at least 50% of the absolute maximum. In Fig. 17, axis A and B correspond to the ITCZ and southern near-equatorial convergence zone, respectively. Annually, for longitudes west of  $140^{\circ}\text{W}$ , a substantially higher occurrence of convergence maximums is observed along the ITCZ than in conjunction with the southern near-equatorial convergence zone. Earlier in this paper, it was shown that the convergence associated with the southern near-equatorial convergence zone west of  $145^{\circ}\text{W}$  during DJF was of similar intensity to that of the ITCZ for a similar longitudinal domain. A map similar to Fig. 17 but for DJF (not presented in this report) confirms this finding. It indicates that during DJF, for longitudes west of  $145^{\circ}\text{W}$ , the occurrence of convergence maxima along the southern near-equatorial convergence axis rivals that associated with the ITCZ.

Elsewhere, a sharply defined axis of high convergence (C) is seen to extend from about  $110^{\circ}\text{W}$  to Hawaii. This axis is quite significant and is associated with speed convergence within the NE trade winds and a mean northern summer tropical storm path across the eastern tropical Pacific Ocean. The short axis extending along the equator from the coast of South America toward the Galapagos Islands (D) in part reflects a southerly displaced ITCZ during El Niño events.

reflects a southerly displaced ITCZ during El Niño events.

## 7. SUMMARY AND CONCLUSIONS

A subjectively analyzed data set consisting of monthly wind stress averages on a  $2^\circ$  square grid over the tropical Pacific Ocean for the period 1961-78 is used to construct annual and seasonal climatological fields of surface wind vectors and the divergence of the surface wind for the eastern tropical Pacific Ocean. A rather complex procedure is developed to calculate independently the ITCZ as a best fit to the axis of maximum convergence within the Northern Hemisphere near-equatorial convergence zone from filtered monthly surface wind divergence fields. Synthesis of all 216 individual monthly ITCZ calculations for the period 1961-78 results in a quasi-Lagrangian climatology of the ITCZ over the eastern tropical Pacific Ocean.

The northeast and southeast trade winds are the dominant features of the atmospheric surface circulation over the eastern tropical Pacific Ocean. In a long-term mean, both trade wind systems are of comparable strength but the SE trades are more extensive. Seasonal wind vector maps indicate that the large-scale circulation patterns of DJF and MAM are similar as well as those of JJA and SON, with either trade wind regime more extensive and stronger during the winter and spring of the respective hemisphere. During JJA and SON, strong cross-equatorial monsoon flow occurs east of  $120^\circ\text{W}$ .

An outstanding feature of the annual and seasonal surface wind divergence maps is the Northern Hemisphere near-equatorial convergence

An outstanding feature of the annual and seasonal surface wind divergence maps is the Northern Hemisphere near-equatorial convergence zone. Convergence within this zone is primarily associated with the

ITCZ although speed convergence within the NE trades throughout the year and convergence associated with a mean tropical storm track during northern summer contribute significantly. For all seasons, the most intense convergence within the zone occurs east of  $100^{\circ}\text{W}$ . A significant SON convergence maximum within the zone is centered near  $12^{\circ}\text{N}$ ,  $140^{\circ}\text{W}$ . A strong northward (southward) shift of the Northern Hemisphere near-equatorial zone occurs during JJA (DJF). Strong areas of divergence found throughout the year over the eastern Pacific Ocean west of Mexico and westward from the NW South American coast are observed to shift in association with the seasonal movements of the Northern Hemisphere near-equatorial convergence zone. During DJF, a southern near-equatorial convergence axis appears along  $8^{\circ}\text{S}$  west of  $145^{\circ}\text{W}$  in association with a sharp E to NE turning and slowing down of the SE trade winds.

In general, the climatology of the ITCZ latitudinal position exhibits a pronounced annual cycle, large standard deviations, and considerable longitudinal dependence. The annual mean latitude of the ITCZ across the tropical Pacific Ocean east of  $160^{\circ}\text{W}$  is slightly less than  $9^{\circ}\text{N}$ . Between  $90^{\circ}\text{W}$  and  $160^{\circ}\text{W}$ , the most southerly ITCZ position generally occurs in February-March and the most northerly position during August-September. East of  $90^{\circ}\text{W}$ , a bimodal structure is observed with two distinct south positions, one in February and another during September-October. A southward shift of the ITCZ occurs east of  $110^{\circ}\text{W}$  during July due to a temporary westward extension of a ridge from the Bermuda High into the western Caribbean Sea. The ITCZ latitudinal position during July due to a temporary westward extension of a ridge from the Bermuda High into the western Caribbean Sea. The ITCZ latitudinal position is generally found not to be synonymous with the near-equatorial axis of wind confluence.

Harmonic analysis of band averaged time series across the eastern tropical Pacific Ocean indicate that the spectra of the ITCZ intensity of convergence is essentially white. A pattern consisting of alternating bands of high and low ITCZ intensity of convergence is observed over the extreme eastern Pacific throughout the year. A tongue of high intensity of convergence extends westward from the extreme east tropical Pacific during the period July to November. Large standard deviations of the ITCZ intensity of convergence are associated with high intensity of convergence values, and vice versa.

Interannual variability of the ITCZ latitudinal position and intensity of convergence is much less than the seasonal ITCZ variability. The widely held notion that the ITCZ strengthens and shifts southward over the eastern tropical Pacific Ocean during El Niño events is not confirmed by the results of this study which instead indicate that these features are related to only some El Niño events. The complex and aperiodic variability of the interannual ITCZ records strongly suggests that other phenomena besides El Niño play important roles in the climatology of the eastern tropical Pacific Ocean.

A data record of 18 years is short for a climatological study. Despite data and analysis limitations, it is hoped that the quasi-Lagrangian ITCZ climatology presented in this report will provide a good observational basis for those investigators who seek a link between the behavior of the ITCZ over the equatorial Pacific Ocean and global-scale climatic variations.

global-scale climatic variations.

## APPENDIX

Table A1. List of symbols and glossary of terms used in association with the ITCZ analysis procedure.

$\theta$	meridional coordinate
$\theta_c$	calculated meridional coordinate
$\phi$	longitudinal coordinate
$M_{\theta,\phi}$	calculated ITCZ value at $\theta,\phi$
$M_T$	temporary minimum value
band	- an interval in $\theta$ with all values having the same sign
boundary minimum	- a minimum value contained within an inner and outer boundary
continuous value	- with reference to any previously calculated value $M_{\theta_c,\phi}$ , the range absolute minimum value at $\theta,\phi+2$ such that $ \theta-\theta_c  \leq 2^\circ$
envelope	- for any value $M_{\theta,\phi}$ , the interval $[\theta-8^\circ, \theta+8^\circ]$ at $\phi+2$
inner boundaries	- northern: $\theta = 16^\circ\text{N}$ for $99^\circ\text{W} \leq \phi \leq 161^\circ\text{W}$ southern: $\theta = 0^\circ$ for $99^\circ\text{W} \leq \phi \leq 161^\circ\text{W}$
minimum	- any relative or absolute minimum value contained entirely within latitudinal interval under consideration
range	- $4^\circ\text{S}$ to Central American coast for $79^\circ\text{W} \leq \phi < 99^\circ\text{W}$ ; $0^\circ$ to $16^\circ\text{N}$ for $99^\circ\text{W} \leq \phi \leq 161^\circ\text{W}$
outer boundaries	- northern: $\theta = 20^\circ\text{N}$ from $161^\circ\text{W}$ to Mexican coast then along Pacific coast to $\phi = 79^\circ\text{W}$ southern: $\theta = 4^\circ\text{S}$ for $79^\circ\text{W} \leq \phi \leq 161^\circ\text{W}$  southern: $\theta = 4^\circ\text{S}$ for $79^\circ\text{W} \leq \phi \leq 161^\circ\text{W}$

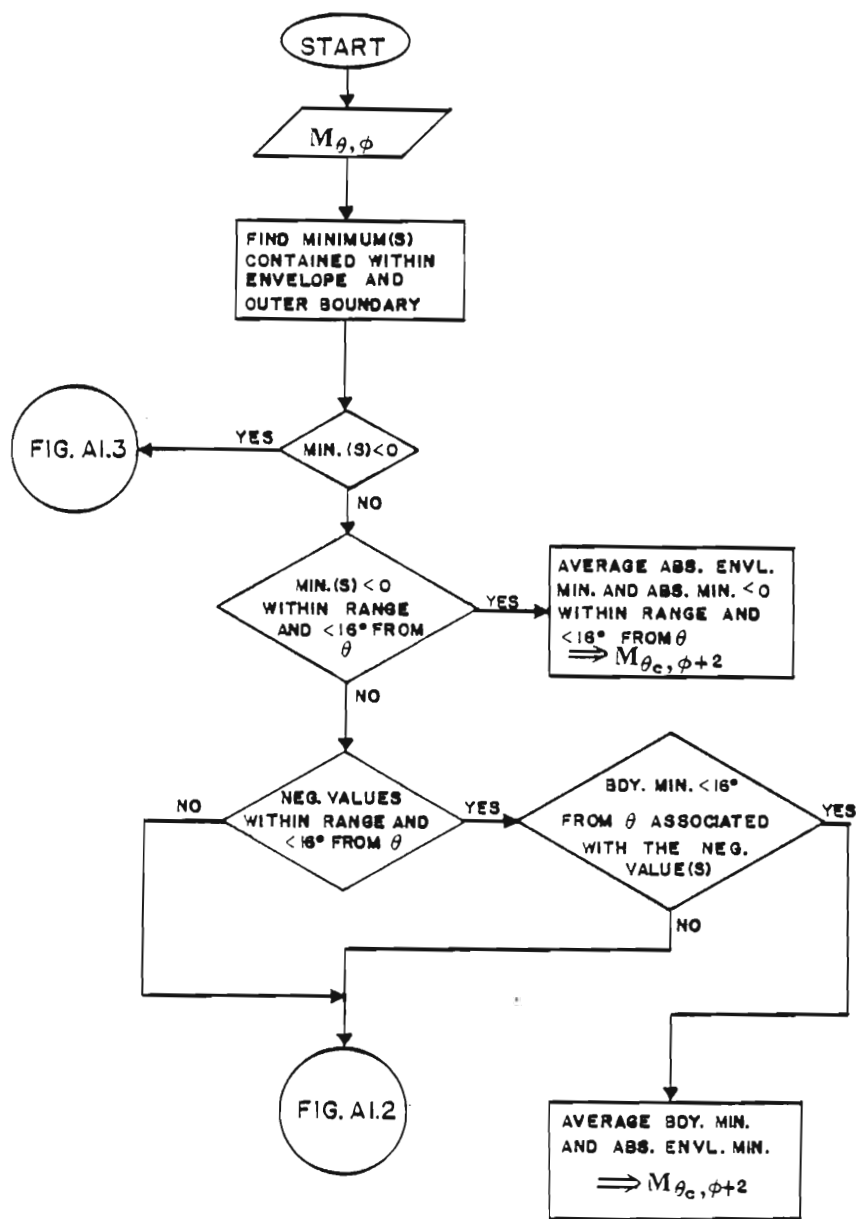


Fig. A1.1. Detailed flow chart of the procedure used for one  $2^\circ$  space step ITCZ calculation ( $M_{\theta, \phi} \rightarrow M_{\theta_c, \phi+2}$ ) from a filtered

divergence field. This scheme is followed for all computations except at the eastern boundary ( $\phi = 79^\circ\text{W}$ ) where  $M_{\theta, \phi}$  is defined to be the true minimum. All divergence field. This scheme is followed for all computations except at the eastern boundary ( $\phi = 79^\circ\text{W}$ ) where  $M_{\theta, \phi}$  is defined to be the true minimum. All intensity averages are arithmetic means; calculated ITCZ latitudinal positions are given to the closest even number grid point.

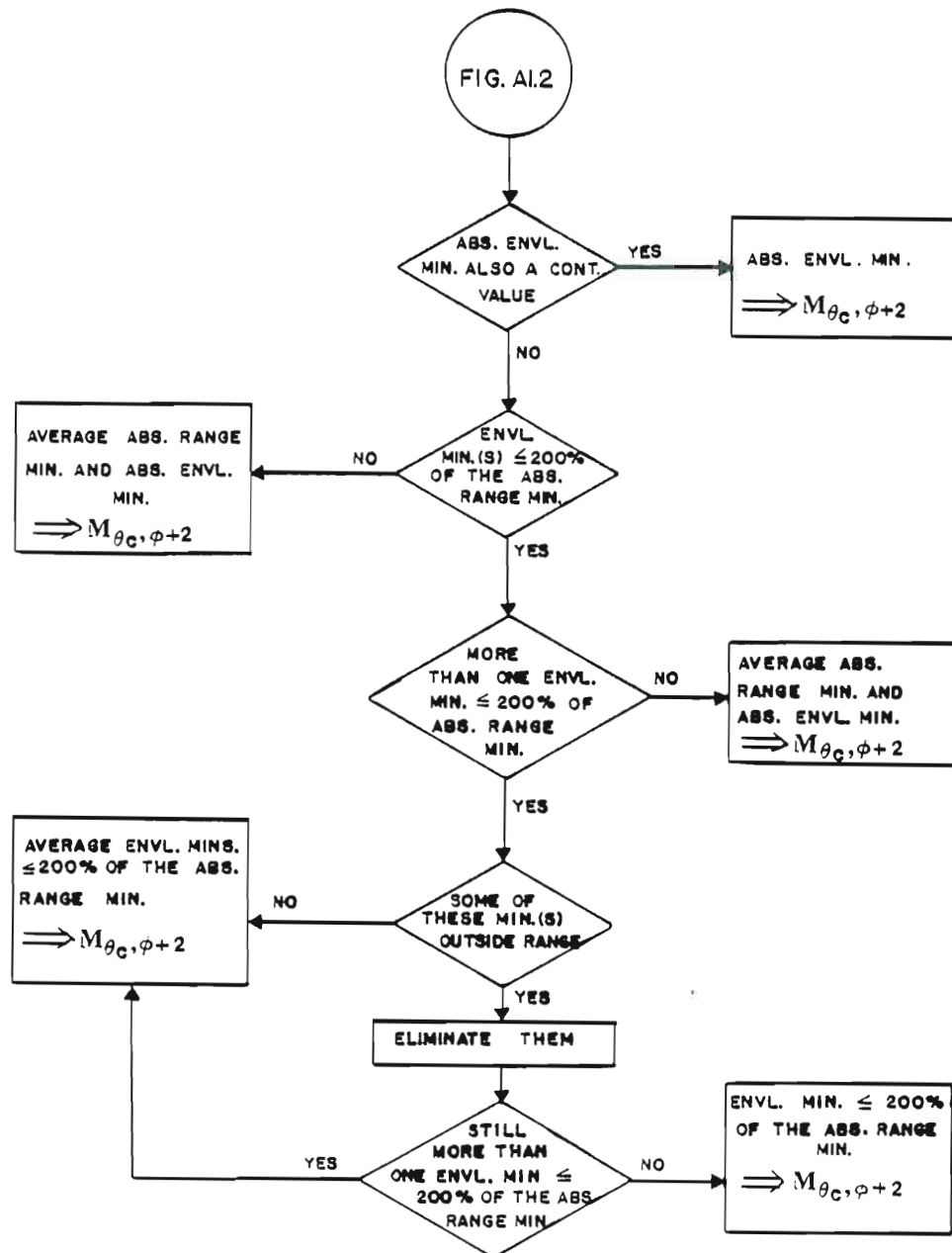


Fig. A1.2. Continuation from Fig. A1.1.

Fig. A1.2. Continuation from Fig. A1.1.



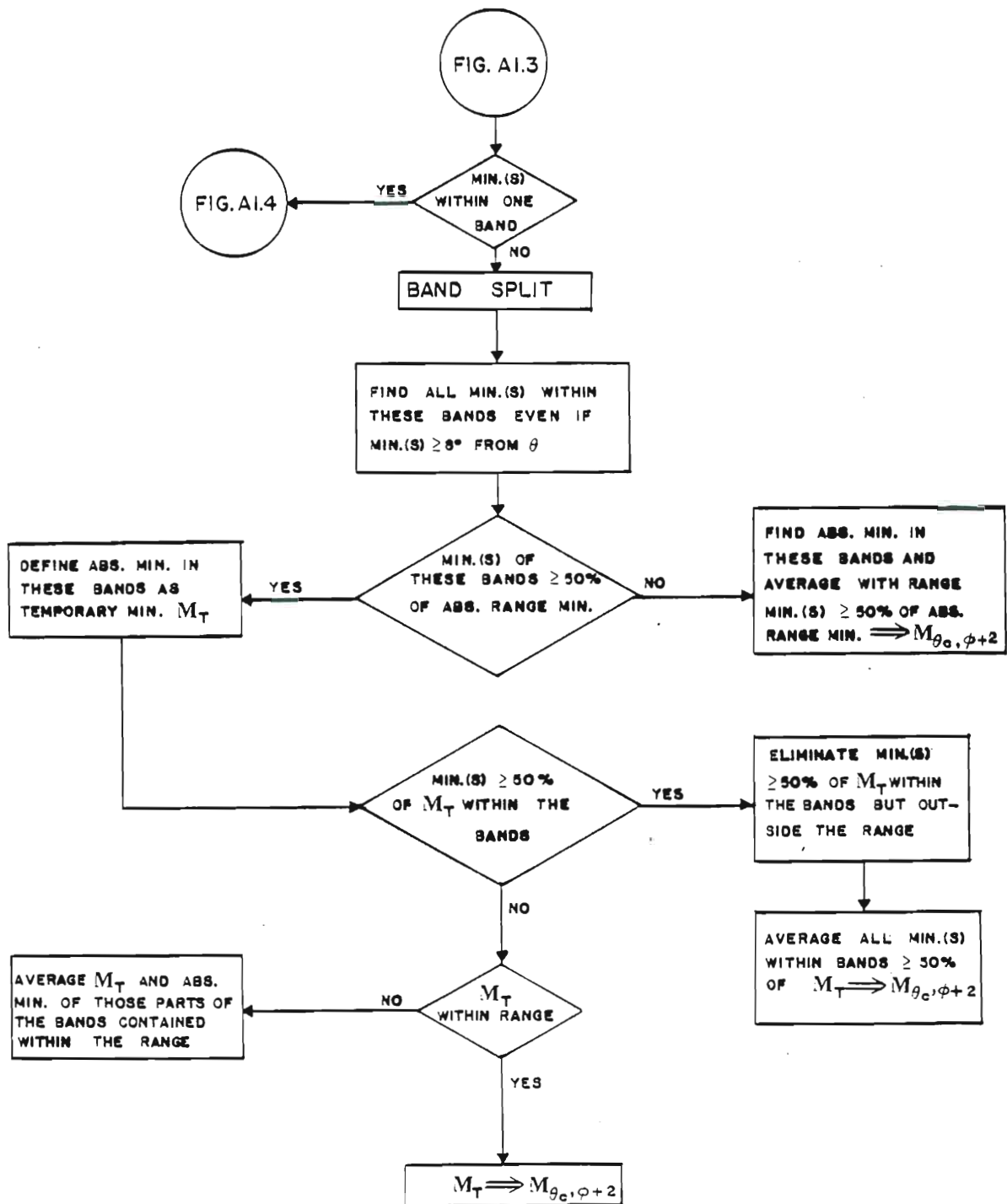


Fig. A1.3. Continuation from Fig. A1.1.

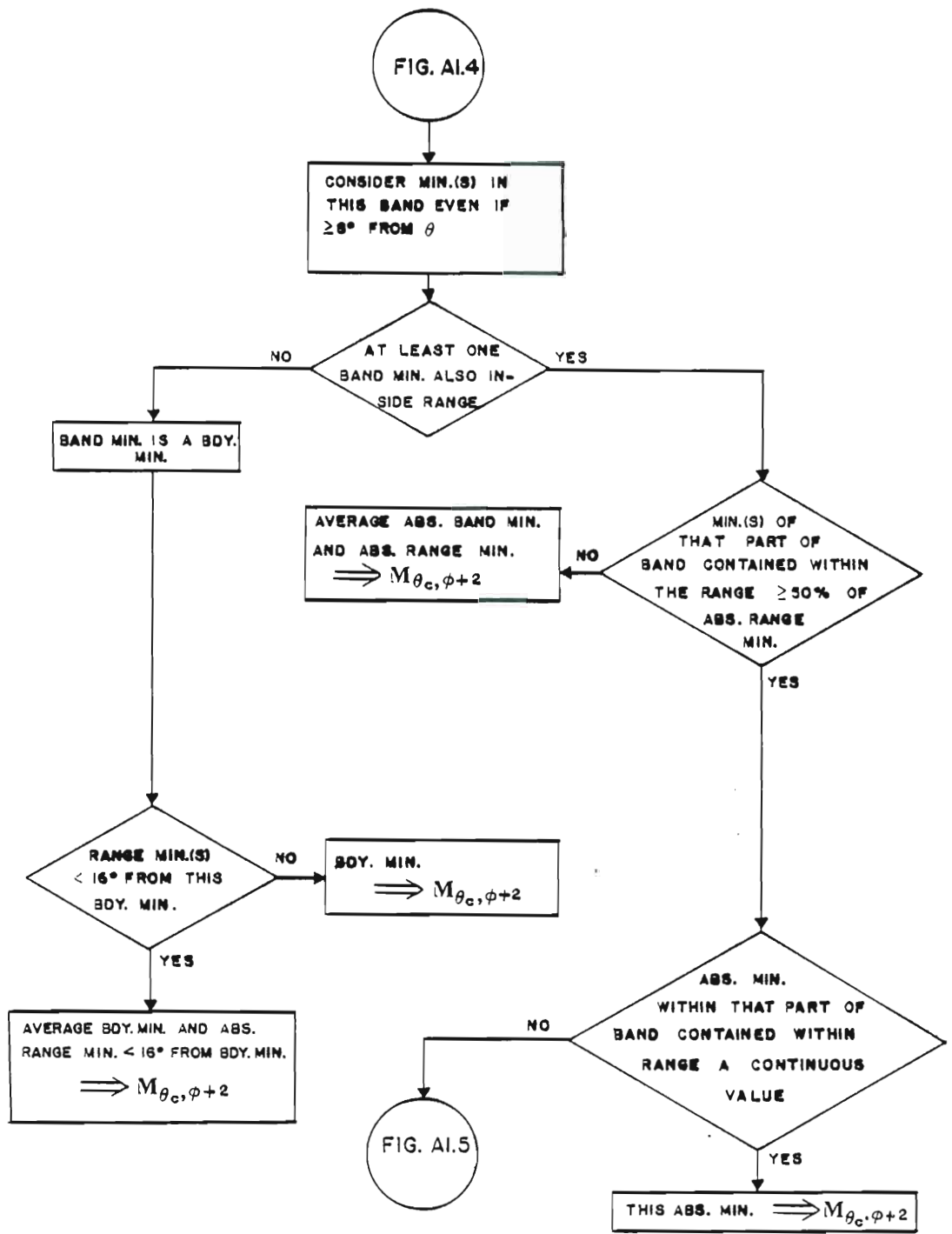


FIG. A1.4. CONTINUATION FROM FIG. A1.3.

Fig. A1.4. Continuation from Fig. A1.3.

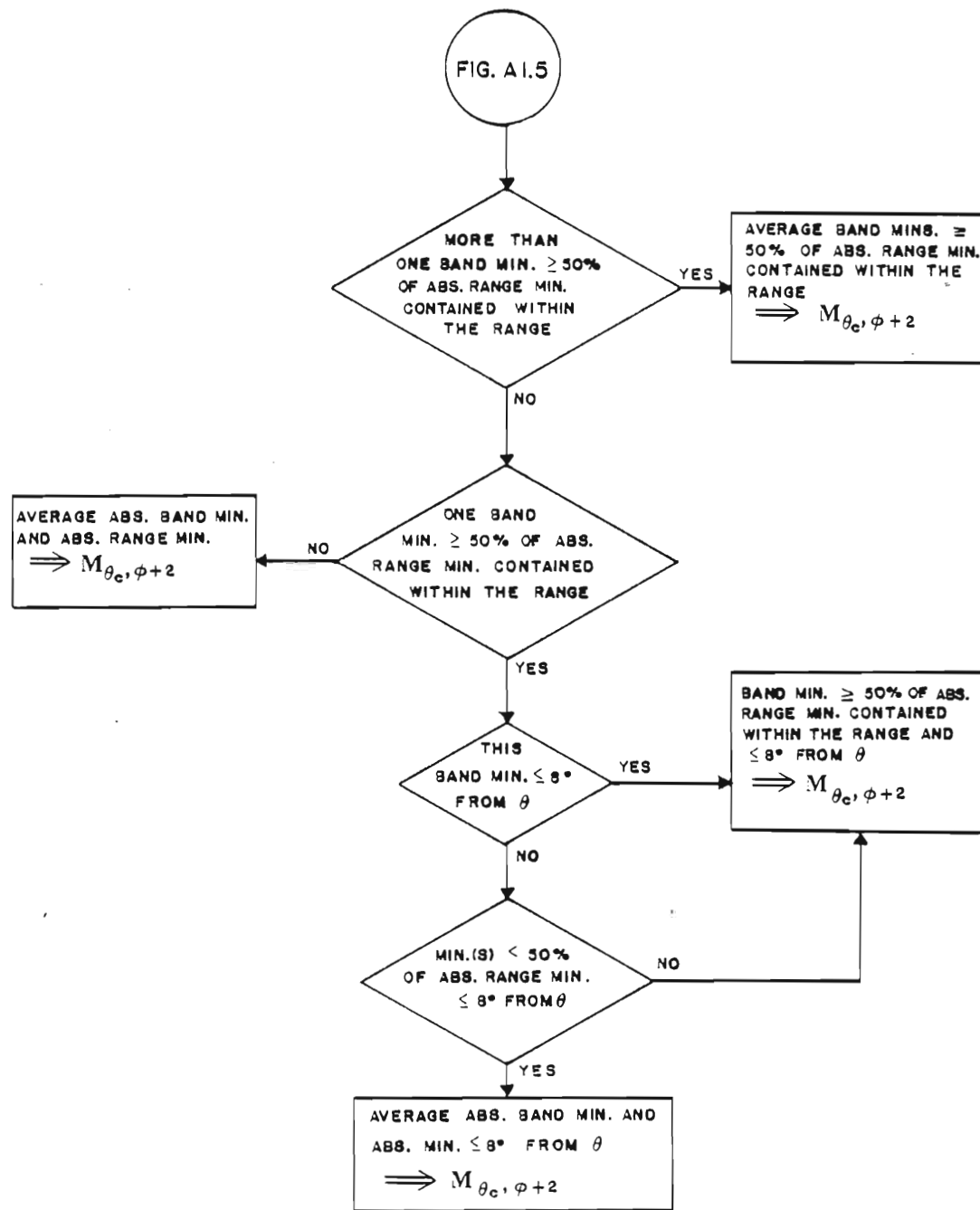


Fig. A1.5. Continuation from Fig. A1.4.

Fig. A1.5. Continuation from Fig. A1.4.

## REFERENCES

- Alpert, L., 1945: The Intertropical Convergence Zone of the Eastern Pacific Region (1). Bull. Amer. Met. Soc., 26, 426-432.
- Atkinson, G. D., 1971: Forecaster's Guide to Tropical Meteorology. Tech. Rept. No. 240, Air Weather Service (MAC), United States Air Force, 1-360.
- Chang, C.-P., 1970: Westward propagating cloud patterns in the tropical Pacific as seen from time-composite satellite photographs. J. Atmos. Sci., 27, 133-138.
- Donguy, J. F., and C. Henin, 1980: Surface conditions in the eastern equatorial Pacific related to the intertropical convergence zone of the winds. Deep Sea Res., 27A, 693-714.
- Dorman, C. E., and R. H. Bourke, 1979: Precipitation over the Pacific Ocean, 30°S to 60°N. Mon. Wea. Rev., 107, 896-910.
- Egger, J., G. Meyers and P. B. Wright, 1981: Pressure, wind and cloudiness in the tropical Pacific related to the Southern Oscillation. Mon. Wea. Rev., 109, 1139-1149.
- Fletcher, R. D., 1945: The General Circulation of the Tropical and Equatorial Atmosphere. J. of Meteor., 2, 167-174.
- Gray, W. M., 1968: Global view of the origin of tropical disturbances and storms. Mon. Wea. Rev., 96, 669-700.
- Hastenrath, S., and P. J. Lamb, 1977: Climatic Atlas of the Tropical Atlantic and Eastern Pacific Oceans. The University of Wisconsin Press, Madison, 15 pp.
- Hastenrath, S., and P. Lamb, 1978: On the dynamics and climatology of Press, Madison, 15 pp.
- Hastenrath, S., and P. Lamb, 1978: On the dynamics and climatology of surface flow over the Equatorial oceans. Tellus, 30, 436-448.

- Hubert, L. F., A. F. Krueger, and J. S. Winston, 1969: The double intertropical convergence zone - Fact or fiction? J. Atmos. Sci., 26, 771-773.
- Jenkins, G. M., and D. G. Watts, 1968: Spectral Analysis and Its Applications. Holden-Day, 543 pp. (see Chapter 2).
- Kornfield, J., A. F. Hasler, K. J. Hanson, and V. E. Suomi, 1967: Photographic cloud climatology from ESSA III and V computer produced mosaics. Bull. Amer. Soc., 48, 878-883.
- Liebmann, B., and D. L. Hartmann, 1982: Interannual variations of outgoing IR associated with tropical circulation changes during 1974-78. J. Atmos. Sci., 39, 1153-1162.
- O'Brien, J. J., and S. B. Goldenberg, 1982: Atlas of Tropical Pacific Wind Stress Climatology, 1961-1970. Florida State University, Tallahassee, 200 pp. (in press).
- Pazan, S. E., and G. Meyers, 1982: Interannual fluctuations of the tropical Pacific wind field and the Southern Oscillation. Mon. Wea. Rev., 110, 587-600.
- Ramage, C. S., 1975: Preliminary discussion of the meteorology of the 1972-73 El Niño. Bull. Amer. Meteor. Soc., 56, 234-242.
- Ramage, C. S., and A. M. Hori, 1981: Meteorological aspects of El Niño. Mon. Wea. Rev., 109, 1827-1835.
- Ramage, C. S., S. J. S. Khalsa, and B. N. Meisner, 1981: The Central Pacific near-equatorial convergence zone. J. Geophys. Research, 86, 6580-6598.
- Rasmusson, E. M., and T. H. Carpenter, 1982: Variations in tropical 86, 6580-6598.
- Rasmusson, E. M., and T. H. Carpenter, 1982: Variations in tropical sea surface temperature and surface wind fields associated with the Southern Oscillation/El Niño. Mon. Wea. Rev., 110, 354-384.

- Reiter, E. R., 1978: Long-term wind variability in the tropical Pacific, its possible causes and effects. Mon. Wea. Rev., 106, 324-330.
- Sadler, J. C., L. Oda and B. J. Kilonsky, 1976: Pacific Ocean cloudiness from satellite observations. UHMET 76-01, Department of Meteorology, University of Hawaii, Honolulu, 137 pp.
- Simpson, R. H., 1947: Synoptic aspect of the intertropical convergence near Central and South America. Bull. Amer. Met. Soc., 28, 335-346.
- Weare, B. C., P. T. Strub and M. D. Samuel, 1980: Marine Climate Atlas of the Tropical Pacific Ocean. Contr. Atm. Sci. No. 20. University of California, Davis, 147 pp.
- Wyrtki, K., and G. Meyers, 1975: The trade wind field over the Pacific Ocean. Part I. The mean field and the mean annual variation. Rep. HIG-75-1. Hawaii Institute of Geophysics, University of Hawaii, Honolulu, 26 pp.